Summer 2019

Exploring transition metal chalcogenides for bio sensing and environmental remediation

Bahareh Golrokh Amin

Department: Chemistry

EXPLORING TRANSITION METAL CHALCOGENIDES FOR BIO SENSING AND ENVIRONMENTAL REMEDIATION

by

BAHAREH GOLROKH AMIN

A DISSERTATION

Presented to the Faculty of the Graduate School of the

MISSOURI UNIVERSITY OF SCIENCE AND TECHNOLOGY

In Partial Fulfillment of the Requirements for the Degree

DOCTOR OF PHILOSOPHY

in

CHEMISTRY

2019

Approved by:

Manashi Nath, Advisor
Amitava Choudhury
Jeffrey Winiarz
Philip D. Whitefield
Mohsen Asl Zaeem

PUBLICATION DISSERTATION OPTION

This dissertation consists of the following four articles, formatted in the style used by the Missouri University of Science and Technology:

Paper I: Pages 44-65 have been published in *Chemical Communications*.

Paper II: Pages 66-103 have been published in *Journal of Materials Chemistry B.*

Paper III: Pages 104-143 are reviewed and need minor revisions for publication in *ACS Omega*.

Paper IV: Pages 144-169 are intended for submission to *Journal of Power Sources.*

ABSTRACT

Electrocatalysts play an inevitable role in many applications including energy storage, energy conversion, and biosensing. The state-of-the-art noble metal-based electrocatalysts have long been used in full water splitting, non-enzymatic glucose sensing, and supercapacitors. However, scarcity and high cost of noble metals restrict utilization of such electrocatalysts in large-scale implementations. Transition metal-based electrodes have been considered as a potential solution to address these drawbacks as well as to enhance the electrocatalytic performance. In this work, applicability of non-oxidic transition metal based electrocatalysts is evaluated. Transition metal chalcogenides are expected to have high catalytic performance owing to their facilitated electron cloud delocalization on the transition metal site as well as enhanced covalency in the lattice due to the low anion electronegativity. To examine this theory, $CoNi_2Se_4$ is studied for its application in full water splitting. This catalyst shows an excellent electrocatalytic activity with low overpotential of 160 mV @ 10 mA cm^{-2} for OER. $CoNi_2Se_4$–rGO on Ni foam has also been employed as an electrocatalyst for the direct oxidation of glucose. A high sensitivity of 18.89 mA mM^{-1} cm^{-2} at low applied potential of 0.35 V vs. Ag|AgCl is achieved. For the same application, we investigated Ni_3Te_2. With electrodeposition method, a high glucose detection sensitivity of 41.615 mA cm^{-2} mM^{-1} is reported. We also fabricated a hydrothermally synthesized Ni_3Te_2 with a sensitivity of 35.213 mA cm^{-2} mM^{-1}. Finally, we examined $NiCo_2Se_4$/rGO for its application in supercapacitors and achieved a high specific capacitance of 2038.55 F g^{-1} with a high energy density and power density of 67.01 W h kg^{-1} and 903.61 W kg^{-1}, respectively.

ACKNOWLEDGMENTS

First and foremost, I am thankful to my advisor, Dr. Manashi Nath for offering me her mentorship and support throughout the past years. This work would not have been possible without her encouragement. It was under her guidance that I overcame many difficulties and learnt a lot. I want to express my gratitude to Dr. Chaudhury, Dr. Winiarz, Dr. Whitefield and Dr. Asl Zaeem for serving on my dissertation advisory committee and for reviewing this dissertation and giving such thoughtful feedback.

I am fortunate to work in NRG research lab and collaborating with my amazing lab mates, Umanga, Wipula, Xi, Rajarshi, Apurv, and Jahangir.

I must also thank my dear friends, with whom I shared so many unforgettable memories. Amin Jamjah, who was always beside me to push me and motivate me, Sajjad Amini, Alireza Toghraee, Mahdi Valipour, and Amir Armani.

I am ineffably indebted to my parents, Azadeh and Hadi, for having faith in me, for their selfless love, constant support and encouragement and sacrifice that they made to shape my life to become a successful individual. I also thank my lovely brother and aunt, Arian and Zohreh, whose belief in me, gave me confidence to continue.

Last but certainly not least, I owe thanks to a very special person in my life, my husband, Koosha Marashi for his endless support and understanding during my pursuit of Ph.D. degree. He was always around at times I thought that it is impossible to continue and helped me to keep things in perspective. I greatly value his contribution and deeply appreciate his belief in me.

TABLE OF CONTENTS

Page

LIST OF ILLUSTRATIONS

SECTION Page

LIST OF TABLES

1. INTRODUCTION

Catalysts are substances that increase the rate of chemical reactions without being consumed. Catalyzed reactions take alternative reaction pathways that need lower activation energy, and therefore, take place at a higher rate than non-catalyzed mechanisms at the same temperature and for the same reactant concentrations (Figure 1.1). Catalysts that participate in electrochemical reactions, are called electrocatalysts. The electrocatalysis reaction takes place on the surfaces of catalysts, where adsorption and desorption steps happen.

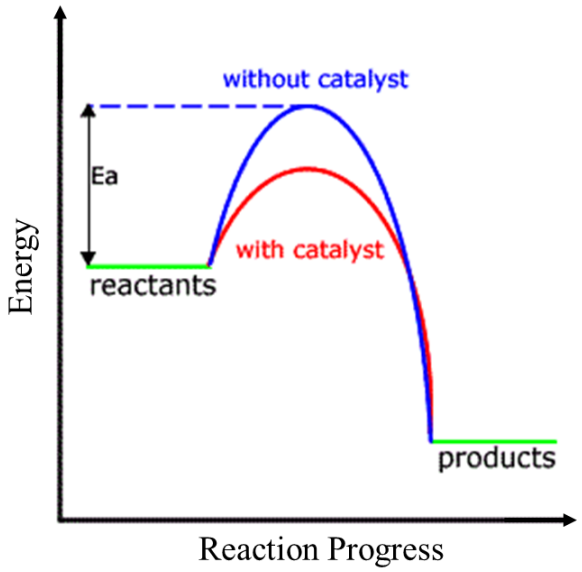

Figure 1.1. Potential energy diagram showing the effect of a catalyst in a hypothetical chemical reaction.

Electrocatalysts are utilized in numerous applications and directly affect our daily lives. Without using proper electrocatalysts, many of the technologies are rendered

useless due to drastic decrease of the reaction rates in electrochemical processes. Examples include CO_2 reduction, which is a method for alleviating global warming, electricity generation technologies such as fuel cells and solar cells, full water splitting, and advanced biosensing technologies. Figure 1.2 depicts some of the applications in which electrocatalysts play a prominent role.

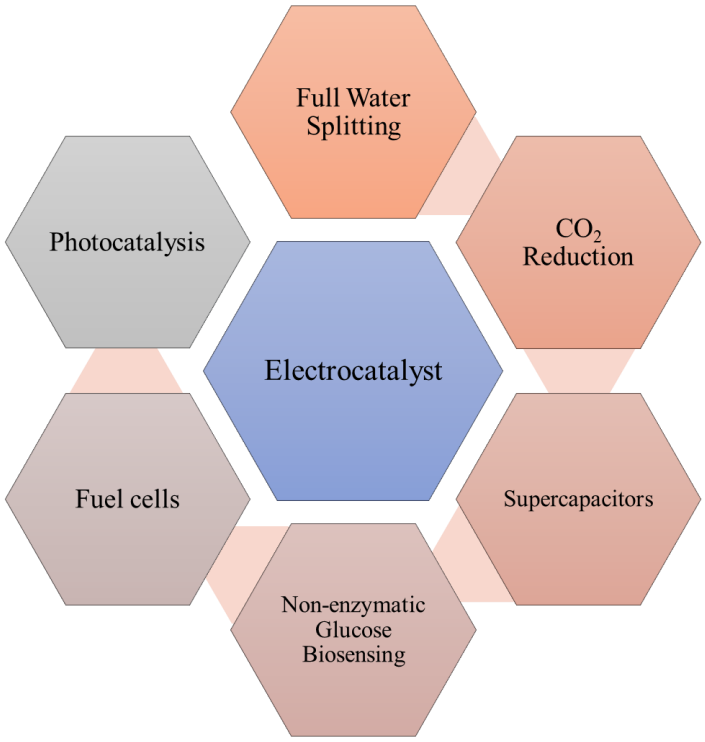

Figure 1.2. Domains and technologies where electrocatalysis is used.

Noble metals have long been recognized and utilized as electrocatalysts in variety of applications from environmental remediation to biosensing. However, their scarcity and high cost limit their implementation in large scales. Recent years have witnessed the advent of first row transition metal compounds as suitable candidates to substitute noble

metal electrocatalysts in energy storage, conversion, and biomedical sensing applications owing to their earth-abundancy, low cost, and high electrocatalytic performance.

Until recently, most of the reported transition metal-based compounds were limited to transition metal oxides/hydroxides. However, it is shown that in certain cases, modifying the environment around the central metal atom can result in optimized and enhanced properties. In the series of chalcogenides, electronegativity of the chalcogen atoms gradually decreases from 3.5 for oxide to 2.4 for selenide. With this decrease in the electronegativity, the degree of covalency in metal-chalcogen bond increases. Hence, it is expected to have a higher valence band energy level for the selenides and tellurides, which reduces the band gap between valence band and conduction band and enhances the electrocatalytic activity of resulting transition metal compounds.[1-3]

Apart from changing the anion coordination down the chalcogenide series, transition metal doping can also enhance the electrocatalytic activity of the compound. Mixed transition metal selenides such as spinel structure $CoNi_2Se_4$ introduce more catalytically active sites for the interaction between the catalyst and reaction media. This increases active surface area and further improves the electrocatalytic performance.[1]

The research presented in this dissertation is devoted to exploring new transition metal chalcogenide as electrocatalysts in different applications. We investigated the practicality of substituting oxygen with chalcogenides that have a higher degree of covalency in the metal-chalcogen bond as the anion atom. We fabricated transition metal chalcogenide electrodes using selenide and telluride and evaluated their performance. Results show that the new materials have high electrocatalytic activity and superior stability in alkaline. The rest of this section introduces areas of full water splitting, non-

enzymatic glucose sensing, and supercapacitors. In the next four sections, our papers are provided, where we have discussed methodologies, comparison with other studies, and results for each project. Finally, concluding points are presented in the last section.

1.1. BIFUNCTIONAL CATALYSTS FOR OVERALL ELECTROCHEMICAL WATER SPLITTING

The necessity of minimizing the dependency on fossil fuels has triggered the research community to search for earth-abundant, everlasting, CO_2 emission-free, and eco-friendly alternative energy sources.[4-8] Alternative energy strategies that utilize hydrogen as the primary carrier hold great promise for a clean and inexhaustible energy future. Success of such technologies relies mainly on efficient production of hydrogen. Water electrolysis, also known as water splitting, is one of the most promising approaches to produce pure molecular hydrogen.[9-12] Water splitting is composed of oxygen evolution reaction (OER), where molecular oxygen is generated, as well as hydrogen evolution reaction (HER), where hydrogen molecules are produced.

Water electrolysis is an uphill reaction rather than a spontaneous process and its rate is governed by the magnitude of the applied potential. A proper electrocatalyst can lower the required applied potential, in addition to expedite the overall process.

The most effective catalysts known to date for HER and OER were noble-metal-based materials and have fair bifunctional activity. Pt-based compounds for HER[13-15] and Ir- and Ru-based compounds for OER[16-18] are decent examples. However, scarcity and high price are the major drawbacks in practical application of noble-metal-based catalysts.[19,20] Considerable research efforts have been devoted to finding alternative materials to achieve a non-precious and highly active bifunctional HER-OER

electrocatalyst to simplify the overall design, lower the cost, and speed up the overall water splitting process.[21-23] As a result, several bifunctional catalysts composed of earth-abundant elements were explored and evaluated, such as metal alloys [24, 25], metal oxides/hydroxides [26, 27], chalcogenides [1-3, 28-30], carbides [31,32], phosphides [33, 34], and metal-free nanomaterials [35]. Another group of bifunctional catalysts are transition metal chalcogenides, which have decent attributes including rich redox chemistry, promising activity, high stability under a variety of conditions, and low cost. [1-3, 28, 30]

The two half-cell reactions of OER and HER in an alkaline medium is illustrated in Figure 1.3. Note that while the external voltage is applied, the water splitting process is continued between the anode (OER domain) and the cathode (HER domain).

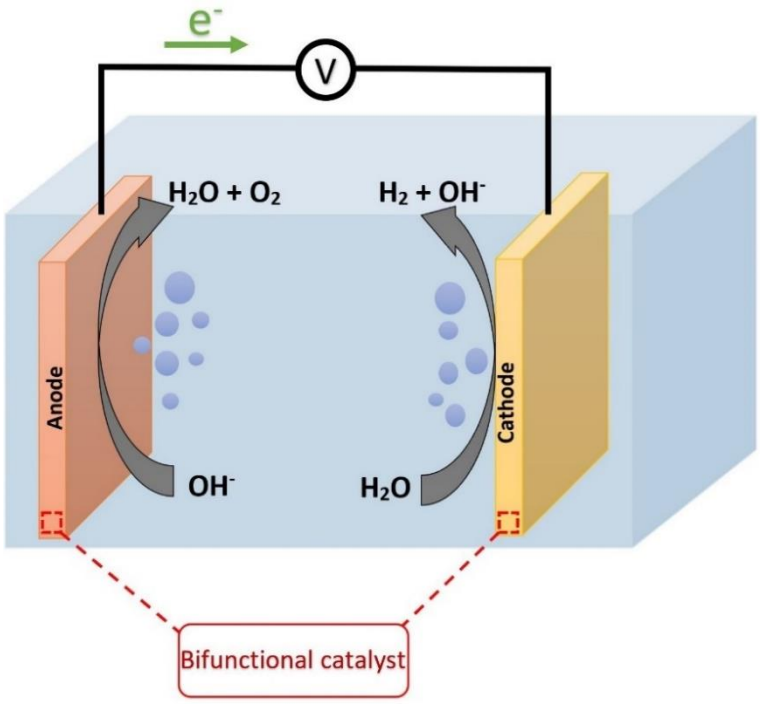

Figure 1.3. Schematic illustration of alkaline water splitting, electrochemical hydrogen, and oxygen evolution reactions happening on a bifunctional catalyst.

The thermodynamic voltage of water splitting is known to be 1.23 V (at 25 ºC and 1 atm), regardless of the reaction medium.[36] However, the electrolysis of water including breakage of O-H bond and forming O_2 and H_2 is kinetically sluggish and generally requires a cell potential substantially higher than the thermodynamic value of 1.23 V vs. reversible hydrogen electrode (RHE). The water splitting reaction undergoes multiple steps, where in each step a single electron transfer takes place. For each of these steps a kinetic barrier needs to be overcome, which consequently entails a higher applied potential on the cell.[37-39] The overpotential voltage for water splitting can be described as follows:[40, 41]

$$V_{op} = 1.23\ V + \eta_a + |\eta_c| + \eta_\Omega \quad (1)$$

where η_Ω represents the excess potential applied for compensating the system internal resistance. η_a and η_c are the overpotentials required to overcome the intrinsic activation barriers of the anode (OER domain) and cathode (HER domain). An electrocatalyst with elevated activity is highly desirable to overcome the intrinsic energy barrier of the anode and cathode.

1.1.1. Oxygen Evolution Reaction. Oxygen evolution reaction, the anodic reaction of water electrolysis, is the process of generating molecular oxygen (O_2) by a chemical reaction from water. In the sluggish four-electron process of OER, molecular oxygen is produced via several proton-electron coupled procedures.[23, 42, 43] Depending on the pH of the electrolytes in which water electrolysis is happening, the half reaction of water splitting for OER can be described as one of the following forms:[4, 44]

$$4\ OH^- \leftrightarrow 2\ H_2O_{(l)} + O_{2(g)} + 4\ e^- \qquad \text{Alkaline solution}$$

$$2\ H_2O_{(l)} \leftrightarrow 4H^+ + O_{2(g)} + 4\ e^- \qquad \text{Acidic solution}$$

1.1.2. Hydrogen Evolution Reaction. HER is a two-electron process that constitutes the other half of the water splitting. Even though the reaction involves only two electrons for each hydrogen molecule, the multiple elemental reactions induce an accumulation of energy barriers and result in slow kinetics.[44, 45] Depending on the different reaction conditions, either acidic or alkaline electrolyte, HER can be described as one of the two forms shown below:[44]

$$2\ H_2O_{(aq)} + 2\ e^- \leftrightarrow H_{2(g)} + 2\ OH^-_{(aq)} \qquad \text{Alkaline solution}$$

$$2\ H^+_{(aq)} + 2\ e^- \leftrightarrow H_{2(g)} \qquad \text{Acidic solution}$$

Ideally, a bifunctional catalyst should have low overpotentials for both OER and HER reactions. For such catalyst to be useful in practice, it further needs to be highly stable with low fabrication cost to be scalable at industrial scale.

1.1.3. Electrolyte. Different pH levels of the electrolytes can strongly influence the performance of electrode material. Until now, an alkaline solution for the OER is the optimal pH to achieve highest performance as most of the reported OER and HER catalysts are not stable in pH < 7. On the other hand, the activity of the electrode for both OER and HER will decrease at pH levels close to a neutral solution and reaches its lowest performance while in acidic electrolyte.[4]

1.1.4. Electrode Materials. Commonly used catalysts for both HER and OER are composed of precious metals and their oxides such as Pt, IrO_x, and RuO_x.[13-18, 46, 47] Due to the scarcity and high cost of these noble metals, there has been significant efforts to identify a nonprecious electrocatalyst based on transition metal compounds including alloys (mostly containing Ni, Co, or Fe)[48], oxide/ hydroxide [49, 50], and chalcogenides.[1-3, 30]

Among these electrocatalysts, the selenide-based ones have a superior performance, in particular in terms of lowered overpotential and increased current density.[1-3, 30, 51-55]

Owing to the probability of charge delocalization between metals via overlapping of d-d orbitals in the crystalline structure, the Lewis acidity of the catalysts will increase. Hence, the rate of hydroxyl adsorption on the catalysts surface enhances.[1, 56]

Among several types of transition metal chalcogenides, Ni-based catalysts are proven as highly efficient materials for both OER and HER. However, doping Ni metal with other transition metals such as Co, can provide numerous active sites accessible for water oxidation process by increasing the surface area exposed to the solution.

Ni-Co-based selenides, which are mixed metal selenide-based catalysts, meet the requirements for catalyzing OER and HER, owing to their desirable electrocatalytic activity in alkaline electrolytes arising from the tunability of the Ni^{2+}/Ni^{3+} and Co^{2+}/Co^{3+} redox couples.[57-62]

1.1.5. Efficiency of Full Water Splitting. It goes without saying that the catalyst material is the primary factor in both OER and HER performances. However, there are several other features that can significantly affect these reactions. Below, we briefly discuss these factors and their effects on the reaction performance.

1.1.5.1. Overpotential and onset potential. Overpotential is the deviation of the electrode potential from the standard reduction potential to cause a given current density. For measuring the overpotential in the water splitting reaction, it is common to choose the difference between the potential (at which a current density of 10 mA cm^{-2}) is achieved from the standard potential of 1.23 V. Generally, a catalyst that has overpotential in the range of 200–300 mV is considered as a competent catalyst for OER.

Thus far, there are only few reported catalysts that have overpotential values less than 200 mV.[4, 13]

Another more demonstrative method of evaluating the performance of a catalyst is using onset potential. The onset potential is the potential at which the process starts as determined by an increase in current in a current-potential curve. In fact, onset potential captures the additional driving force required to overcome the kinetic barriers in a reaction. Since finding the onset potential sometimes relies on extrapolation of the rising portion of the current-potential curve, which is exponential in this region, the evaluation is not always rigorous.

1.1.5.2. Tafel slope. Tafel equation relates the rate of an electrochemical reaction to the overpotential through the Tafel slope. The Tafel analysis is a common method that allows easy comparison of catalytic activities of different catalysts and is used to understand the reaction kinetic and mechanism. The Tafel slope helps to identify the rate determining step of the reaction, by examining the dependency of the current response at a given voltage using the following equation:

$$\eta = b \times \log (j / j_0) \quad (2)$$

where η indicates the overpotential, b indicates the Tafel slope, j represents the current density, and j_0 denotes the exchange current density. A compelling OER catalyst is determined by a small Tafel slope and large current density.[4, 13]

1.1.5.3. Mass and specific activities. The mass (catalyst loading) is a quantitative parameter to define the catalytic activity of an electrocatalyst. The smaller the catalyst loading to achieve certain current density, the more superior the catalytic activity.

Moreover, the current normalized by the electrochemical surface area (ECSA) known as the specific activity can be determined by measuring double layer charging current at different scan rates and is calculated using the following equation:

$$ECSA = C_{DL} / C_s \quad (3)$$

where *Cs* is the specific capacitance, C_{DL} was calculated based on the slop of the capacitive current (i_{DL}) from a non-faradaic double-layer region versus scan rate v ($V\ s^{-1}$).

1.1.5.4. Stability. The stability of an electrocatalyst for both OER and HER can be evaluated using two methods: first, subjecting the catalyst to multiple cyclic voltammetry (CV) cycling at high scan rates, and second, through chronoamperometric analyses.

The stability of a catalyst can be affected by many factors such as nature of an electrolyte and more importantly, the nature of the working electrode itself. Generally, the active materials directly grown on the working electrode are exhibiting higher stability compared to the pasted or drop-casted ones, as no binder is needed to stick the materials on the electrode surface.

In the study performed by Tahir et al., a qualitative assessment of stability is provided. Figure 1.4 shows this assessment and categorizes the stability levels into ideal, excellent, good, and satisfactory. An ideal material falls in the range of overpotentials less than 300 mV to reach 10 mA cm^{-2} current density and is able to remain in this range after 10 hours of stability check.[4]

In the work presented as Paper I of this dissertation, the stability of $CoNi_2Se_4$ was evaluated for both OER and HER using chronoamperometry measurements at a constant

current density. According to results shown in the respective section, $CoNi_2Se_4$ electrocatalyst is categorized in the "ideal" category in terms of its stability.

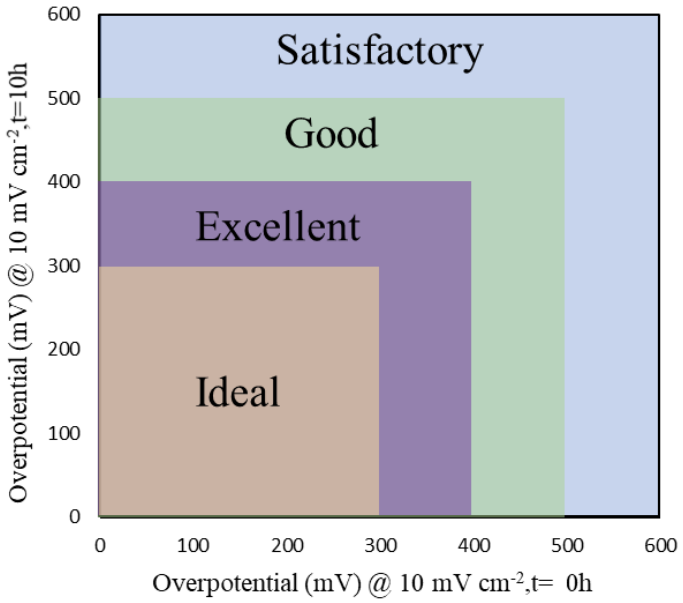

Figure 1.4. Acceptable overpotential range and stability after 10 hours, indicating the applicability of an electrode in practical applications. (adapted from reference 4).

1.2. NON-ENZYMATIC GLUCOSE SENSOR

Diabetes mellitus, commonly known as diabetes, is an increasingly prevalent condition resulting in abnormal blood glucose level that affects millions of people worldwide. Diabetes is a chronic disease, for which there is no known cure. As of 2013, almost 400 million people have been diagnosed with diabetes and this number is increasing at an alarming rate.[63, 64] Diabetes is a metabolism disorder in which the quantity of glucose in the blood is highly elevated due to the inability of the body to produce sufficient insulin. Insulin is a hormone that helps the glucose in blood to be absorbed by the body cells.[65-68]

The most common types of diabetes are type 1 and type 2. In type 1 diabetes, the immune system mistakenly attacks and destroys the insulin-producing cells, hence disabling pancreas to create insulin. About 10% of diabetic patients are classified in type 1 category. Type 2 diabetes arises when body is impotent to produce enough insulin or use insulin properly. This type is more common and accounts for about 90% of all cases worldwide.[69] Figure 1.5 shows the differences between the functioning of pancreas in a healthy person and individuals with the two types of diabetes. Both type 1 and type 2 diabetes can be treated by use of medications and/or externally supplying the necessary insulin to the body. If not treated, the glucose level in the blood can reach a critical level that may cause multi-organ damage for a diabetic person.

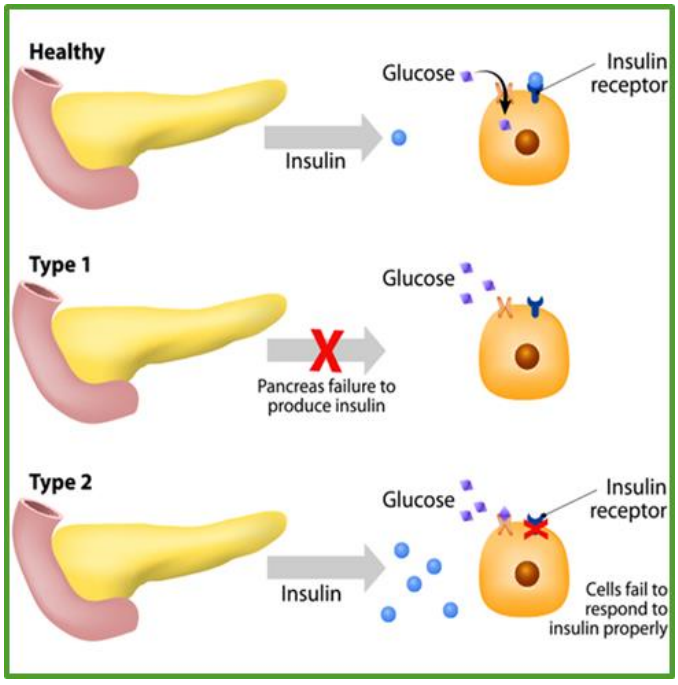

Figure 1.5. Type1 and Type 2 diabetes, pancreas malfunction. (adopted from Koutoubi, MD, Ph.D. research).

By monitoring the blood glucose level, patients are more likely to prevent diabetic emergencies such as hyperglycemia (excessively high concentration of glucose) or hypoglycemia (excessively low concentration of glucose). These conditions can lead to long-term complications such as heart attack, stroke, high blood pressure, kidney failure, and blindness.[70-73]

In conventional method for monitoring the blood glucose level, a drop of the blood is taken via finger pricking. This process, particularly when repeated frequently, brings anxiety, tension, and additional pain to the patients. For a diabetic person, it is common to test the blood glucose level several times a day. Also, relying on blood sampling often results in sporadic results of glucose changes throughout the day, rendering this approach impractical for monitoring glucose level during workout or overnight.[74, 75] Therefore, many studies are dedicated to finding alternative metering systems, capable of continuously and more conveniently measuring glucose level with high sensitivity and selectivity at a low cost.

Among various classes of known glucose biosensors, electrochemical glucose sensor technologies obtained significant recognition over the past few years. As compared to other technologies, the electrochemical glucose sensors can be easily fabricated at relatively low cost and have high sensitivity in the range of μM to mM as well as good repeatability and selectivity.[76, 77] Based on the sensing element utilized to detect glucose, electrochemical glucose sensors can be categorized into enzymatic and non-enzymatic types. The very first enzyme-based electrode was introduced by Clark and Lyons in 1962,[78] in which the catalytic oxidation of glucose was recorded based on the oxygen depletion in the environment. Since then, researchers have been actively making

ceaseless improvements in electrochemical glucose oxidation sensors, which resulted in three generations of enzymatic glucose sensors as summarized in Figure 1.6.

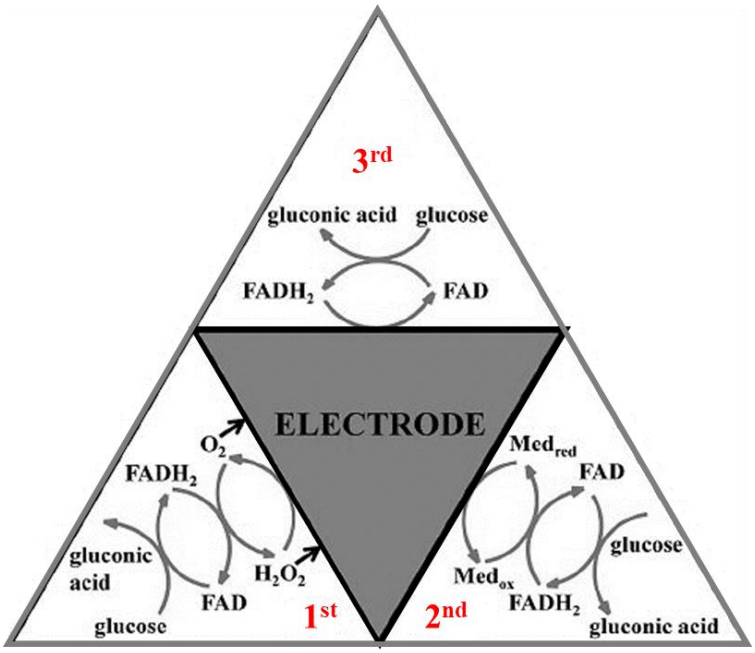

Figure 1.6. Summary of enzymatic glucose oxidation mechanisms presented as three generations.

1.2.1. First Generation Enzymatic Glucose Sensors. First generation glucose sensors, as shown in Figure 1.7, are dependent on the immobilization of an enzyme on the electrode and presence of oxygen as a co-substrate.[79, 80] In this method, glucose is oxidized to produce gluconolactone and hydrogen peroxide using glucose oxidase (GOx) attached on the electrode surface as the catalyst of the reaction. The concentration of glucose can be evaluated by measuring the amount of hydrogen peroxide generated at the electrode. In this method, the reliance of the reaction on existence of free oxygen for mediating the regeneration of the catalytic center and producing hydrogen peroxide can

significantly reduce the accuracy of glucose level determination. Another shortcoming of this type of glucose sensing is the high applied potential required for generation of H_2O_2 from O_2. This large potential can also oxidize unwanted interfering species co-exist in the blood, such as ascorbic acid, uric acid, dopamine, and countless other drugs, which in turn, creates a huge background effect.[81, 82]

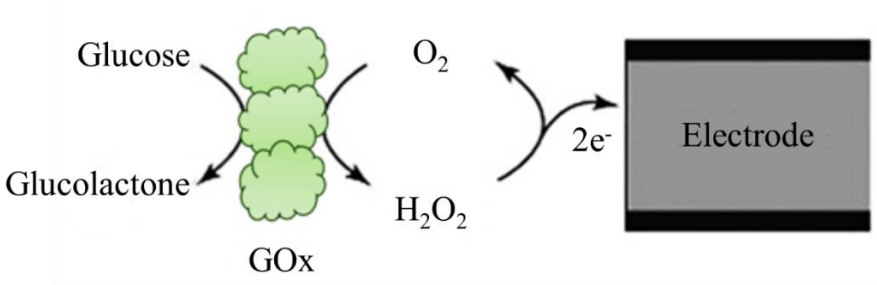

Figure 1.7. Glucose oxidation in first generation of enzymatic glucose sensors.

A number of solutions were suggested to overcome the problems associated with the first generation of glucose sensing; however, all of the approaches either overcomplicate the fabrication process or enlarge the overall size of the sensor. These major issues motivated researchers to search for a new method, referred to as the second generation glucose sensing.

1.2.2. Second Generation Enzymatic Glucose Sensors. In the second generation of glucose sensors, artificial electron-accepting mediators were used to serve as a substitution to oxygen –the first-generation mediator, and to facilitate the electron transfer process.[83,84] The second generation of enzymatic glucose sensors are fabricated using GOx as an immobilized enzymatic catalyst on an artificial mediator as shown in

Figure 1.8. Ferricyanide and derivatives of ferrocene have been widely used as mediator due to their low molecular weight, low toxicity, and high stability.[85-87]

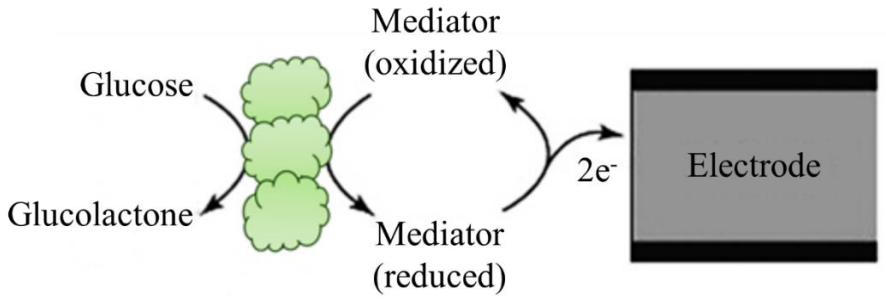

Figure 1.8. Glucose oxidation mechanism in second enzymatic glucose sensors.

Although this generation of enzymatic glucose sensors were able to address some of the issues of the first generation, maintaining the mediator close to the electrode surface is difficult. Also in this approach, the performance of the electrode is dependent on external factors such as changes in the pH, temperature, humidity, and other interferences.[88, 89] Although the mediator reacts at a considerably faster rate than oxygen, there is still a chance for oxygen to compete with the mediator, which reduces the accuracy of the system. Moreover, the reaction between mediators and the co-existing interfering species is not eliminated, lowering the efficiency of the sensor.

1.2.3. Third Generation Enzymatic Glucose Sensors. In the third generation of glucose sensor technology, the electron transfer process occurs directly between the enzyme and the electrode, eliminating the reaction mediator, as presented in Figure 1.9.[90, 91] This was done by securing the thick proteins of enzyme to the electrode.

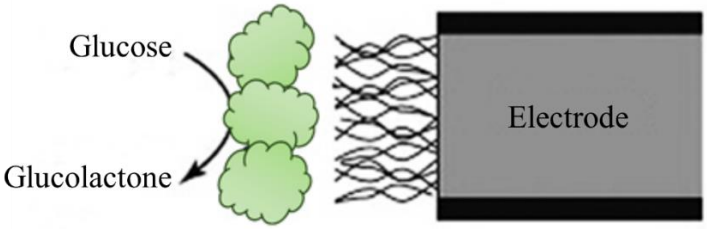

Figure 1.9. Glucose oxidation in the third generation of enzymatic glucose sensors.

Since both glucose and mediators must access the redox active centers, improvements in active surface area of the electrode can increase the electron transport rate.[92] Recent progress in developing nano and porous materials allows making electrodes with increased surface area which can entrap the enzyme and enhance the performance.

Figure 1.10 depicts the formation of the layers in a test strip of the third-generation enzymatic glucose sensors. As shown in the figure, the components include counter/reference electrodes, spacer, working electrode, a bottom supporting layer, as well as the enzyme and the mediator coated onto the working electrode.

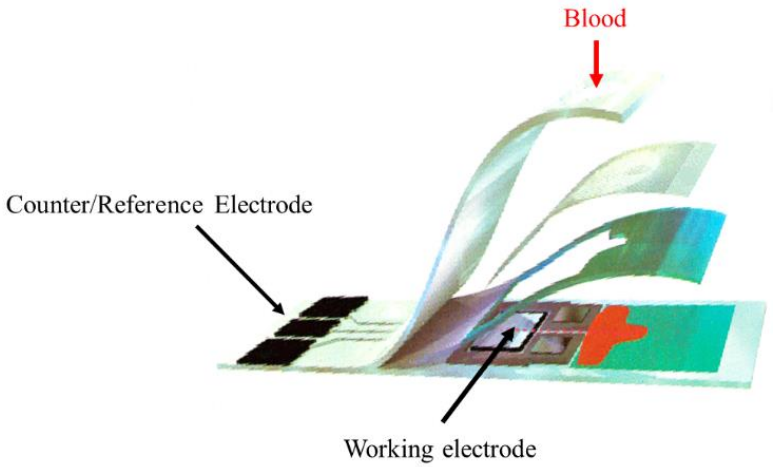

Figure 1.10. Cross section of a commercial strip for self-testing of blood glucose level.

Despite the performance improvements compared to their two former counterparts, the third-generation enzymatic glucose sensors still suffer from the limitations related to the use of enzymes. The activity of enzymes is always dependent on the changes in humidity, temperature, and pH. In addition, slow electron transfer process in the thick enzyme layers can limit the efficacy of the biosensor. These drawbacks were the motivation for researchers to explore for an enzyme-free glucose sensor, which led to the development of the fourth generation of glucose sensors.

1.2.4. Fourth Generation Non-Enzymatic Glucose Sensors. In the recent years, due to the intrinsic limitations of all enzyme-based sensors, such as insufficient stability and poor repeatability, studies have been redirected towards the possibility of creating enzyme-free electrochemical sensors. In enzyme-free biosensors, also known as non-enzymatic glucose (NEG) sensors, the process of glucose oxidation occurs directly on the electrode surface as shown in Figure 1.11.[93-97] The oxidation of glucose is facilitated by an electrocatalyst that transfers the charge from the electrode to electrolyte.[98] Therefore, the electrode design as well as formulation of electrocatalyst composition plays a substantial role in the success of this technology.

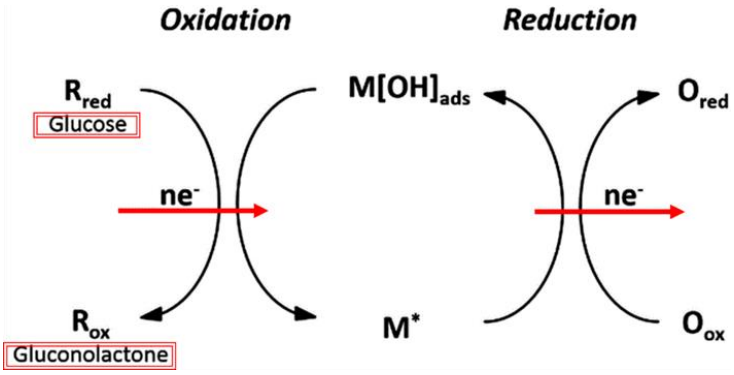

Figure 1.11. Glucose oxidation on the electrode surface in NEG sensors.

Direct electrooxidation of glucose on the surface of the electrode in NEG sensors is highly dependent on the electrode materials. Therefore, nanostructured materials with the capability of increasing active surface area and enhancing mass transport were established as a valuable tool in glucose sensing performance.[99-101]

Among different materials used as catalysts for NEG sensing, noble metals, such as Pt are shown to have a good performance.[102-105] The challenge of using noble metals in NEG sensors despite their acceptable performance is their scarcity and high cost, which limit their large-scale applications.[106] In addition, noble metals suffer from surface poisoning by the intermediates present inside solution, which can immediately cover the electroactive surface and reduce selectivity and sensitivity of the glucose sensor.[107-110]

Besides the noble metals, transition metals, such as Ni, Co, and Cu, can also be used as catalysts in NEG sensors. These non-precious metals can develop outstanding reaction kinetics owing to their multivalence nature (e.g., redox couple of Ni^{2+}/Ni^{3+} in alkaline media), which results in ultrahigh sensitivity (up to mA mM^{-1} Cm^{-2}).[111]

In Table 1.1, a comprehensive comparison between enzymatic and non-enzymatic electrochemical glucose biosensors is presented. In this table, advantages and disadvantages of each category as well as the differences between noble metal-based and transition metal-based NEG sensors are explained.

Characteristics of transition metal-based electrodes make them suitable for accurately measuring glucose level from low concentration alternate body fluids, such as saliva, urine, sweat, etc. This can enable developing glucose sensors that can determine the concentration of glucose in the body without the need for taking blood samples. If diabetic patients are provided with such non-invasive and convenient glucose measuring

methods, they are more likely to collect frequent glucose levels, which allows them to optimize their insulin injections.[112, 113]

Table 1.1. Comparison of enzymatic and non-enzymatic glucose sensors.

Sensor type	**Sensing element**	**Example**	**Reaction**	**Advantages**	**Disadvantages**
Enzyme-based	Biological enzymes	GOD	GOD_{ox} + glucose → GOD_{red} +glucolactone	- Good selectivity - Acceptable sensitivity	- Sensitive to changes - Insufficient stability
Non-enzymatic	Noble metal	Pt	Glucose + Pt → Glucolactone + Pt	- Blood sample tests - Relatively stable	- High cost - Prone to poisoning
	Transition metals	Ni	Ni(III) + glucose → Ni(II) + gluconolactone	- Ultrahigh sensitivity - Stable - Low cost	- Active only in alkaline media - Fair selectivity

Concentrations of glucose in the alternative body fluids are as low as 0 to 0.8 mmol L^{-1} for urine[114], 0.03 to 0.08 mmol L^{-1} for saliva[115], and 0.02 to 0.6 mmol L^{-1} for sweat[116], requiring the glucose sensor to be highly sensitive and selective and have an extremely low limit of detection (LOD).

The catalytic ability of transition metal oxides for the non-enzymatic direct electrooxidation of glucose has been explored for more than a decade.[117] These electrodes require minimal fabrication cost and have shown to be stable glucose sensors. The electrocatalytic activity of transition metal-based sensors involve electrochemical redox reaction at the transition metal site, which facilitates charge transfer to the electrolyte and

initiates glucose oxidation. On the other hand, the anion used in the catalyst composition has a significant influence on the potential in which the glucose oxidation happens.[118]

In the trend of catalytic activity between oxygen and the rest of chalcogenides, as the electronegativity of the chalcogen atom decrease from oxygen to telluride, degree of covalency in metal-chalcogen bond increases. This results in a higher valence band energy level for the selenides and tellurides which will reduce the band gap between valence band and the conduction band. By rising the valance band edge closer to the glucose oxidation level, the applied potential can be lowered. This is significantly important because the lower the applied potential, the lower the interference of other species during glucose monitoring, resulting in better selectivity of the electrode.

The central hypothesis of our projects is enhancing the catalytic activity of the non-enzymatic glucose sensors by modifying the anion coordination from oxide to selenide and telluride. The adjustment in anion coordination can lower the potential needed to oxidize glucose and consequently, increases the selectivity and sensitivity of the electrocatalyst.

We rely on the theory that transition metal doping increases the active surface area, and hence can further enhance the catalytic activity of the catalyst towards glucose oxidation. Testing these hypotheses resulted in confirmatory reports presented as Paper II and Paper III in this dissertation.

Adjacency of operating potentials in oxygen evolution process and glucose oxidation reaction, as depicted in Figure 1.12, motivated investigating applicability of the same catalyst used for OER, namely $CoNi_2Se_4$, as the electrocatalyst for glucose sensing.

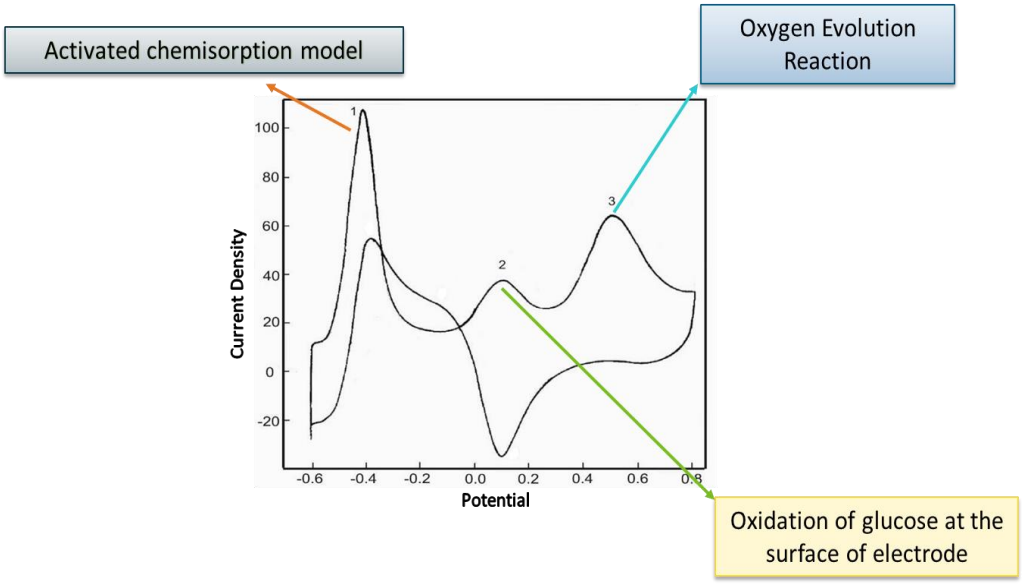

Figure 1.12. Similarity in OER and glucose oxidation processes.

1.2.5. Other Applications of Non-Enzymatic Glucose Electrodes. Although glucose electrooxidation is mainly useful in glucose level determination, some of its other usages are equally or even more prominent. Glucose electrooxidation is used in several industrial process such as in food industry and development of fuel cells and batteries. Non-enzymatic sensors, despite their application in biosensing, are vastly used in non-physiological situations. Owing to their high electrocatalytic activity, non-enzymatic electrodes can outperform their enzymatic counterparts in many of the applications, such as fuel cells. Besides their performance, specific non-enzymatic electrodes are shown to have better chemical resistance, long-term sensitivity, and thermal stability, making them very suitable for practical applications with extreme environments.[119] In the remainder of this section, some of the non-physiological applications of non-enzymatic glucose electrodes are explained.

1.2.5.1. Industrial processes. Non-enzymatic glucose electrodes have a great potential for being used in several bio-industrial processes. Examples are fermentation plants and large-scale synthesis in the pharmaceutical industry. In the fermentation plants, the main challenge is enforcement of strict environmental controls for optimal production. Therefore, adaptable sensors with stable performance are desired. Non-enzymatic electrodes, unlike their enzymatic counterparts do not require optimum controlled conditions and can maintain their performance in spite of environment changes. In the pharmaceutical industry, several of the processes are contingent upon an effective control of the formation and consumption of key analytes or reactants, e.g., glucose. While there are many instances of using enzymatic glucose sensors, non-enzymatic ones are to be further developed and practically utilized.[120-123]

1.2.5.2. Quality control. In the food industry, quality control is an inevitable component of the production cycle. This process is responsible for validating the quality, maturity, nutritional value, and authenticity of the product. Non-enzymatic electrodes are widely used in the quality control for measuring the quantity of various types of sugar. The relatively low LOD, and hence high sensitivity, ensures their ability in detection of small amounts of substances.[124-126] Non-enzymatic glucose electrodes, in particular, have been extensively used to discriminatively determine aldose sugars (e.g., glucose, xylose, and galactose) and ketose sugars (e.g., fructose and sorbose).[127]

1.2.5.3. Bio-fuel conversion. In the past decade, developing carbon neutral renewable energy sources has been one of the main areas of research in several disciplines. Fuel cells constitute one of the technologies that are under investigation. The fact that glucose is a by-product of photosynthesis and is readily harvested in natural

sugars, makes it an ideal source to replace fossil fuels. Moreover, successful development of a glucose-fed fuel cell can also enable fabrication of biologically powered artificial organs, such as heart or pacemaker.[128-130]

A glucose-based fuel cell allows generation of power from a degradable biomass that is nontoxic, nonflammable and readily and renewably available. In other words, we can obtain a high energy output from a sustainable source. Such developments can potentially lead to replacement of batteries used in portable devices and electric vehicles with glucose-based fuel cell systems. Theoretically, the complete oxidation of glucose in a fuel cell can occur at a potential of 1.23 V and yield the processes shown below, releasing 2870 kJ mol^{-1} of energy. [131]

$$C_6H_{12}O_6 + 24OH^- \rightarrow 6CO_2 + 18H_2O + 24e^- \quad \text{Anode}$$

$$6O_2 + 12H_2O + 24e^- \rightarrow 24OH^- \quad \text{Cathode}$$

$$C_6H_{12}O_6 + 6O_2 \rightarrow 6CO_2 + 18H_2O \quad \text{Overall}$$

Despite the fact that the complete glucose oxidation process yields a substantial amount of energy, in practice, all enzymatic and most of the non-enzymatic electrodes can only oxidize the glucose to glucolactone, a mere two-electron process that releases 250 kJ mol^{-1}.[131] While this is always the case for enzymatic electrodes, a non-enzymatic electrode has the potential to fully oxidize the glucose and release more energy. This can be done by applying a higher potential to the system, but it defeats the purpose of a fuel cell. In transition metal chalcogenide-based glucose sensors however, the operating potential is significantly lower, allowing complete or more substantial oxidation of the glucose.

1.3. SUPERCAPACITORS

There is a growing concern about our dependency on depleting fossil fuel for our energy demands. The emission of green-house gases such as CO_2 or methane from the fossil fuels have exacerbated the global warming crisis. These along with several other consequences underscore the urgency of exploring a renewable, efficient, and clean energy source as well as a new technology to store the generated energy for later utilization.

One of the most well-known technologies for electrochemical energy storage developed for practical applications in our daily lives are batteries. However, despite the high energy density of the batteries, they are suffering from relatively low power delivery and limited cycle life*. This elevates the need for an energy storage device with high power density, longer life span, and shorter charge/discharge time.[132, 133]

In the recent years, supercapacitors have attracted considerable attention to bridge the gap between traditional dielectric capacitors with high power output and batteries with high energy density.[134, 135] Although the first supercapacitor introduced in 1957, not until late 90s did supercapacitors begin to draw some attention, which was due to the growing demand for electric vehicles and portable electronics.[136] Supercapacitors are able to boost the batteries in electric vehicles by providing the required power for acceleration. Moreover, supercapacitors can complement the energy storage function of the batteries by delivering back-up power supplies to protect batteries from power disruptions.[137]

---

* Typically defined as the number of complete charge/discharge cycles that a battery is able to support before its capacity falls under 80% of the original value.

In spite of the high power density of electrochemical supercapacitor, their restrictions such as low energy density and high production costs motivated researchers to investigate various approaches to overcome these limitations. Since the electrochemical performance of supercapacitors is largely dependent on the properties of electrode materials, intensive studies have been carried out to develop new electrode materials with high capacitive characteristics.

1.3.1. Types of Supercapacitors Based on the materials utilized to fabricate the electrodes and charge storage mechanism, supercapacitors are classified in three different categories shown in Figure 1.13. More details regarding each of these types of supercapacitors are provided in the following sections.

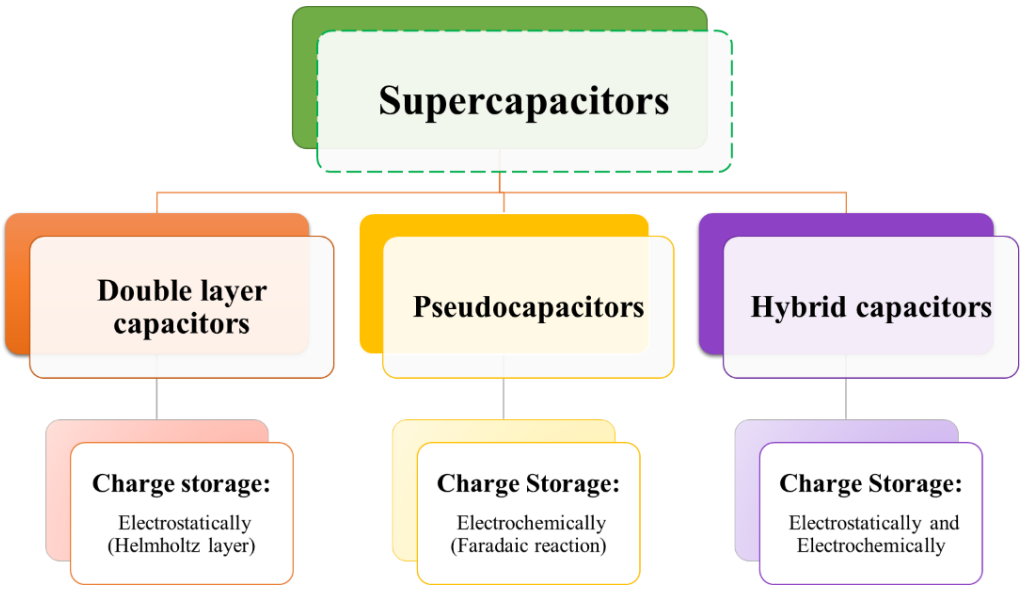

Figure 1.13. Different types of supercapacitors.

1.3.1.1. Electric double layer capacitors. The energy storage mechanism in Electric double layer capacitors (EDLCs) can be described as the accumulation of

electrostatic charge on the electrode/electrolyte interface. The double layer includes two layers of charges. The first layer is composed of an agglomeration of electric charge on the surface of the electrode. The second layer is the electrolyte ions with counterbalancing charge buildup on the electrolyte side that provides the electroneutrality. The diagram in Figure 1.14 shows the process of storing charge in EDLC.

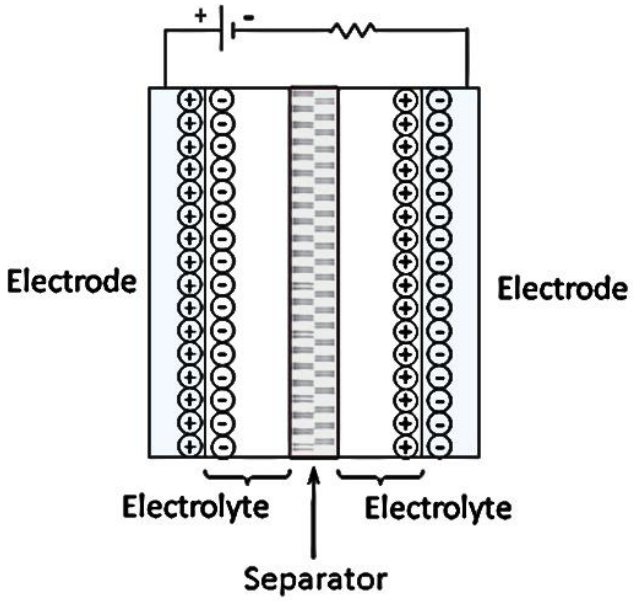

Figure 1.14. Charge storage mechanism in EDLCs.

In EDLCs, the ions from the electrolyte adhere to the surface of the electrode via electrostatic force without forming any chemical bond. During the process of charging, by applying a voltage between two electrodes, cations migrate to the negative electrode (cathode) while anions travel towards the positive electrode (anode), forming two charged layers inside the electrolyte. In the discharge cycle the reverse process takes

place, resulting in ions moving in the opposite direction. Therefore, during the process of charge – discharge in EDLCs, the concentration of electrolyte remains constant.[138, 140]

The electrochemical process of charging and discharging an electrode can be summarized as follows:

Charging: $E_{surface} + A^- \rightarrow E^+_{surface} \,||\, A^- + e^-$

Discharging: $E^+_{surface} \,||\, A^- \rightarrow E_{surface} + A^-$

where A^- is the anion, $E_{surface}$ is the electrode surface, and || represent the electrode/electrolyte interface.[141, 142]

1.3.1.2. Pseudocapacitors. Pseudocapacitors store electrical energy faradaically by electron charge transfer between electrode and electrolyte. This is accomplished through electrosorption, redox reactions, and intercalation processes, collectively referred to as pseudocapacitance. When a potential is applied to a pseudocapacitor, also known as faradaic supercapacitor (FS), a rapid redox reaction of the electrode materials takes place on or near the surface of the electrode. The reversible faradaic reaction of the electrode materials results in a charge passing across the double layer, which induces faradaic current flow through the supercapacitor cell (Figure 1.15).[140, 143]

Pseudocapacitors operate in an extended voltage window and have higher specific capacitance compared to EDLCs. The larger specific capacitance and consequently the better energy density of pseudocapacitors is due to occurrence of the electrochemical process on the surface of the electrode as well as in the bulk near the surface.[143]

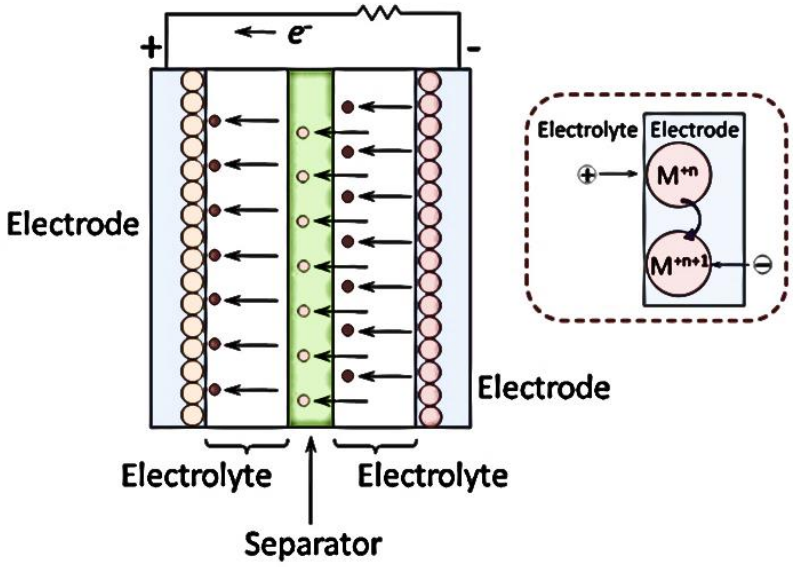

Figure 1.15. Charge storage mechanism in pseudocapacitors.

Although the specific capacitance achieved by pseudocapacitors can be 10 to 100 times larger than the electrostatic capacitance of EDLCs, FSs typically have lower power density and poor cycling stability compared to EDLCs. The low power density of FSs can be attributed to their slow faradaic reaction compared to fast non-faradaic reaction of EDLCs. On the other hand, their unsatisfactory stability is related to the redox reaction, and hence decomposition of the electrode materials, taking place directly on the electrode surface.[144, 145]

To capitalize the advantages and compensate the disadvantages of EDLCs and pseudocapacitors and to improve the specific capacitance, energy density, power density, and the overall cell voltage, hybrid supercapacitors were introduced.[146-148] In the next section, we elaborate on hybrid supercapacitors.

1.3.1.3. Hybrid supercapacitors. Hybrid supercapacitors, as the name suggests, incorporates mechanisms from both faradaic and double layer capacitance.[149, 150] The process of charge storage in hybrid supercapacitors is depicted in Figure 1.16.

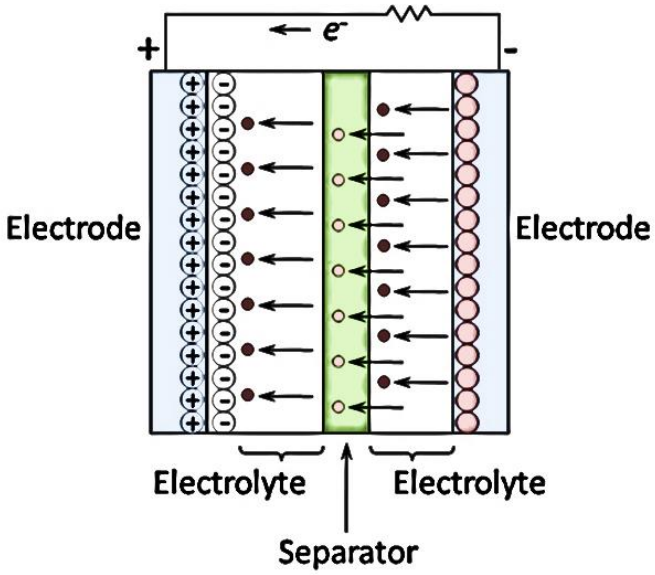

Figure 1.16. Charge storage mechanism in hybrid supercapacitors.

In both faradaic and double layer capacitance charging processes, which happen simultaneously in a hybrid supercapacitor, an electrode material with large surface area, high conductivity, and high porosity can significantly improve the performance. Therefore, in the research community, an extensive effort is devoted to developing new materials and improving the performance of the existing electrodes with high capacitance, energy density, and power density.

1.3.2. Electrode Materials. Based on the application, supercapacitors can be fabricated with different materials. Figure 1.17 shows the electrode materials used for the three types of supercapacitors discussed earlier.

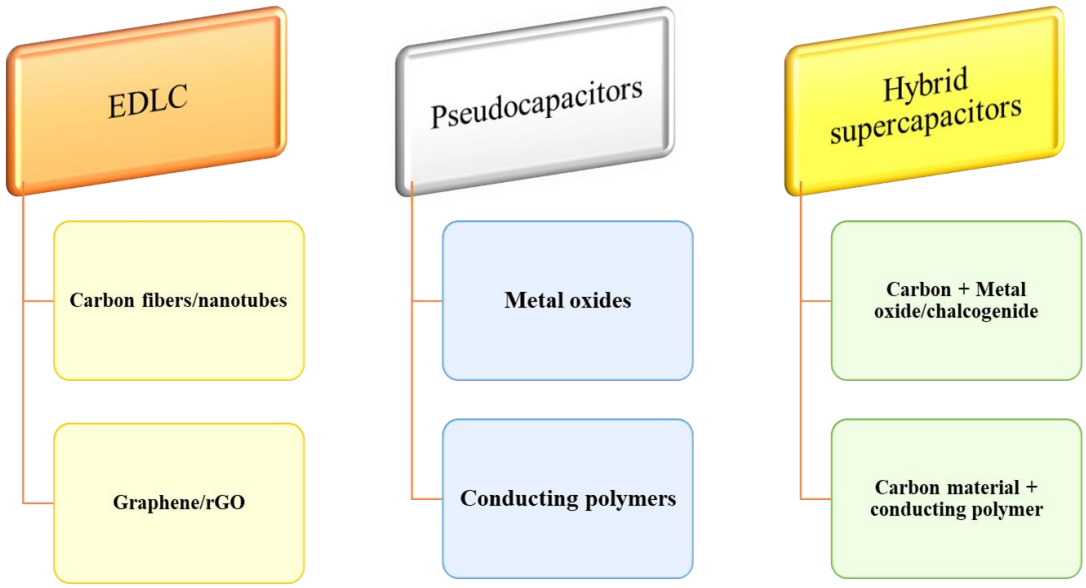

Figure 1.17. Classifications of different electrode types and their materials.

1.3.2.1. Carbon-based electrode. The high electric field originated by the electric double layers in EDLCs enhance their energy storage performance compared to conventional capacitors.[151] As mentioned earlier, the charge storage and capacitance of the supercapacitors are highly related to the electrode materials. Among various materials investigated as an ideal candidate in energy storage systems, the most significant substance used for commercial purposes is carbon-based materials with high surface area and highly porous structure.

The charge storage process in carbon-based electrodes predominately occurs on the electrochemical double layer formed at the electrode/electrolyte interface, hence, the performance of the supercapacitor is mainly dependent on the surface area accessible to the electrolyte ions. For this reason, specific surface area, morphology of the materials, porosity, and electrical conductivity collectively plays an important role in the electrochemical performance of the electrode.[153-154]

Several carbon-based materials such as activated carbons, graphite, graphene, and reduced graphene oxide have been extensively studied as possible electrode materials in EDLC energy storage devices. All of these materials have excellent properties including abundance, non-toxicity, high surface area, high chemical stability, high electrical conductivity, and wide operating temperature range.[155-157]

In particular, graphene, a two-dimensional single layer of carbon atom with sp2-hybridization, has been investigated as a promising candidate for EDLCs due to its remarkable electrical, mechanical, and thermal properties.[158] However in practice, high internal resistance between the carbon particles and inaccessible surface area for the electrolyte ions results in limited performance.[143, 159]

The future of carbon-based electrodes is contingent on eliminating these limitations by developments in carbon materials with surface modifications to improve the overall conductivity and capacitance without compromising the stability.

1.3.2.2. Metal oxide. Metal oxides are able to produce more energy density Compared to carbon-based electrodes, while they can provide better electrochemical stability in contrast with conductive polymers.[160] Many metal oxides have been extensively investigated for their applications in pseudocapacitors and hybrid

supercapacitors such as RuO_2 [161, 162], MnO_2 [163, 164], and V_2O_5 [165, 166]. Among these, RuO_2 is the first pseudocapacitor electrode material introduced in 1971 with a faradaic charge-transfer reaction.[167] Although RuO_2 can offer a reversible redox reaction in a wide potential window with acceptable specific capacitance and high energy density, it is not an ideal electrode material due to its scarcity and hence, high fabrication cost which restrict its large-scale production.[168, 169]

1.3.2.3. Transition metal chalcogenide. A variety of electrode materials have emerged to replace noble-metal oxide electrodes. One group of the most explored materials are those based on transition metal chalcogenides. Low cost and distinct oxidation states available for redox reactions makes transition metal chalcogenides an ideal candidate.[170-172]

Previous studies on different electrode materials in energy storage applications revealed unsatisfactory performance, namely low specific capacitance of carbon-based electrodes, inadequate cycling stability of the conducting polymers, high cost of RuO_2, and inferior electrical conductivity of transition metal oxides.[168, 173] The limitations of these electrode materials restricted their rate capability and hinder their practical implementations. Therefore, it is crucial to explore for a novel electrode material with distinguished properties as promising candidate in energy storage purposes.[174]

Recently, the electrochemical properties and the charge storage mechanism of transition metal-based electrodes have been widely investigated. The abundance, low cost, and multiple oxidation states of transition metals, which enables them to have richer redox reaction sites for charge storage process, suggest their potential application in supercapacitors.[175-178]

Specifically, transition metal selenides have been extensively investigated as the electrode materials in electrochemical energy storage systems. Transition metal selenides exbibit chemical properties similar to those of the transition metal oxides and sulfides. This is because of the fact that selenium is the nearest neighbor to oxygen and sulfur in the VI A group. Selenide-based electrodes, however, have lower optical band gap and significantly higher conductivity compared to oxide-based and sulfide-based electrodes, resulting in better energy storage performances. The lower electronegativity of selenide can increase the space between the layers in the crystalline structure and make the transportation of electrons between the layers more convenient. For these reasons, the replacement of sulfur and oxygen with selenium can potentially be an advisable choice.[1-3, 174, 179]

Moreover, doping elements to a binary structure is a known strategy to increase the electrical conductivity as higher redox active sites are introduced for energy storage process. Hence, mixing low cost transition metal chalcogenides is a favorable way to increase the specific surface area, and consequently, enhance the specific capacitance.[133, 180] Recently, ternary nickel cobalt oxide ($NiCo_2S_4$) and ternary nickel cobalt sulfide ($NiCo_2Se_4$) have been extensively studied due to their excellent electrochemical activities. This is mainly attributed to the fact that both $NiCo_2S_4$ and $NiCo_2Se_4$ possess multiple oxide states that enable rich redox reactions originating from both nickel and cobalt ions compared to binary transition metal oxides and selenides such as Ni_3S_4[181-184], Co_3S_4 [184-186], $NiSe_2$[187-189,] and CoSe[190-193]. Therefore, ternary Ni-Co chalcogenides have been selected as an eminent pseudocapacitive material for energy storage devices.[132, 174]

1.3.3. Electrochemical Evaluations. In this section, the electrochemical experiments from which we can evaluate the performance of the electrode as a high-performance supercapacitor are presented.

1.3.3.1. Galvanostatic charge – discharge. Galvanostatic charge – discharge (GCD) is a standard technique to understand the rate capability of the electrode and to test the performance of the active materials and cycle life of supercapacitors under practical operating conditions. During the charge and discharge processes, the working electrode is connected to a constant current source until a preset voltage is reached. Symmetrical shapes of the GCD curves shown in Figure 1.18, verify the reversibility of the electrode.[133, 194]

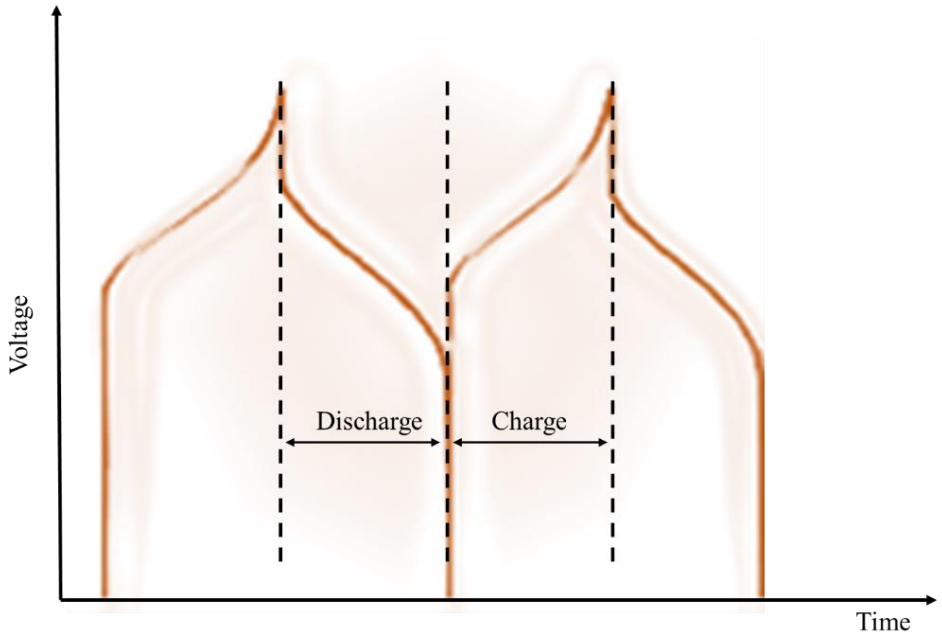

Figure 1.18. A typical galvanostatic charge – discharge process.

From the GCD curves, the specific capacitance (*C*), energy density (*E*), and power density (*P*) of the electrode can be calculated using the following equations:

$$C = \frac{I\ \Delta t}{m\ \Delta V} \tag{4}$$

$$E = \frac{1}{2}\ C\ \Delta V^2 \tag{5}$$

$$P = \frac{E}{\Delta t} \tag{6}$$

where *I* denotes current, *m* denotes the total mass of active materials, *Δt* denotes the discharge time, *ΔV* denotes the potential window, and *C* is in F g^{-1}. [133, 194]

1.3.3.2. Cyclic voltammetry. The cyclic voltammetry (CV) technique can be used to carry out the material capacitance measurements and to identify the capacitance behavior. It is also useful in determining whether the electrode is following a double layer capacitance behavior in non-faradaic region or it is a pseudocapacitance reaction in faradaic region. As seen in Figure 1.19, a CV technique can determine if a broad redox peak (cathodic peak) appears, which will suggest a reversible charge storage process.[140]

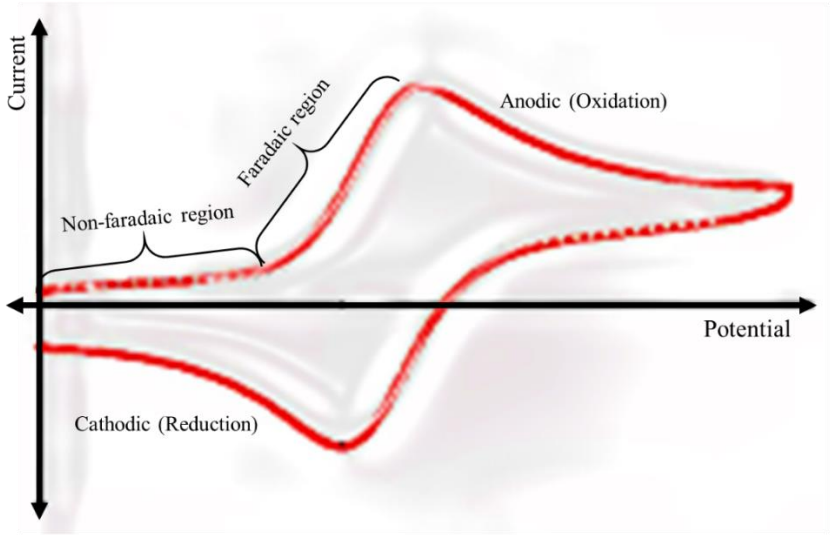

Figure 1.19. Cyclic voltammetry test.

1.3.3.3. Electrochemical impedance spectroscopy. The capacitive performance and reaction kinetics of the electrode can be evaluated using electrochemical impedance spectroscopy (EIS) measurements presented in the form of Nyquist plots. In this method, the configuration of the equivalent circuit model must be outlined to be able to analyze the impedance spectra. In an EIS curve, a semicircle, corresponding to the high-frequency region and a sloped line, corresponding to the low-frequency region should be observed (Figure 1.20). Based on the diameter of the semicircle and the value of charge transfer resistance, denoted as R_{ct}, can be evaluated. R_{ct} is related to the charge transfer process on the interface between the electrode and electrolyte. Also, the intercept on the real axis (Z_{Re}) in high-frequency region represents the internal resistance. *Rs* is the combination of the ionic resistance of the electrolyte, the inner resistance of the electrode material, and the resistance between the current collector and the electrode.[140, 142, 195]

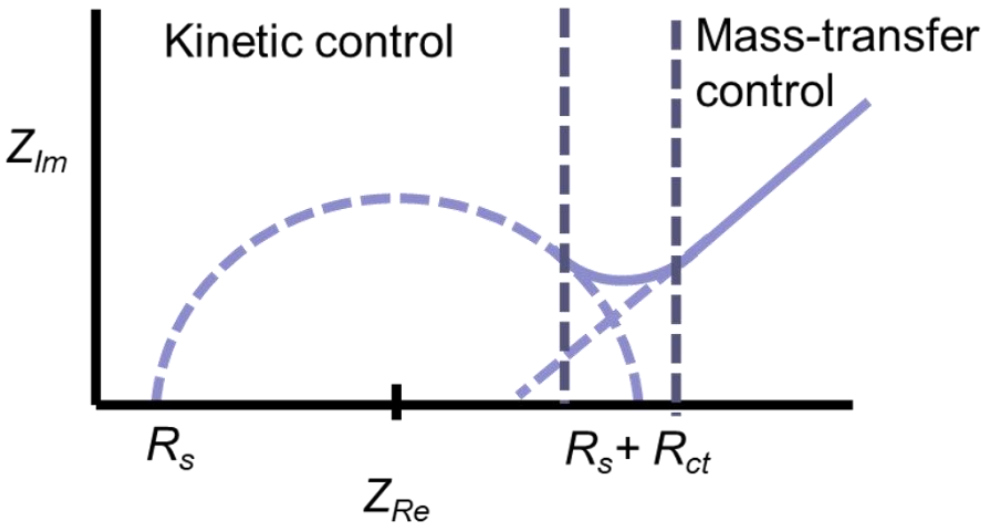

Figure 1.20. Nyquist plot representing the EIS analysis.

In the work presented in Paper IV of this dissertation, $NiCo_2Se_4$/rGO on Ni foam electrode is evaluated for applications in supercapacitors. This study proves that the excellent electrochemical performance of the $NiCo_2Se_4$/rGO is attributed to the excellent pseudocapacitance behavior of $NiCo_2Se_4$ in combination with the high conductive rGO. The proposed electrode can be employed as a promising candidate for high energy- and power-density electrode in energy storage applications.

1.4. ONGOING PROJECT

As indicated in Table 1.1, Ni in +3 oxidation state induces the conversion of glucose molecule to glucolactone. In $CoNi_2Se_4$, most of the Ni is in +3 oxidation state, resulting in a high sensitivity in the process of glucose oxidation. We have also combined $CoNi_2Se_4$ with reduced graphene oxide (rGO) to further boost the conductivity and electron transfer and increase the specific surface area.

To further highlight the effect of decreasing the anion electronegativity and hence, lowering the potential needed for glucose oxidation, Ni_3Te_2 was fabricated and studied for its electrocatalytic efficiency in glucose electrooxidation.

Moreover, to evaluate the effect of cation coordination on the electrocatalytic activity, we investigated the usage of Cu_2Se and its performance in non-enzymatic glucose sensing. Unlike nickel-based electrodes, we have not reported the findings of our studies on copper-based electrodes in an article yet. Results of our preliminary experiments on Cu_2Se are provided in the following section.

Copper is the second most studied element for electrochemical bio-sensing after Ni. Cu-based electrodes, similar to Ni-based electrodes, oxidize glucose to glucolactone

relying on redox couple of Cu(III)/Cu(II). However, the electron transport process in Cu(III)/Cu(II) conversion is not as clear as for Ni-based electrodes.[111,119]

Detailed synthesis procedure of electrodeposited Cu_2Se on Ni foam is as follows. Chemical reagents were analytical grade and used as purchased without further purification.

10 mM of Copper sulfate [$CuSO_4$] was measured and transferred in 30 mL of DI water under stirring to prepare a homogenous solution. Then, 10 mM of selenium dioxide [SeO_2] and 25 mM of lithium chloride [LiCl] were added to the mixture and stirred for 10 minutes. N_2 gas was purged to the solution for 20 minutes to avoid the formation of oxide layer. Ni Foam was employed as substrate in electrodeposition. Prior to electrodeposition, Ni foam substrates were cleaned by ultrasonic treatment in diluted HCl and then rinsed with deionized water to ensure clean surface. Cu_2Se was electrodeposited on the substrate by a controlled-potential deposition at - 0.8 V (vs. Ag/AgCl) at room temperature for 300 seconds.

As shown in Figure 1.21, CV was employed to characterize the electrocatalytic activity of Cu_2Se-NF electrodes towards glucose oxidation in alkaline medium at different scan rates. It is observed that the current density clearly rises with increasing the scan rate, suggesting a diffusion-controlled reaction at the surface of the electrode. Moreover, as provided in Figure 1.22, upon addition of 1.0, 2.0, 3.0, 4.0 and 5.0 mM of glucose, Cu_2Se-NF electrode exhibited substantial increase in current density.

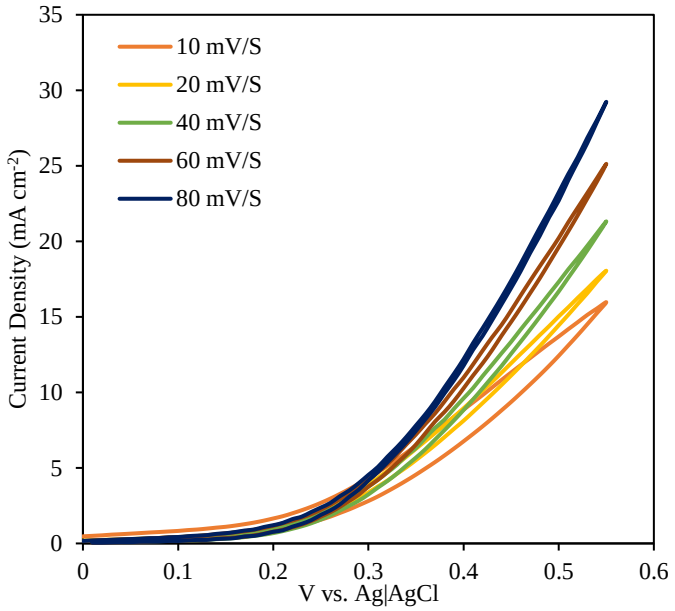

Figure 1.21. CVs obtained from Cu_2Se-NF electrode at different scan rates.

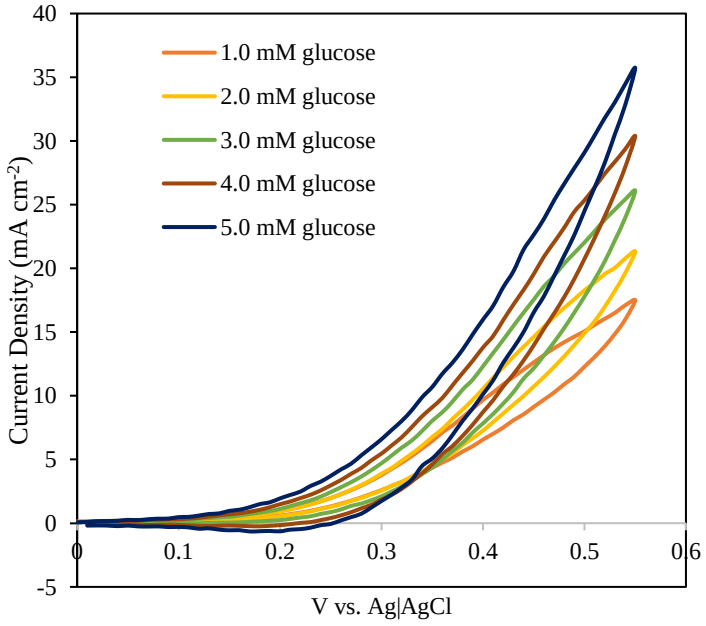

Figure 1.22. CVs of Cu_2Se-NF in presence of different concentrations of glucose.

As shown in Figure 1.23, it is obvious that the current density increases noticeably at the applied potential of +0.45 V vs. Ag|AgCl in presence of 1.0 mM glucose. Therefore, the working potential is chosen to be at 0.45 V. Upon successive addition of varying concentrations of glucose, significant and quick responses are observed for Cu_2Se-NF electrode (Figure 1.24). The calibration plot, provided in Figure 1.25, shows a wide linear range from 10 μM to 7.0 mM (R = 0.9988) with a sensitivity of 5.2897 mA mM^{-1} cm^{-2}.

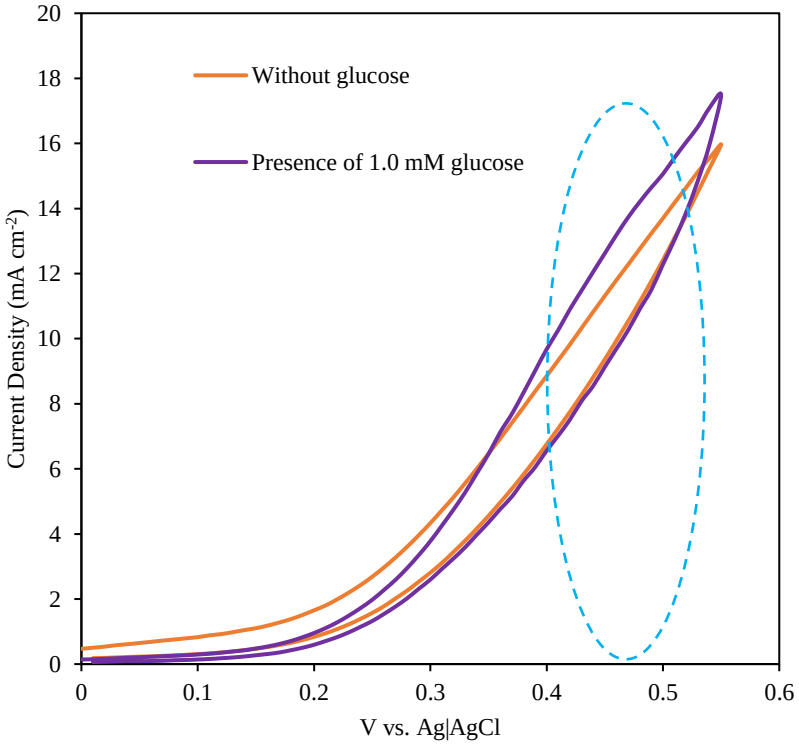

Figure 1.23. Comparisons between CVs of Cu_2Se-NF in the absence and presence of glucose.

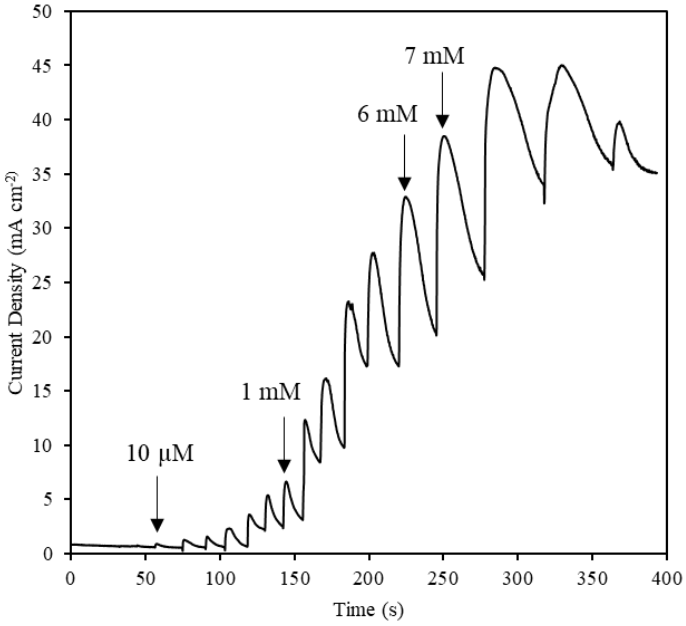

Figure 1.24. Amperometric response to successive addition of glucose.

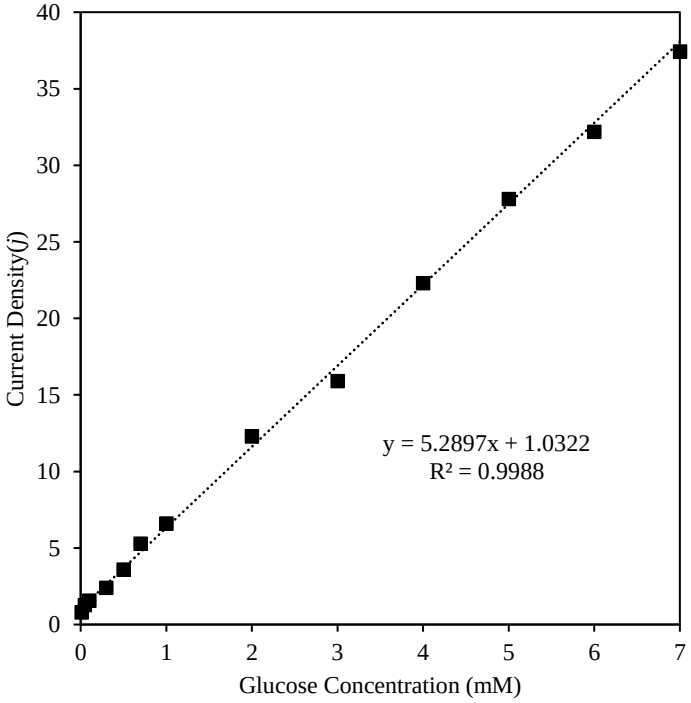

Figure 1.25. Calibration curve of Cu_2Se-NF.

The following list shows our publications, where the usage of transition metal chalcogenide is discussed for full water splitting, non-enzymatic glucose sensing, and supercapacitors.

1. B. G. Amin, A. T. Swesi, J. Masud, and M. Nath, "$CoNi_2Se_4$ as an Efficient Bifunctional Electrocatalyst for Overall Water Splitting," *Chemical Communications*, vol. 53, issue 39, pp. 5412-5415, 2017.
2. B. G. Amin, J. Masud, and M. Nath, "A Non-Enzymatic Glucose Sensor Based on $CoNi_2Se_4$ /rGO Nanocomposite with Ultrahigh Sensitivity at Low Working Potential," *Journal of Materials Chemistry B*, vol. 7, issues 14, pp. 2338-2348, 2019.
3. B. G. Amin, U. De Silva, and M. Nath, "Ultrasensitive and Highly Selective Ni_3Te_2 as a Non-Enzymatic Glucose Sensor at Extremely Low Working Potential," *ACS Omega*, under review.
4. B. G. Amin, J. Masud, and M. Nath, "Facile One-Pot Synthesis of $NiCo_2Se_4$/rGO on Ni Foam for High Performance Hybrid Supercapacitor," *Journal of Power Sources*, to be submitted.

PAPER

I. $CoNi_2Se_4$ AS AN EFFICIENT BIFUNCTIONAL ELECTROCATALYST FOR OVERALL WATER SPLITTING

Bahareh Golrokh Amin, Abdurazag T. Swesi, Jahangir Masud, and Manashi Nath

Department of Chemistry, Missouri University of Science and Technology, Rolla, MO 65409

ABSTRACT

$CoNi_2Se_4$ with a vacancy-ordered spinel structure shows excellent bifunctional electrocatalytic activity for water splitting in alkaline medium producing 10 mA cm^{-2} at a cell voltage of 1.61 V. For OER, an overpotential of 160 mV was needed for 10 mA cm^{-2} which is one of the lowest overpotentials reported to date.

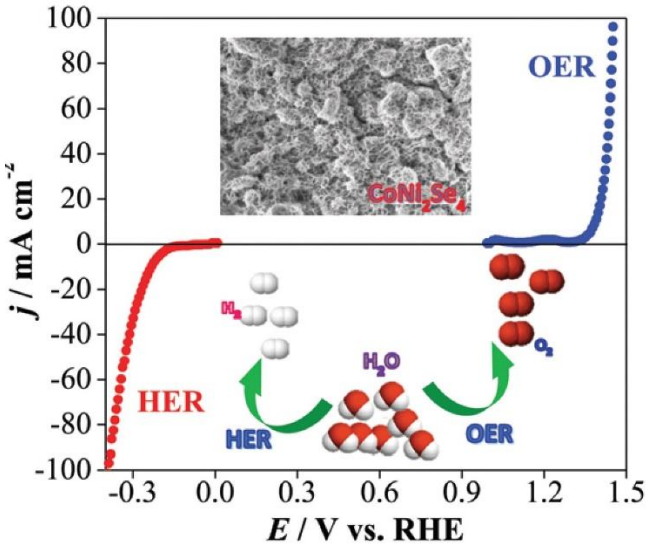

Water electrolysis has taken a center stage in the recent quest for alternative sustainable energy, since it provides clean energy with minimal environmental impact.[1, 2] Water splitting comprises both the oxygen evolution reaction (OER) and hydrogen evolution reaction (HER).[3-6] In fact, it is one of the most promising approaches to produce pure molecular hydrogen,[7-12] an ideal fuel with high energy density and excellent energy conversion efficiency with zero CO2 emission.[8, 13] However, the kinetically sluggish four electron oxygen evolution reaction limits the rate of water electrolysis at low applied potentials.[14-16] A well-designed OER electrocatalyst can lower the applied potential and hence can expedite the overall process.[17] Although OER catalysts have been over-represented with noble metal based compositions such as IrO_x and RuO_x,[18, 19] recently, there has been a lot of progress in nonprecious metal based OER electrocatalysts. Of these the selenide based OER electrocatalysts have made quite an impact due to their superior performance in terms of lowering the overpotential and increasing the current density.[17, 20-26]

Mixed metal selenides are expected to show better catalytic activity due to the possibility of charge delocalization between the metal cations through d–d overlap within the crystalline lattice thereby increasing the Lewis acidity and subsequently the adsorption rate of hydroxyl species on the catalyst surface. It is also believed that the high electrical conductivity for electron delocalization between cations with mixed valence could offer facile donor–acceptor chemisorption sites for reversible adsorption of oxygen.[27] Accordingly, Ni-Co-oxides have outperformed the OER catalytic activity of Ni-oxides.[27-31] In the mixed metal chalcogenide family also transition metal doped chalcogenides have shown efficient OER catalytic activity in alkaline medium.[32, 33]

However, efficient OER catalytic activity in ordered ternary selenides with well-defined stoichiometry is still rare.

In this communication, we have reported the OER catalytic activity of $CoNi_2Se_4$ for the first time, which shows an overpotential of 160 and 210 mV at 10 and 50 mA cm^{-2}, respectively, which represents one of the lowest overpotentials reported to date. Besides the excellent OER catalytic activity, $CoNi_2Se_4$ also shows efficient HER catalytic activity exhibiting an overpotential of only 220 mV to deliver 10 mA cm^{-2}. The potential required for the overall water splitting with this bifunctional catalyst was estimated to be 1.61 V at 10 mA cm^{-2}.

Previously, nickel cobalt-based oxide and sulfide have been reported for OER catalytic activity albeit with higher overpotential.[32-38] However, this is the first report on the bifunctional catalytic activity of spinel type vacancy-ordered $CoNi_2Se_4$. Even in its pristine state $CoNi_2Se_4$ outperforms any other ternary selenides OER electrocatalysts known to date. $CoNi_2Se_4$ was synthesized by electrodeposition on various conducting substrates including carbon fiber paper (CFP) as well as Au-coated glass. Growing the catalytic films directly by electrodeposition offers the advantage of producing binder and other additive-free films, which can thus utilize the catalyst's full potential. The as-grown films were characterized through scanning electron microscopy (SEM), powder X-ray diffraction (PXRD), and X-ray photoelectron spectroscopy (XPS) to confirm their structure and morphology, while the OER and HER catalytic activities were studied through electrochemical measurements. The details of the synthesis procedure, sample preparation and instrumental details have been provided in the ESI.†

The composition of the electrodeposited film was confirmed using PXRD as shown in Figure 1a which revealed that the film was indeed crystalline and the diffraction peaks matched with the standard diffraction pattern of $CoNi_2Se_4$ (JCPDS No: 04-006-5239). SEM image of the electrodeposited film showed that it was a granular, rough film with nanoflake-like morphology (Figure 1b) and there was uniform coverage on the substrate. As can be seen from the SEM image, the nanoflakes were quite thin (B50 nm) and randomly oriented providing a high surface area for the film. The elemental composition analyzed using energy dispersive X-ray spectroscopy (EDS) confirmed that the film was indeed composed of Ni, Co, and Se (Figure S1, ESI†) with an approximate elemental ratio of 2 : 1 : 4 (Ni : Co : Se).

TEM studies also confirmed the nanostructured morphology of the electrodeposited film (Figure S2a, ESI†), while the SAED pattern revealed the crystalline nature of the nanoparticle ensemble (Figure S2b, ESI†). The chemical composition of the electrodeposited film was further characterized by X-ray photoelectron spectroscopy, XPS. All binding energies for Ni, Co and Se were calibrated with respect to C 1s (284.5 eV) as a reference binding energy. The chemical composition and the oxidation state of the catalyst were investigated from the deconvoluted XPS spectra, and the corresponding results are presented in Figure 1c-e. The deconvoluted Ni 2p and Co 2p confirmed the presence of mixed valence of metal ions which might play a significant role in their catalytic activity.[39] As shown in Figure 1c, the binding energies of around 777.6 and 794.2 eV of Co 2p are assigned to Co^{3+} and of 780.2 and 795.5 eV are attributed to Co^{2+} with its shake-up satellite peaks at 785.2 and 800.5 eV.[40, 41]

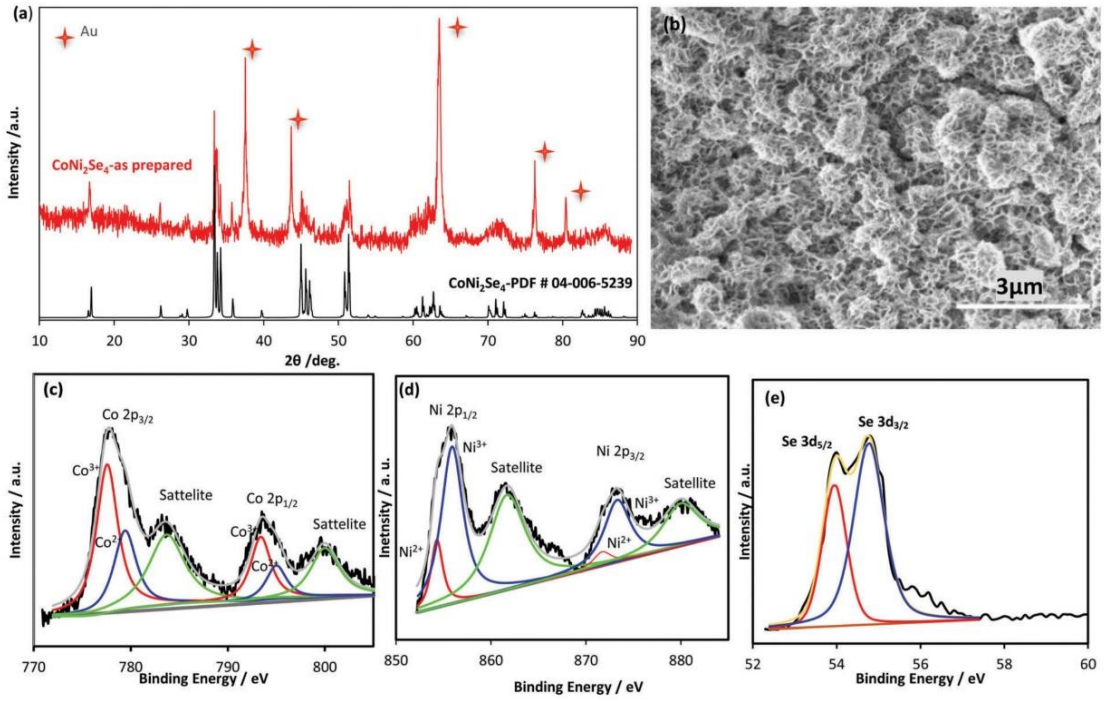

Figure 1. Characterization techniques for $CoNi_2Se_4$. (a) PXRD pattern of the electrodeposited film confirming the formation of $CoNi_2Se_4$. (b) SEM image of the as-synthesized film showing formation of nanoflakes. Deconvoluted XPS spectra of (c) Co 2p, (d) Ni 2p and (e) Se 3d collected from the as-synthesized catalyst.

Similarly, in the Ni 2p spectra (Figure 1d), the peaks at 854.3 and 871.8 eV correspond to Ni^{2+} while those at 856.1 and 873.3 eV corroborate with Ni^{3+}. [42,43] In the Se 3d XPS spectrum in Figure 1e, the peaks at 54.0 and 54.9 eV correspond to Se $3d_{5/2}$ and Se $3d_{3/2}$, respectively, which were comparable with the binding energies commonly observed in the transition metal selenides.[44]

The approximate percentage of variable oxidation states of Co^{2+}/Co^{3+} and Ni^{2+}/Ni^{3+} was calculated from the area of deconvoluted spectra corresponding to Co 2p and Ni 2p peaks (Figure 1c and d). It was found that the as prepared catalyst contained 10% of Co^{3+}, 20% of Co^{2+}, 14% of Ni^{2+}, and 56% of Ni^{3+}. Accordingly, the composition of the film can be written as $Co_{1-x}Ni_x(Ni_{2-y}Co_y)Se_4$ where x = 0.4 and y = 0.3.

The vacancy ordered spinel structures are generally represented as AB_2Se_4 where A is a divalent cation while B is a trivalent cation.[45] However, it has frequently been observed that there can be cation substitution both in the divalent and trivalent sites leading to mixed valence of both cations.[46]

It seems that in the present case, there is substantial mixing both in the A and the B sites with Ni^{3+} predominantly occupying the B site while the A site is predominantly occupied by Co^{2+}. There is nominal substitution of Ni^{2+} in the A site and Co^{3+} in the B site.

It must be noted here that this is one of the few examples of Ni-containing OER catalysts which contains Ni^{3+} in the nascent state, while in other reported catalysts, Ni^{3+} is generated in situ through a pre-catalytic oxidation state. The electrocatalytic activity of $CoNi_2Se_4$ was measured in 1 M KOH utilizing a three-electrode cell, with Pt as the counter, Ag|AgCl as the reference, and $CoNi_2Se_4$ as the working electrode. The electrocatalytic activity was investigated through linear sweep voltammetry (LSV), while the catalyst stability was estimated from constant voltage chronoamperometry measurements.

The electrochemically active surface area (ECSA) as shown in Figure 2 was determined by measuring the double layer charging current at different scan rates following a procedure reported elsewhere[20] and given in the ESI. † For comparison, RuO_2 was also electrodeposited and the electrocatalytic activity was measured in the same solution. All the plots have been shown after *iR* correction.

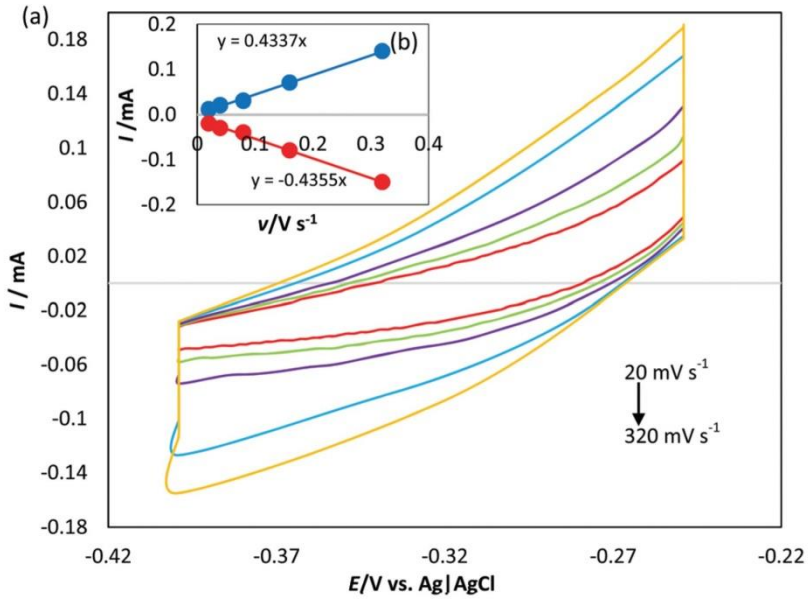

Figure 2. Electrochemical active surface area of $CoNi_2Se_4$. (a) CV measured for the $CoNi_2Se_4$ catalyst in N_2 saturated 1.0 M KOH solution at different scan rates. (b) Anodic and cathodic current measured at 0.32 V as a function of scan rates.

The OER polarization plot of the $CoNi_2Se_4$ electrode measured in 1 M KOH solution at a scan rate of 10 mV s^{-1} has been shown in Figure 3a. As can be seen from the LSV plot, $CoNi_2Se_4$ was indeed active for OER and showed a low onset potential of 1.34 V vs. RHE. For $CoNi_2Se_4$, the current density increased very rapidly and 50 mA cm^{-2} was achieved at an overpotential of 210 mV indicating superior catalytic activity over RuO_2 (360 mV at 10 mA cm^{-2}). This overpotential is one of the lowest values that has been reported in Ni-based chalcogenide systems for OER activity (see Table ST1 in the ESI†). In order to study the effect of substrates, the OER catalytic activity of CoNi2Se4 on different substrates [Au–glass, carbon fiber paper (CFP), carbon cloth (CC)] was measured as shown in Figure S3 (ESI†).

It can be observed that $CoNi_2Se_4$ showed comparable activity in all the substrates with the best being on carbon fiber paper (CFP) possibly due to the porous nature and high surface area of the substrate. High OER catalytic activity of $CoNi_2Se_4$ was also confirmed from the Tafel plot which showed a modest slope of 72 mV decade1 as shown in Figure 3b.

The stability of the catalyst for an extended period of time under the operational conditions is a crucial factor to evaluate the practical usability of the catalyst. Chronoamperometric measurement, where the potential was held constant at 1.38 V vs. RHE to achieve a current density of 8.0 mA cm^{-2}, was performed to estimate the stability of the catalyst for 10 h. As can be seen from Figure 3c, the current density was more or less constant for 10 h with more than 95% of the initial current being preserved and the loss was negligible. These results indicate that the catalytic activity of $CoNi_2Se_4$ was preserved for extended hours of operation in N_2 saturated 1.0 M KOH.

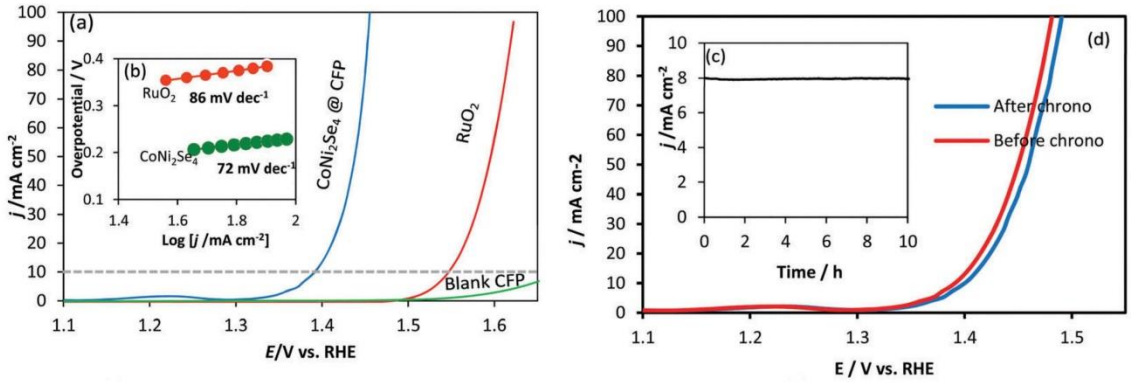

Figure 3. Electrocatalytic performance and stability of $CoNi_2Se_4$ on CFP for OER. (a) LSV curves of $CoNi_2Se_4$ and RuO_2 in 1 M KOH at a scan rate of 10 mV s^{-1} for OER. (b) Tafel plots of $CoNi_2Se_4$ @ CFP and RuO_2. (c) Chronoamperometry plot for $CoNi_2Se_4$ for 10 h at 1.38 V applied potential. (d) Comparison of LSVs before and after 10 h stability in 1 M KOH.

The stability of the catalyst was also confirmed by re-measuring the catalytic activity after 10 h of chronoamperometric study, which showed no change in the onset potential and overpotential (Figure 3d). The compositional stability of the catalyst after 10 h of chronoamperometry was also demonstrated by the PXRD pattern which showed the presence of only $CoNi_2Se_4$ and no other peaks corresponding to free metals or their oxides (Figure S4, ESI†).

EDS analysis (after stability, Figure S5, ESI†) confirmed the overall compositional stability of the catalyst. The composition of the post catalytic activity sample was also confirmed through XPS which showed no change in the Ni, Co and Se binding energies (Figure S6, ESI†). The electrocatalytic activity of $CoNi_2Se_4$ for hydrogen evolution reaction (HER) at the cathode in an alkaline electrolyte was also investigated. It was observed that $CoNi_2Se_4$ showed decent catalytic activity for HER in N_2-staurated 1 M KOH as shown in Figure 4a. LSV for $CoNi_2Se_4$ showed an overpotential of 220 mV for achieving a cathodic current density of 10 mA cm^{-2}.

The stability of the catalyst was checked under continuous operation for 6 h (Figure 4b) at an applied potential of 0.23 V vs. RHE. As can be seen from the chronoamperometry plot, there was minimal variation in the current density, and the LSV plot showed almost similar behavior before and after chronoamperometry. In summary, the bifunctional catalytic activity of electrodeposited $CoNi_2Se_4$ nanoflakes for OER and HER has been reported for the first time.

The simple one-step synthesis by electrodeposition of stoichiometric $CoNi_2Se_4$ enables reproducibility and scalability. Detailed electrochemical measurements revealed superior catalytic activity of $CoNi_2Se_4$ for both OER and HER where only 160 and 220

mV overpotentials were required to achieve 10 mA cm^{-2} (OER and HER, respectively). The observed overpotential for OER is one of the lowest that has been reported to date. Based on compositional analysis, it can be inferred that the presence of Ni^{3+} in the as-synthesized catalyst composition has a positive influence in reducing the overpotential for oxygen evolution to a very low value. $CoNi_2Se_4$ can be applied as both anode and cathode catalysts in a full water electrolysis system, and it requires a potential of only 1.61 V to deliver a current density of 10 mA cm^{-2} through overall water splitting. The catalyst showed high functional and compositional stability for an extended period of time which is a necessary parameter for evaluation of an electrocatalyst. $CoNi_2Se_4$ exposed a new path for the exploration of using mixed transition metal selenide nanostructures, specifically those containing Ni^{3+}, as an economical and efficient bifunctional catalyst for overall water splitting.

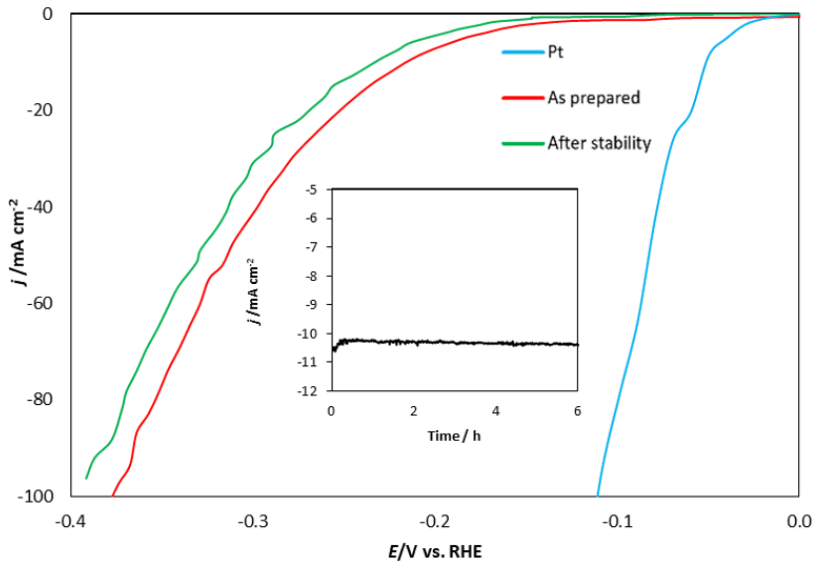

Figure 4. HER performance and stability of $CoNi_2Se_4$ on CFP. (a) LSV curves for $CoNi_2Se_4$ @ Au/glass and Pt in 1.0 M KOH at a scan rate of 10 mV s^{-1} for HER. (b) Chronoamperometry at 0.23 V (vs. RHE) for continuous HER in 1.0 M KOH for 6 h.

REFERENCES

1. N. S. Lewis, G. Crabtree, A. J. Nozik, M. R. Wasielewski and P. Alivisatos, Basic Research Needs for Solar Energy Utilization, *Report of Department of Energy*, USA, 2005.

2. M. G. Walter, E. L. Warren, J. R. McKone, S. W. Boettcher, Q. Mi, E. A. Santori and N. S. Lewis, *Chem. Rev.*, 2010, 110, 11.

3. Q. Yin, J. M. Tan, C. Besson, Y. V. Geletii, D. G. Musaev, A. E. Kuznetsov, Z. Luo, K. I. Hardcastle and C. L. Hill, *Science*, 2010, 328, 328.

4. M. W. Kanan and D. G. Nocera, *Science*, 2008, 321, 1072.

5. D. Merki and X. Hu, *Energy Environ. Sci.*, 2011, 4, 3878.

6. H. B. Gray, *Nat. Chem.*, 2009, 1, 7.

7. J. A. Turner, *Science*, 2004, 305, 972.

8. Y. Zheng, Y. Jiao, M. Jaroniec and S. Qiao, *Angew. Chem., Int. Ed.*, 2015, 54, 52.

9. H. Wang, H. W. Lee, Y. Deng, Z. Lu, P. C. Hsu, Y. Liu, D. Lin and Y. Cui, *Nat. Commun.*, 2015, 6, 7261.

10. X. Zhang, H. Xu, X. Li, Y. Li, T. Yang and Y. Liang, *ACS Catal.*, 2016, 6, 580.

11. X. Lv, Y. Zhu, H. Jiang, X. Yang, Y. Liu, Y. Su, J. Huang, Y. Yao and C. Li, *Dalton Trans.*, 2015, 44, 4148.

12. L. Kuai, J. Geng, C. Chen, E. Kan, Y. Liu, Q. Wang and B. Geng, *Angew. Chem., Int. Ed.*, 2014, 53, 7547.

13. M. G. Walter, E. L. Warren, J. R. McKone, S. W. Boettcher, Q. Mi, E. A. Santori and N. S. Lewis, *Chem. Rev.*, 2010, 110, 6446.

14. F. Lin and S. W. Boettcher, *Nat. Mater.*, 2014, 13, 81.

15. K. Zeng and D. Zhang, *Prog. Energy Combust. Sci.*, 2010, 36, 307.

16. Y. Liu, H. Cheng, M. Lyu, S. Fan, Q. Liu, W. Zhang, Y. Zhi, C. Wang, C. Xiao, S. Wei, B. Ye and Y. Xie, J. Am. *Chem. Soc.*, 2014, 136, 15670.

17. I. H. Kwak, H. S. Im, D. M. Jang, Y. W. Kim, K. Park, Y. R. Lim, E. H. Cha and J. Park, *ACS Appl. Mater. Interfaces*, 2016, 8, 5327.

18. J. Tian, Q. Liu, A. M. Asiri and X. Sun, *J. Am. Chem. Soc.*, 2014, 136, 7587.

19. Y. Lee, J. Suntivich, K. J. May, E. E. Perry and Y. Shao-Horn, *J. Phys. Chem. Lett.*, 2012, 3, 399.

20. A. T. Swesi, J. Masud and M. Nath, *Energy Environ. Sci.*, 2016, 9, 1771.

21. J. Masud, A. T. Swesi, W. P. R. Liyanage and M. Nath, *ACS Appl. Mater. Interfaces*, 2016, 8, 17292.

22. J. Masud, P. Ioannou, N. Levesanos, P. Kyritsis and M. Nath, *Chem. Sus. Chem*, 2016, 9, 3123.

23. D. Kong, H. Wang, Z. Lu and Y. Cui, *J. Am. Chem. Soc.*, 2014, 136, 4897.

24. X. Xu, P. Du, Z. Chen and M. Huang, *J. Mater. Chem. A*, 2016, 4, 10933.

25. Z. Wang, J. Li, X. Tian, X. Wang, Y. Yu, K. A. Owusu, L. He and L. Mai, *ACS Appl. Mater. Interfaces*, 2016, 8, 19386.

26. X. Xu, F. Song and X. Hu, *Nat. Commun.*, 2016, 7, 12324.

27. M. Hamdani, R. Singh and P. Chartier, *Int. J. Electrochem. Sci.*, 2010,5, 556.

28. F. Basharat, U. A. Rana, M. Shahida and M. Serwara, *RSC Adv.*, 2015, 5, 86713.

29. Q. Dong, C. Sun, Z. Dai, X. Zang and X. Dong, *ChemCatChem*, 2016, 8, 3484.

30. Z. Zhang, S. Liu, F. Xiao and S. Wang, *ACS Sustainable Chem. Eng.*, 2017, 5, 529.

31. J. Liang, Y. Z. Wang, C. C. Wang and S. Y. Lu, *J. Mater. Chem. A*, 2016, 4, 9797.

32. Z. Peng, D. Jia, A. M. Al-Enizi, A. A. Elzatahry and G. Zheng, *Adv. Energy Mater.*, 2015, 5, 1402031.

33. D. Liu, Q. Lu, Y. Luo, X. Sun and A. M. Asiri, *Nanoscale*, 2015, 7, 15122.

34. Q. Liu, J. Jin and J. Zhang, *ACS Appl. Mater. Interfaces*, 2013, 5, 5002.

35. A. Sivanantham, P. Ganesan and S. Shanmugam, *Adv. Funct. Mater.*, 2016, 26, 4661.

36. J. Yin, P. Zhou, L. An, L. Huang, C. Shao, J. Wang, H. Liua and P. Xi, *Nanoscale*, 2016, 8, 1390–1400.

37. X. Gao, H. Zhang, Q. Li, X. Yu, Z. Hong, X. Zhang, C. Liang and Z. Lin, *Angew. Chem., Int. Ed.*, 2016, 55, 6290.

38. H. Cheng, Y.-Z. Su, P. Kuang, G.-F. Chen and Z.-Q. Liu, *J. Mater. Chem. A*, 2015, 3, 19314.

39. M. Gao, Y. Xu, J. Jiang, Y. Zheng and S. Yu, *J. Am. Chem. Soc.*, 2012, 134, 2930.

40. C. Jin, F. Lu, X. Cao, Z. Yang and R. Yang, *J. Mater. Chem. A*, 2013, 1, 12170.

41. T. Z. Su, Q. Z. Xu, G. F. Chen, H. Cheng, N. Li and Z. Q. Liu, *Electrochim. Acta*, 2015, 174, 1216.

42. H. Shi and G. Zhao, *J. Phys. Chem. C*, 2014, 118, 25939.

43. E. Umeshbabu, G. Rajeshkhanna, P. Justin and G. Ranga Rao, *RSC Adv.*, 2015, 5, 66657.

44. A. B. Mandale, S. Badrinarayanan, S. K. Date and A. P. B. Sinha, *J. Electron Spectrosc. Relat. Phenom.*, 1984, 33, 61.

45. A. Hayashi, K. Imada, K. Inoue, Y. Ueda and K. Kosuge, *Bull. Inst.Chem. Res.*, Kyoto Univ., 1986, 64, 186.

46. W. Hu, R. Chen, W. Xie, L. Zou, N. Qin and D. Bao, *ACS Appl. Mater. Interfaces*, 2014, 6, 19318.

SUPPORTING INFORMATION

$CoNi_2Se_4$ AS AN EFFICIENT BIFUNCTIONAL ELECTROCATALYST FOR OVERALL WATER SPLITTING

Bahareh Golrokh Amin, Abdurazag T. Swesi, Jahangir Masud, and Manashi Nath

Department of Chemistry, Missouri University of Science and Technology, Rolla, MO 65409.

Experimental and Methods

Materials were reagent grade and were used as received without further purification. Nickel acetate tetrahydrate [Ni $(C_2H_4O_2)_2.4H_2O$ from J. T. Baker chemical company, USA and cobalt acetate tetrahydrate [Co $(C_2H_4O_2)_2.4H_2O$ from Alfa Aesar, SeO_2 [Acros Chemicals] and lithium chloride (LiCl) [Aldrich] were used. Au-coated glass slide (purchased from Deposition Research Lab Incorporated (DRLI), Lebanon, Missouri) and Carbon fiber paper (CFP) and Carbon cloth (CC) (purchased from Fuel cells ETC company, College Station, Texas) were used as substrates in electrodeposition.

Electrodeposition of $CoNi_2Se_4$

The electrolytes were prepared using analytical grade reagents and deionized (DI) water with a resistivity of 18 MΩ·cm. Prior to electrodeposition, Au / glass substrates were cleaned by ultrasonic treatment in micro-90 detergent followed by rinse with isopropanol for three times and eventually rinsed with deionized water (15 min each step) to ensure clean surface. Au-coated glass was covered with a Teflon tape, leaving an exposed geometric area of 0.283 cm^{-2}, and connected as the working electrode.

An IviumStat potentiostat was used to control the electrodeposition process and to monitor the current and voltage profiles. $CoNi_2Se_4$ was electrodeposited on the substrate by a controlled-potential deposition at - 0.8 V (vs. Ag/AgCl) at room temperature from an aqueous solution containing 10 mM Ni $(C_2H_4O_2)_2.4H_2O$, 25 mM Co $(C_2H_4O_2)_2.4H_2O$ and 40 mM SeO_2. The pH of the electrolytic bath was adjusted to ~ 2.5 with dilute HCl. After each electrodeposition, the electrodeposited films were washed with deionized water in order to remove impurities and adsorbents from the surface.

Electrochemical Measurements

Oxygen and hydrogen (OER and HER) evolution reaction was performed in 1M KOH solution by using Iviumstat. Ag|AgCl|KCl (sat.) and Pt mesh were using as reference and counter electrode, respectively. The measured potential vs. the Ag/AgCl was converted to the reversible hydrogen electrode (RHE) via the Nernst equation (eq. 1):

$$E_{RHE} = E\text{Ag|AgCl} + 0.059\text{PH} + E^{o}\ \text{Ag|AgCl} \quad (1)$$

where E_{RHE} is the converted potential vs. RHE, EAg|AgCl is the experimentally measured potential against Ag|AgCl reference electrode, and E^{o} Ag|AgCl is the standard potential of Ag|AgCl at 25^{o} C (0.199 V).

Surface Characterizations

SEM and EDS

A FEI Helios Nanolab 600 FIB/FESEM at an acceleration voltage of 10 kV and a working distance of 5.0 mm was employed to obtain SEM image of the modified

electrode surfaces. Energy dispersive spectroscopy (EDS) accompanied by line scan analysis was also acquired from the SEM microscope.

XRD

The product was characterized through powder X-ray diffraction (PXRD) with Philips X-Pert utilizing CuKα (1.5418Å) radiation. PXRD pattern was collected from the pristine product with no further treatments. Because the product formed a very thin layer on the substrate, the PXRD was collected at grazing angles in thin film geometry (GI mode with Göbel mirrors).

XPS

KRATOS AXIS 165 X-ray Photoelectron Spectrometer using monochromatic Al X-ray source was used for all XPS measurements of the catalyst.

Electrochemically active surface area (ECSA)

The ECSA of the $CoNi_2Se_4$ can be determine by measuring the double layer charging current at different scan rates following here:

$$ECSA = C_{DL}/C_s \quad (2)$$

where C_s is the specific capacitance (0.040 mF cm^{-2}) in N_2 saturated 1 M KOH solution. Cs is the specific capacitance which is reported in a range between 0.022 to 0.130 mF cm^{-2} in alkaline solutions.[S1] Here, the value of 0.040 mF cm^{-2} was used based on previously reported Ni-based OER catalysts.[S1] C_{DL} was calculated as a slop of the plot of capacitive

current (i_{DL}) from a non-faradaic double-layer region against scan rate v (V s^{-1}). The ECSA was measured to be 10.8 cm^{-2} on CFP.

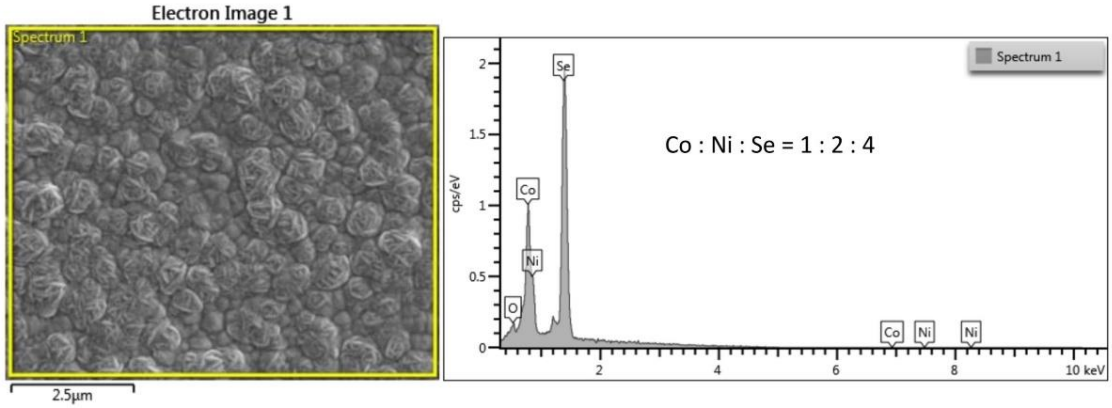

Figure S1. Elemental analysis of as prepared $CoNi_2Se_4$ by using EDS.

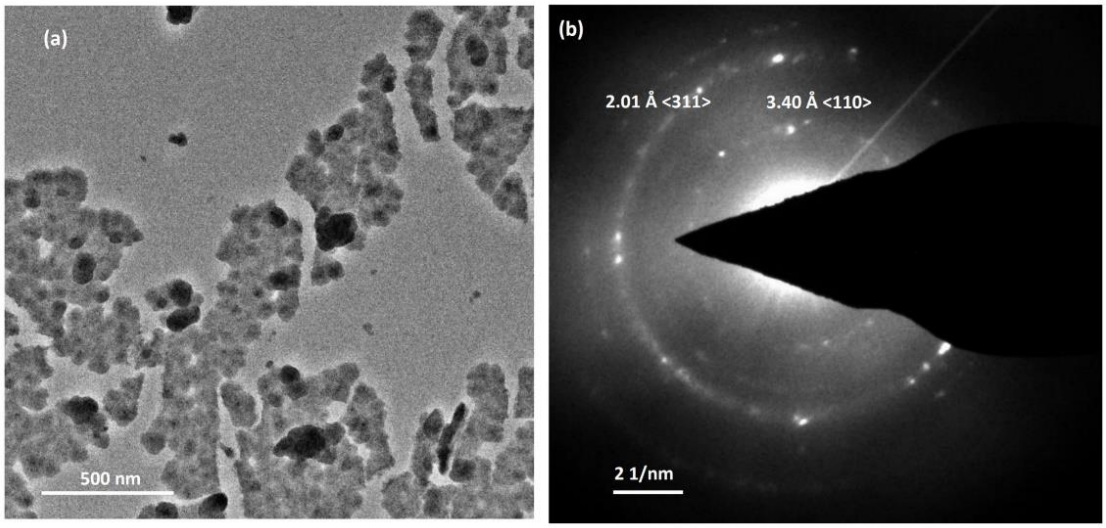

Figure S2. TEM image (a) and SAED pattern (b) of $CoNi_2Se_4$ catalyst.

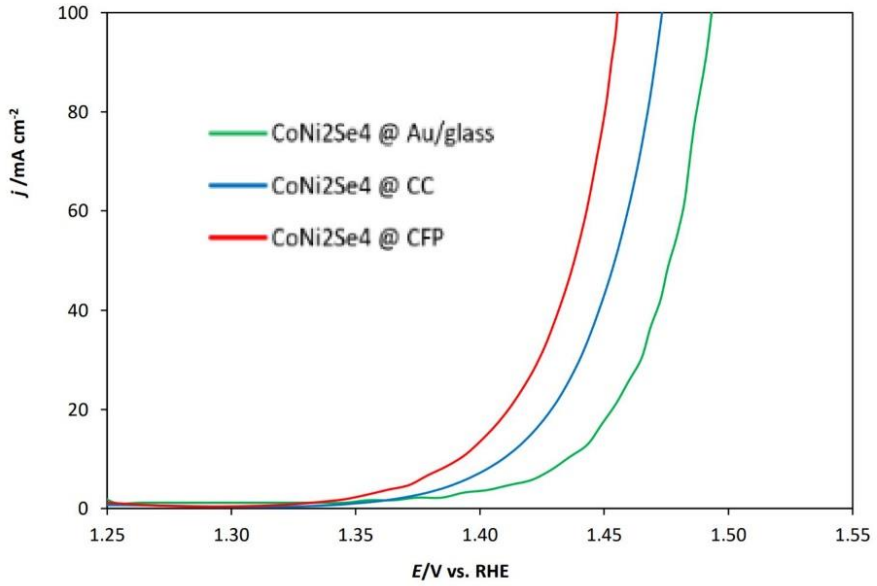

Figure S3. Comparison of OER catalytic activity of $CoNi_2Se_4$ grown on different substrates. All measurements were done in 1M KOH solution.

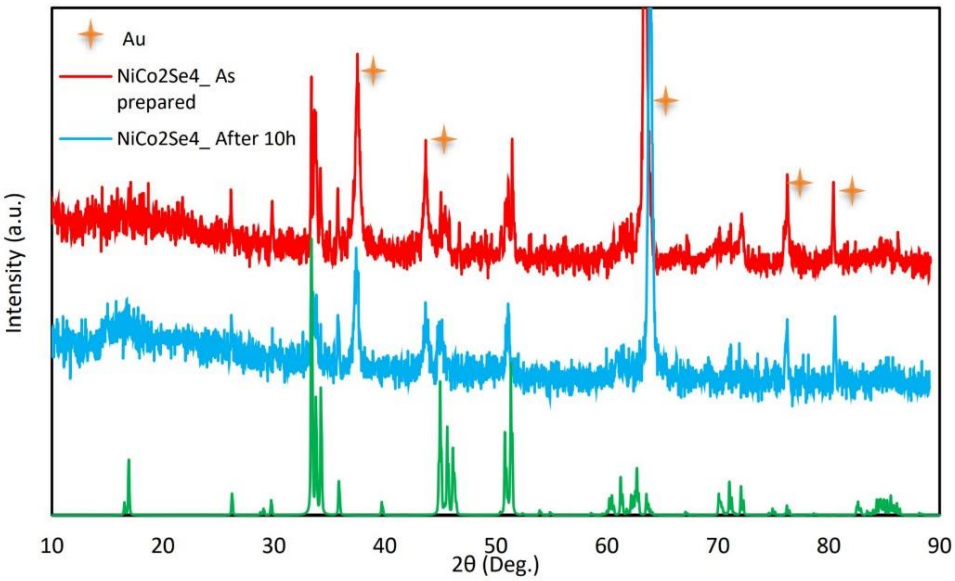

Figure S4. Comparison of PXRD before and after chronoamperometry.

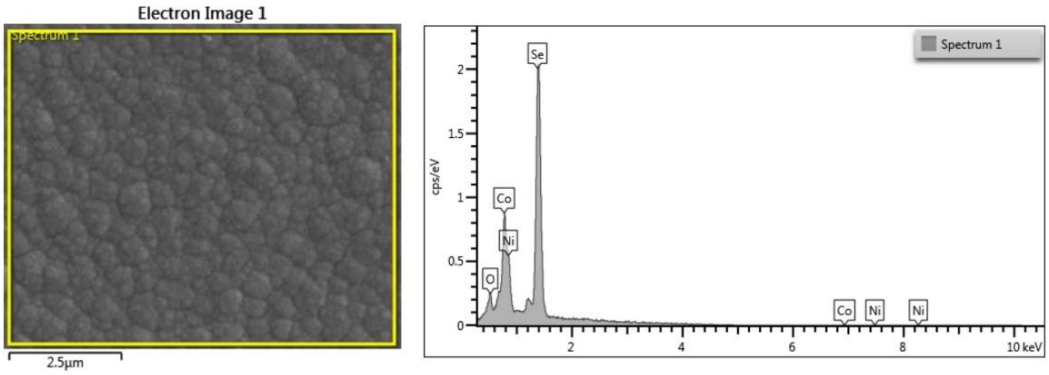

Figure S5. EDS analysis after 10h of chronoamperometry.

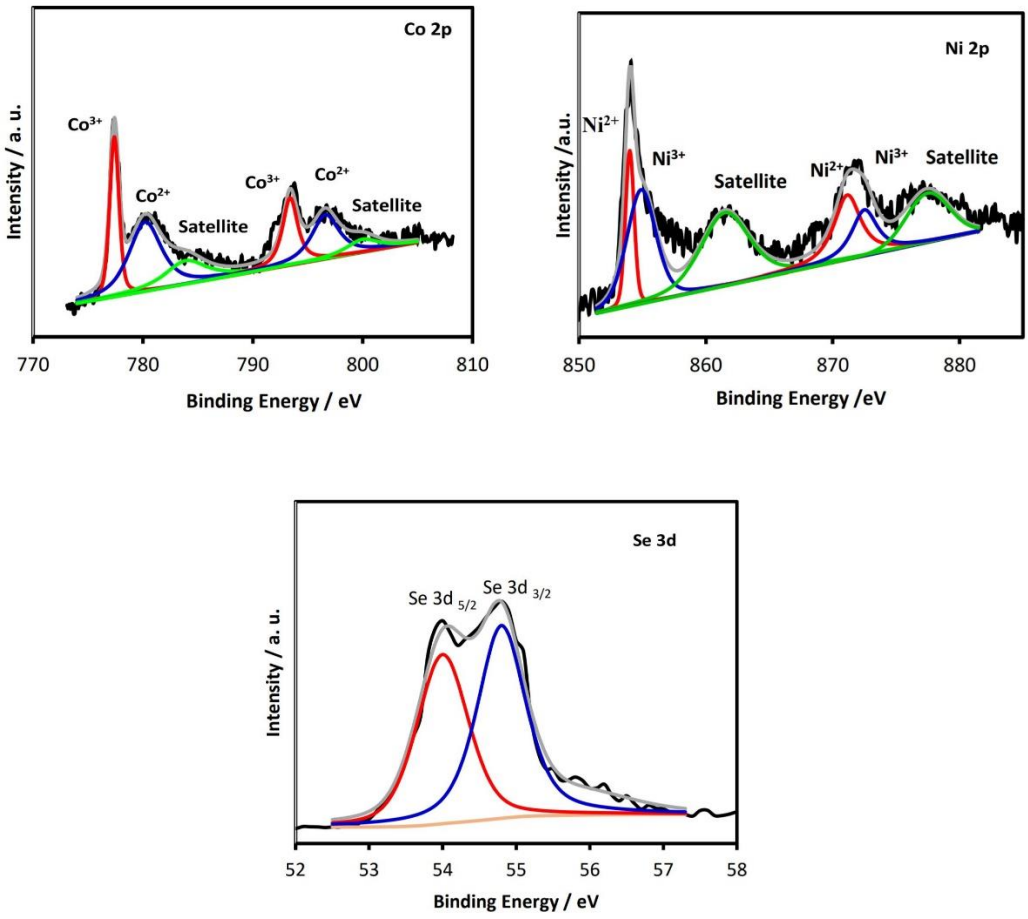

Figure S6. Comparison of XPS (Ni 2p, Co 2p and Se 3d) before and after Chronoamperometry for 10h.

Table S1. Comparison of OER activity of the $CoNi_2Se_4$ @ C.P. with recently reported catalysts.

Electrocatalyst	Catalyst Loading	Electrolyte	Overpotential (mV *vs.* RHE) @ 10[a], 20[b] or 50[c] mA cm-2	Ref.
$NiCo_2Se_4$@CFP	**4.7 mg cm^{-2}**	**1 M KOH**	**160[a], 210[c]**	**This work**
$NiCo_2S_4$@graphene	-	0.1 M KOH	470[a]	S2
$NiCo_2S_4$ NA/CC	4.0 mg cm^{-2}	1 M KOH	340 mV (100 mA cm^{-2})	S3
$NiCo_2S_4$ NW/NF	-	1 M KOH	260[a]	S4
$NiCo_2O_4$ hollow microcuboids	~1 mg cm^{-2}	1 M NaOH	290[a]	S5
Ni-Co-O@Ni-Co-S NA	-	1 M KOH	300[b]	S6
$NiCo_2O_4$	-	1 M KOH	391[b]	S7
(a-CoSe/Ti)	3.8 mg cm^{-2}	1 M KOH	292[a]	S8
$Co_{0.85}Se$	-	1 M KOH	324[a]	S9
$(Ni,CO)_{0.85}Se$	-	1 M KOH	255[a]	S9
$Co_{0.13}Ni_{0.87}Se_2$/Ti	1.67 mg cm^{-2}	1 M KOH	320 mV (100 mA cm^{-2})	S10
$NiSe_2$ /Ti	-	1 M KOH	350 mV (100 mA cm^{-2})	S10
$NiSe_2$	1 mg cm^{-2}	1 M KOH	250[a]	S11
$CoSe_2$	1 mg cm^{-2}	1 M KOH	430[a]	S11
NiS/ Ni foam	-	1 M KOH	335[c]	S12
Ni_3Se_2/Cu foam	-	1 M KOH	343[c]	S13
CoSe/Ti mesh	3.8 mg cm^{-2}	1 M KOH	341[c]	S14
Fe-doped NiSe	4.8 mg cm^{-2}	1 M KOH	264 mV (100 mA cm^{-2})	S15
$Ni(OH)_2$	142 μg cm^{-2}	1 M KOH	313[b]	S16
NiO nanoparticles	-	1 M KOH	347[b]	S16
Amorphous NiO	0.1 mg cm^{-2}	1 M KOH	> 470 [b]	S17
NiO_x/C	-	1 M KOH	335[a]	S18
$(Ni_{0.69}Fe_{0.31}O_x/C)$	-	1 M KOH	280[a]	S18
NiOOH	-	1 M KOH	525[a]	S19
NiCo LDH	~0.17 mg cm^{-2}	1 M KOH	393[b]	S20

REFERENCES

S1. A. T. Swesi, J. Masud, and M. Nath, *Energy Environ. Sci.*, 2016, 9, 1771-1782.

S2. Q. Liu, J. Jin, and Junyan Zhang, *ACS Appl. Mater. Interfaces*, 2013, 5, 5002−5008.

S3. D. Liu, Q. Lu, Y. Luo, X. Sun, and A. M. Asiri, *Nanoscale*, 2015,7, 15122–15126.

S4. A. Sivanantham, P. Ganesan, and S. Shanmugam, *Adv. Funct. Mater.*,2016.

S5. X. Gao, H. Zhang, Q. Li, X. Yu, Z. Hong, X. Zhang, C. Liang, and Zhan Lin, *Angew. Chem. Int. Ed.*, 2016, 55,6290–6294.

S6. W. Xu, Z. Lu, X. Lei, Y. Li, and X.A. Sun, *Phys. Chem. Chem. Phys.*, 2014, 16, 20402–20405.

S7. Z. Peng, D. Jia, A. Al-Enizi, A. Elzatahry, and G. Zheng, *Adv. Energy Mater.*, 2015, 5, 1402031-1402038.

S8. T. Liu, Q. Liu, A. M. Asiri, Y. Luo, and X. Sun, *Chem. Commun.*, 2015, 51, 16683.

S9. C. Xia, Q. Jiang, C. Zhao, M.N. Hedhili, H.N. Alshareef, *Adv. Mater.*, 2016, 28, 77–85.

S10. T. Liu, A.M Asiri, and X. Sun, *Nanoscale*, 2016, 8, 3911- 3915.

S11. I.H. Kwak, H.S. Im, D.M. Jang, Y.W. Kim, K. Park, Y.R. Lim, E.H. Cha, and J. Park, J., *ACS Appl. Mater. Interfaces*, 2016, 8, 5327−5334.

S12. W. Zhu, X. Yue, W. Zhang, S. Yu, Y. Zhang, and J. Wang, *Chem. Commun.*, 2016, 52, 1486-1489.

S13. J. Shi, J. Hu, Y. Luo, X. Sun, A.M. Asiri, *Catal. Sci. Technol.*, 2015, 5, 4954-4958.

S14. T. Liu, Q. Liu, A.M. Asiri, Y. Luo, X. Sun, *Chem. Commun.*, 2015, 51, 16683-16686.

S15. C. Tang, A.M. Asiri, and X. Sun, *Chem.Commun.*, 2016, 52, 4529-4532.

S16. L. Stern, and X. Hu, *Faraday Discuss.*, 2014, 176, 363 –379.

S17. Kuai, L.; Geng, J.; Chen, C.; Kan, E.; Liu, Y.; Wang, Q. & Geng, B, *Angew. Chem. Int. Ed.*, 2014, 53, 7547–7551.

S18. Y. Qiu, L. Xin, and W. Li, *Langmuir*, 2014, 30, 7893–7901.

S19. S. Klaus, Y. Cai, M. Louie, L. Trotochaud, and A.T. Bell, *J. Phys. Chem. C*, 2015, 119, 7243-7254.

S20. H. Liang, F. Meng, M. Acevedo, L. Li, A. Forticaux, L. Xiu, Z. Wang, and S. Jin, *Nano Lett.*,2015,15, 1421–1427.

II. NON-ENZYMATIC GLUCOSE SENSOR BASED ON $CoNi_2Se_4$/RGO NANOCOMPOSITE WITH ULTRAHIGH SENSITIVITY AT LOW WORKING POTENTIAL

Bahareh Golrokh Amin, Jahangir Masud, and Manashi Nath

Department of Chemistry, Missouri University of Science and Technology, Rolla, MO 65409

ABSTRACT

Uniform and porous $CoNi_2Se_4$ was successfully synthesized by electrodeposition onto a composite electrode comprising reduced graphene oxide (rGO) anchored on a Ni foam substrate (prepared hydrothermally). This $CoNi_2Se_4$–rGO@NF composite electrode has been employed as an electrocatalyst for the direct oxidation of glucose, thereby acting as a high-performance non-enzymatic glucose sensor. Direct electrochemical measurement with the as-prepared electrode in 0.1 M NaOH revealed that the $CoNi_2Se_4$–rGO nanocomposite has excellent electrocatalytic activity towards glucose oxidation in an alkaline medium with a sensitivity of 18.89 mA mM^{-1} cm^{-2} and a wide linear response from 1 mM to 4.0 mM at a low applied potential of +0.35 V vs. Ag|AgCl. This study also highlights the effect of decreasing the anion electronegativity on enhancing the electrocatalytic efficiency by lowering the potential needed for glucose oxidation. The catalyst composite also exhibits high selectivity towards glucose oxidation in the presence of several interferents normally found in physiological blood samples. A low glucose detection limit of 0.65 mM and long-term stability along with a short response

time of approximately 4 seconds highlights the promising performance of the $CoNi_2Se_4$–rGO@NF electrode for nonenzymatic glucose sensing with high precision and reliability.

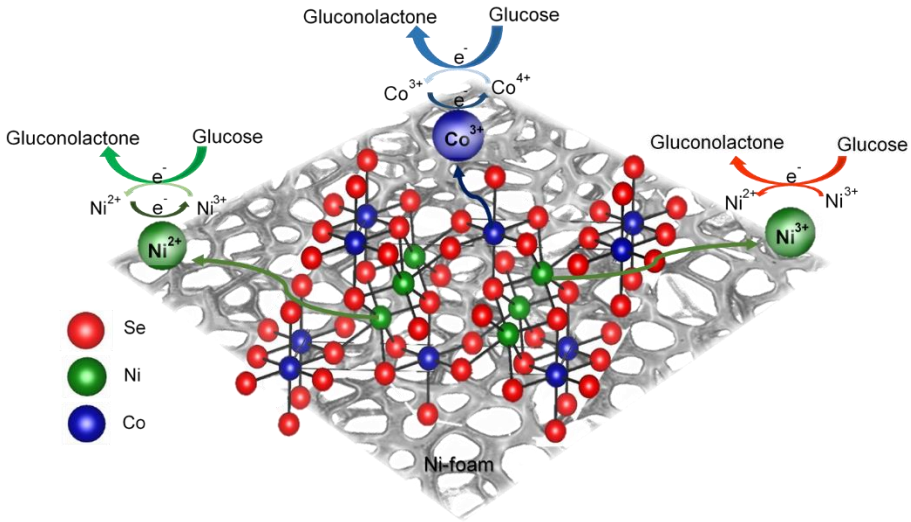

1. INTRODUCTION

Diabetes is a sophisticated and increasingly prevalent condition that affects millions of people worldwide and has become the third main cause of death. Constant monitoring of glucose level is the most effective way of controlling diabetes and preventing life-threatening conditions.[1] Among various methods available for detection of glucose level, electrochemical detection technique based on direct glucose electro-oxidation has received significant recognition over the past few years due to its high sensitivity, low limit of detection, promising response time, and low cost.[2, 3] Out of the two main categories of electrochemical sensors, the traditional enzymatic glucose sensors suffer from several disadvantages including complicated immobilization process of

enzymes, sensitivity to the environmental conditions, poor long-term functional stability of the sensorial device, and high fabrication cost.[4-6] To overcome the intrinsic limitations of enzyme-based devices, researches have intensified investigations on developing non-enzymatic electrochemical glucose sensing, which relies heavily on direct glucose oxidation on the electrode surface.[7,8] The choice of glucose oxidation electrocatalyst plays a crucial role in development of such non-enzymatic glucose sensors. Several redox-active compounds have been used as electrocatalyst for glucose electro-oxidation.[9-14] Recently, transition-metal-based compounds have been extensively explored as suitable glucose sensing candidates due to their high electrocatalytic activity, electrical conductivity, abundancy, and low cost.[15, 16]

Transition metal chalcogenides (TMCs), in particular, have been subjected to intense research in various energy-related applications such as bifunctional electrocatalysts for water splitting [17-20], dye-sensitized solar cells [21-23], Li-ion batteries [24, 25], and supercapacitors.[26-30] The tunable redox-active reaction centers of TMCs improve their electrochemical behavior, while their narrow bandgap and higher degree of covalency leads to better electrical conductivity.[31] Such properties make transition metal chalcogenides significantly better electrocatalysts compared to the respective oxide counterparts, owing to their superior charge transport property and redox tunability, essential for an electrochemical reaction.[32] Among several types of TMC, Ni-based nanomaterials have been extensively investigated due to their desirable electrocatalytic activity in alkaline electrolytes arising from the tunability of the Ni^{2+}/Ni^{3+} redox couple, low toxicity, and low cost.[33-35] Apart from binary selenides, ternary mixed metal selenides have also been explored primarily to study the effect of transition metal doping on the

catalytic activity. Among the ternary selenides, spinel-type compositions having the generic formula AB_2Se_4 has been investigated recently for electrocatalytic activities in water splitting.[17, 36] In these spinels, the Ni atom is frequently stabilized in +3 oxidation state, which is more catalytically active than Ni^{2+}, thereby, increasing their inherent catalytic activity.[17, 37] Similarly, in $CoNi_2Se_4$, while Co and Ni both have octahedral coordination, Ni cation occupies the vacancy ordered sites, while Co cations are present in the fully filled layer, providing several catalytically active sites and numerous pathways for possible charge transport as well as exposure to the electrolyte.[38]

Apart from the catalyst composition, the other aspect of enhancing electrocatalytic efficiency is to increase conductivity of the catalytic composite. In that regards, various carbon-based additives have been used. Graphene being a two-dimensional sheet of a single-atom thick carbon atoms arranged in a hexagonal network with a large specific area and exhibiting excellent thermal and electrical conductivity, has been used as a matrix to boost electron transfer rates and electrocatalytic activities.[39-44]

Inspired by the advantages of $CoNi_2Se_4$ and graphene-based composites as electrocatalysts, in this study, a $CoNi_2Se_4$-rGO composite (rGO = reduced graphene oxide) was pursued as electrocatalyst for glucose oxidation. $CoNi_2Se_4$ was successfully synthesized via single-step electrodeposition directly on composite electrode comprising hydrothermally prepared reduced graphene oxide anchored on Ni foam substrate ($CoNi_2Se_4$-rGO@NF), and was examined for non-enzymatic glucose oxidation for the first time. The developed catalytic composite exhibits an exceptionally high efficiency for glucose oxidation including an extremely low working potential of only 0.35 V vs. Ag|AgCl with superior sensitivity of 18890 μA mM^{-1} cm^{-2}, a wide linear range of 1 μM

to 4.0 mM for glucose detection, a low detection limit of 0.65 µM (S/N = 3), an excellent stability, and a high selectivity in the presence of interfering species. The electrochemical sensing behavior of the $CoNi_2Se_4$-rGO@NF electrode towards glucose sensing was investigated using amperometric techniques and is presented in the following sections.

2. EXPERIMENTAL

2.1. MATERIALS

All reagents were of analytical grade and used as purchased without further purification. Nickel acetate tetrahydrate [Ni $(C_2H_4O_2)_2.4H_2O$ was purchased from J. T. Baker chemical company, USA, cobalt acetate tetrahydrate [Co $(C_2H_4O_2)_2.4H_2O$ was acquired from Alfa Aesar, SeO_2 [Acros Chemicals], lithium chloride (LiCl) [Aldrich], Dextrose [Sigma-Aldrich], Ascorbic acid [Fisher-Scientific], Lactose [Fisher-Scientific], Fructose [Aldrich], Dopamine [Sigma-Aldrich], sodium chloride and potassium chloride [Fisher-Scientific] were all provided and used throughout the experiment. Ni Foam was employed as substrate in electrodeposition. Deionized water (18.2 MΩ cm^{-1}) was used throughout the work.

2.2. SYNTHESIS OF GRAPHENE OXIDE (GO) AND RGO SAMPLES

Graphene oxide (GO) was first prepared by modified Hummers method using natural graphite following reported procedure.[45] Specifically, 10 mg of GO was dispersed in 12 mL of DI water and sonicated for 45 minutes. Then, 3 µL Hydrazine monohydride was added to this dispersion and was sonicated for another 30 minutes. Ni foam was

cleaned using diluted HCL followed by sonication in a mixture of ethanol and deionized water. Both the GO mixture and pre-cleaned Ni foam were transferred into a 23 mL Teflon–lined stainless steel autoclave which was sealed and kept at 145 °C for 8 hours and then naturally cooled to room temperature. The Ni foam containing the rGO ingrown on the surface was taken out and rinsed with DI water and ethanol several times followed by drying in vacuum oven at 40 °C overnight.

2.3. SYNTHESIS OF $CoNi_2Se_4$@NF AND $CoNi_2Se_4$-RGO@NF

As described in our previous work,[17] $CoNi_2Se_4$ can be synthesized by electrodeposition. Similar synthesis strategy was followed in this paper where electrodeposition was carried out from an electrolyte containing 10 mM $Ni(C_2H_4O_2)_2.4H_2O$, 25 mM $Co(C_2H_4O_2)_2.4H_2O$, and 40 mM SeO_2 dissolved in DI water. Dilute HCl was added to the solution to adjust the pH of the electrolytic bath to 2.5. The mixture was stirred and sonicated for 15 minutes to completely disperse and dissolve the precursors, and then, nitrogen gas was purged through the solution for 35 minutes. $CoNi_2Se_4$ was electrodeposited from the electrolytic bath at a potential of -0.8 V (vs. Ag|AgCl) for 600 seconds at room temperature. Electrodeposition was performed on both rGO-coated Ni foam as well as bare Ni foam for comparing the electrocatalytic activities and investigating the influence of rGO. Figure 1 shows a detailed schematic for the growth process of $CoNi_2Se_4$-rGO@NF catalytic composite. After each electrodeposition, as-grown thin films were washed with deionized water to remove impurities and unreacted ions from the surface. For electrochemical measurements, the prepared

electrode was covered with a Teflon tape, leaving an exposed geometric area of 0.283 cm^2.

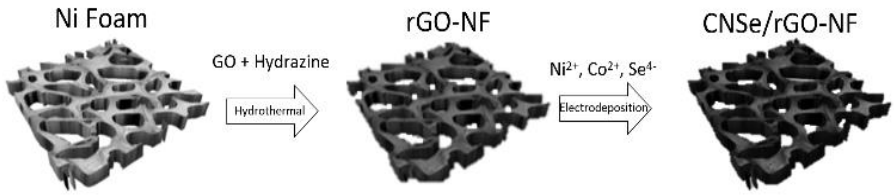

Figure 1. Schematic of the fabrication process of $CoNi_2Se_4$-rGO@NF.

2.4. CHARACTERIZATIONS OF THE MATERIALS

The crystalline phase of the product was characterized through powder X-ray diffraction (PXRD) on a Philips X-Pert x-ray diffractometer with Cu Kα (1.5418 Å) radiation. The PXRD pattern was collected from 10° to 90°. A FEI Helios Nanolab 600 FIB/FESEM operating at an acceleration voltage of 10 kV and a working distance of 5.0 mm was employed to obtain SEM images of the electrode surface to study the morphology of the product. Also, energy dispersive spectroscopy (EDS) accompanied by line scan analysis was acquired from the SEM microscope. High resolution transmission electron microscopy (TEM) images and selected area electron diffraction (SAED) pattern were obtained using FEI TECNAI F20 operating at 200 kV accelerating voltage. X-ray photoelectron spectroscopy (XPS) measurements of the catalysts were performed by a Kratos Axis 165 X-ray Photoelectron Spectrometer using the monochromatic Al X-ray source. The spectra were collected after sputtering with Ar for 30 seconds which removes approximately < 1 nm from the surface.

2.5. ELECTROCHEMICAL MEASUREMENTS

The electrochemically active surface area (ECSA) of the modified electrode from double layer capacitance measurements in the non-Faradaic region was also measured and details are provided in the ESI† (Figure S1). In the non-Faradaic region, the current measured corresponded only to the charge/discharge of the electric double layer. A series of current–voltage plots were measured in the non-Faradaic region with scan rates ranging from 2.5–40 mV s^{-1}. The current at a fixed potential was plotted as a function of scan rate, and from the linear plot, the double layer capacitance, C_{dl}, was estimated. *ECSA* was calculated using the following equation (eqn (1)): [17]

$$ECSA = C_{dl} \,/\, C_s \qquad (1)$$

where C_s is the specific capacitance of the sample or the capacitance of an atomically smooth planar surface of the material per unit area under identical electrolyte conditions (C_s = 0.04 mF cm^{-2} in 0.1M NaOH was used). The *ECSA* was estimated to be 80 cm^2.

Cyclic voltammetry (CV) and chronoamperometry measurements were performed with an IviumStat potentiostat under continuous stirring in a three-electrode electrochemical setup to scan the current and voltage profiles, where $CoNi_2Se_4$–rGO@NF served as the working electrode while a platinum mesh and Ag|AgCl electrode were selected as the counter and reference electrodes, respectively. A 0.1 M NaOH aqueous solution was used as the electrolyte. The limit of detection of the analyte was calculated according to the following equation (eqn (2)):[46–48]

$$LOD = \ 3SD/N \qquad (2)$$

where SD is the standard deviation of the analyte concentration calculated from the current response of consecutive addition of glucose into the electrolyte; N is the slope of the calibration curve which indicates the sensitivity of the electrode with signal-to-noise ratio of 3.

3. RESULTS AND DISCUSSION

3.1. CHARACTERIZATION OF THE $CoNi_2Se_4$-RGO@NF SAMPLE

The catalytic films were grown directly on rGO-coated Ni foam since Ni foam is a conductive substrate with 3-dimensional porous network that facilitates electron transport between electrodeposited nanostructure and electrolyte, thus making it a desirable platform for the fabrication of biosensors. The morphology of the as-synthesized rGO@NF and electrodeposited $CoNi_2Se_4$–rGO@NF as the final product was observed by scanning electron microscopy (SEM). Figure 2a and its inset show low- and high-magnification SEM images, respectively, of pure binder-free rGO grown on Ni foam. Figure 2b and its inset and Figure 2c show the $CoNi_2Se_4$ films grown on the rGO@Ni substrate with low to high magnifications. As shown in these figures, both rGO and the nanoflake-like structures of $CoNi_2Se_4$–rGO were uniformly distributed on the Ni foam. Such a flake-like nanostructured geometry leads to a rough surface of the electrode, which can be expected to lead to enhancement of the electrode performance due to the high surface area, better surface-to-volume ratio and exposure of more electrocatalytically active sites on $CoNi_2Se_4$–rGO@NF. Moreover, the surface

composition of the $CoNi_2Se_4$ nanoflakes has been investigated through EDS spectra (Figure S2, ESI†), which verified the film composition to be $CoNi_2Se_4$ with an approximate elemental ratio of 1 : 2 : 4 for Co : Ni : Se. In addition, the elemental mapping of Co, Ni, and Se (Figure S3, ESI†) further confirmed the coexistence of Co, Ni and Se uniformly over the Ni foam in the above-mentioned relative ratio. The nanostructured morphology of the electrodeposited film was further verified by TEM imaging as has been reported in our previous article on $CoNi_2Se_4$ as an efficient OER electrocatalyst (Figure S4a, ESI†).[17] The SAED pattern shows the crystalline nature of the nanocomposite (Figure S4b, ESI†). The crystalline phase of the material was also confirmed by the powder X-ray diffraction (PXRD) method, as illustrated in Figure 2d. The diffraction peaks from the as-synthesized $CoNi_2Se_4$–rGO@NF film matched with the standard diffraction pattern of $CoNi_2Se_4$ (PDF file card no. 04-006-5239) confirming the pure crystalline nature of the electrodeposited film. Raman spectroscopy was also performed to characterize the rGO present in the composite. As shown in Figure 2e, the as-synthesized rGO shows two prominent peaks at 1331 cm^{-1} and 1573 cm^{-1} corresponding to the structural defects and disorder in the graphene network (D band) and the C–C bond stretching frequency (G band), respectively. Generally, the intensity ratio of the D- and G-bands (I_D/I_G) is used to estimate the degree of disorder and the average size of the sp^2 domains. The value of $I_D : I_G$ was calculated to be 0.94. Furthermore, XPS was employed to obtain detailed information about the chemical composition and oxidation states of the corresponding elements in the as-deposited $CoNi_2Se_4$ nanoflakes. For XPS studies,

electrodeposited films on Au-glass substrates were used to avoid the huge Ni signal coming from Ni foam substrate. The XPS studies have also been reported in our previous study.[17] The XPS peaks were calibrated with respect to the C1s signal (284.5 eV) as a reference binding energy. Figure S5, ESI† (adopted from our previous publication[17]) shows all of the XPS peaks for Ni, Co, and Se. The oxidation states of Co and Ni were investigated from the deconvoluted XPS spectra. It was confirmed, using the Gaussian fitting method, that Ni 2p and Co 2p are present in mixed 2+ and 3+ valence states, which conceivably plays a key role in their electrocatalytic activity towards glucose oxidation.[49] As shown in Figure S5a, ESI,† the peaks located at 777.6 eV and 794.2 eV can be attributed to Co3+ and those at 780.2 eV and 795.5 eV are assigned to Co^{2+} with its shake-up satellite peaks at 785.2 eV and 800.5 eV.[50, 51] The peaks centered at 854.3 eV and 871.8 eV correspond to Ni^{2+}, while those at 856.1 and 873.3 eV are in agreement with Ni^{3+} (Figure S5b, ESI†).[52, 53] Finally, the peaks at 54.0 eV and 54.9 eV shown in Figure S5(C) (ESI†) correspond to Se $3d_{5/2}$ and Se $3d_{3/2}$, respectively, and match with the binding energies repeatedly reported in the transition metal selenides.[54] Based on the XPS results, it was concluded that $CoNi_2Se_4$ has a vacancy-ordered spinel structure, where Co is primarily present as divalent ions occupying the fully-filled layers while Ni is present primarily as Ni^{3+} in the half-filled vacancy-ordered layer. The presence of mixed valency also indicates that there is significant scrambling of Co^{3+} and Ni^{2+} in the vacancy-ordered and fully occupied layers, respectively.

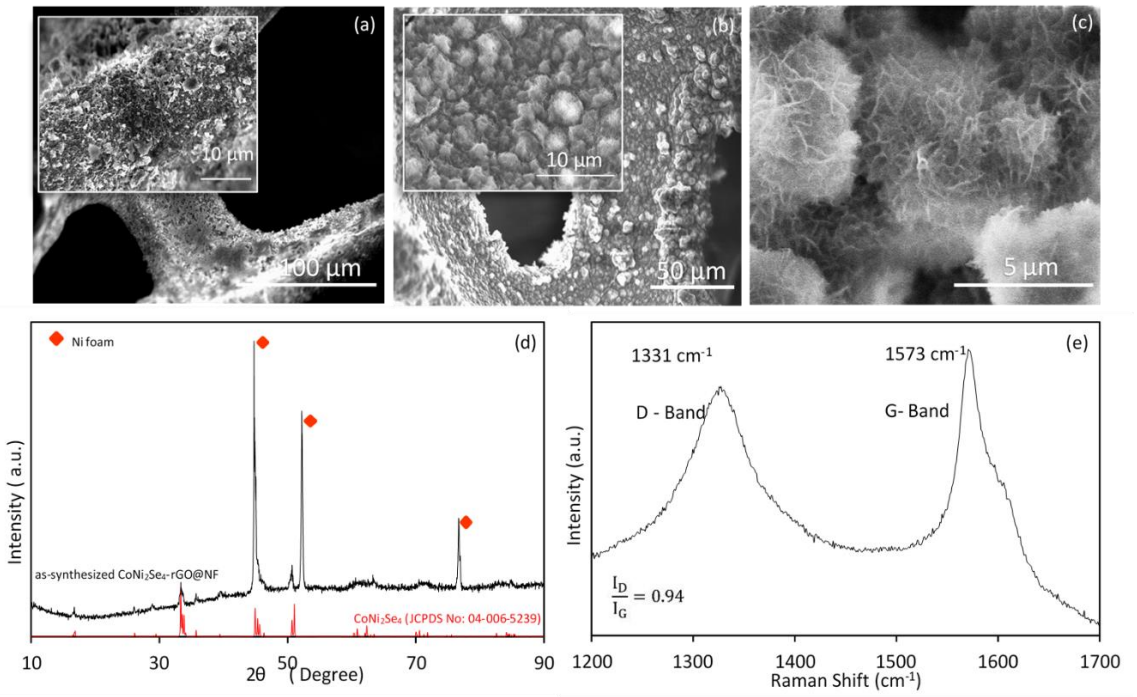

Figure 2. Characterization techniques of $CoNi_2Se_4$-rGO@NF. (a) SEM image of reduced graphene oxide on Ni foam at low magnification (the inset shows a higher magnification SEM image of rGO@NF), (b) SEM image of $CoNi_2Se_4$–rGO on Ni foam at low magnification (the inset shows a higher magnification SEM image) and (c) SEM image of $CoNi_2Se_4$–rGO@NF showing a nanoflake-like geometry with a rough electrode surface. (d) The XRD pattern of $CoNi_2Se_4$–rGO@NF. (e) Raman spectrum of the reduced graphene oxide.

3.2. ELECTROCATALYTIC ACTIVITY OF THE $CoNi_2Se_4$@NF ELECTRODE TOWARDS GLUCOSE DETECTION

Cyclic voltammetry (CV) was used to characterize the electrocatalytic activity of different catalyst-coated composite electrodes towards glucose oxidation in an alkaline medium. Figure 3a shows the current response of bare $CoNi_2Se_4$ on Ni foam measured in 0.1 M NaOH at different scan rates by scanning the applied potential. It is observed that the anodic and cathodic peak currents clearly increase with increasing scan rate, suggesting a diffusion-controlled reaction mechanism at the surface of the electrode.

The inset in Figure 3a shows the linear relationship between the peak current and the square root of the scan rate, which further verifies the diffusion-controlled process occurring at the electrode. Upon addition of 1.0, 2.0, 3.0, 4.0, and 5.0 mM glucose into the 0.1 M NaOH electrolyte, the $CoNi_2Se_4$@NF electrode exhibited a substantial increase in anodic current density as shown in Figure 3b, indicating increase of the oxidation current due to glucose oxidation.

To clearly identify the optimal potential for glucose oxidation, different applied potentials in the range of 0.3–0.4 V vs. Ag|AgCl were investigated with successive addition of 0.1 mM glucose, as shown in Figure 3c. It is obvious that the current response on glucose addition increases sharply when the applied potential increases from 0.3 V to 0.35 V and then decreases with the increase of the applied potential from 0.35 to 0.40 V. Therefore, the best working potential for glucose oxidation was selected to be 0.35 V for the remainder of this study. As shown in Figure 3d, upon successive addition of varying concentrations of glucose, significant and fast current responses were observed for the $CoNi_2Se_4$@NF electrode with 95% of the steady-state current reached within 6 seconds (Figure 3f). The step size of the current density increase depends on the concentration of glucose and typically rises with increasing concentration (Figure 3d).

The current density was plotted as a function of added glucose concentration as shown in Figure 3e, which served as the calibration curve for the $CoNi_2Se_4$@NF electrode. Linear fitting of the calibration plot in the concentration range from 0.001 mM to 4.0 mM ($R^2 = 0.9974$) yielded the sensitivity of glucose detection, which was estimated to be as high as 9.8766 mA mM^{-1} cm^{-2} (Figure 3e). In glucose sensing devices, the efficiency is measured by the current response as well as the working potential for the

device. Since most of these chalcogenides have limited electrical conductivity, in order to obtain better electrocatalytic performance, rGO was introduced to the $CoNi_2Se_4$ system.

It is expected that the presence of rGO in the catalytic matrix will elevate the sensitivity of the electrode with a faster response time and higher current density due to the enhanced conductivity, better electron transfer, and increased specific surface area of the reduced graphene oxide.[55]

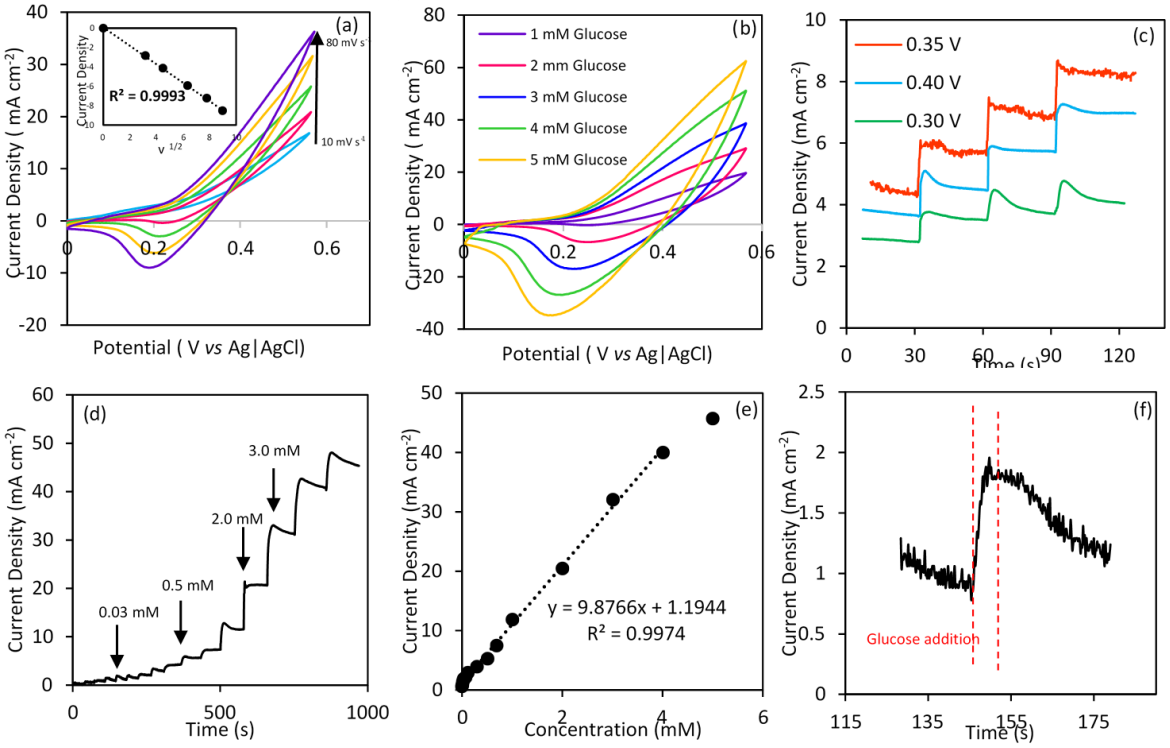

Figure 3. Electrochemical performance of $CoNi_2Se_4$@NF. Cyclic voltammograms of the $CoNi_2Se_4$ on Ni foam electrode (a) in the absence of glucose at different scan rates: 10, 20, 40, 60, 80, and 100 mV s^{-1} (the inset is the relationship between the peak current and the square root of the scan rate), and (b) at different glucose concentrations with a scan rate of 10 mV s^{-1}. (c) Amperometric current responses of $CoNi_2Se_4$@NF at different working potentials with successive addition of 0.1 mM glucose. (d) Amperometric response of $CoNi_2Se_4$@NF upon the successive addition of glucose. (e) The calibration curve for the current response to glucose concentration. (f) Plot showing the response time to reach the steady-state current.

3.3. ELECTROCATALYTIC ACTIVITY OF THE $CoNi_2Se_4$–RGO@NF ELECTRODE TOWARDS GLUCOSE SENSING AND DETECTION

The $CoNi_2Se_4$–rGO@NF composite electrode was prepared by a similar electrodeposition technique to that mentioned above. The electrocatalytic performance of the composite $CoNi_2Se_4$–rGO@NF electrode, shown in Figure 4, was investigated by electrochemical measurements such as chronoamperometry and CV in the absence and presence of glucose in 0.1 M NaOH solution at the scan rate of 10 mV s^{-1}. The CV plots presented in Figure 4a show that $CoNi_2Se_4$–rGO@NF does not exhibit a clear anodic peak in the potential range between 0.1 V and 0.5 V. However, the anodic current rises and shifts linearly with the increase of the scan rate. The linear relationship between the peak current and the square root of the scan rate as shown in the inset of Figure 4a indicates a diffusion-controlled electrochemical process occurring on the electrode surface. The cathodic peak shows a negative movement with the increase of the scan rate, most probably due to the fortified electric polarization resulting from the oxidation–reduction procedure.[56]

The electrochemical properties of $CoNi_2Se_4$–rGO@NF towards glucose oxidation are shown in Figure 4b. Upon injection of glucose into the electrolyte, a clear anodic peak can be observed at +0.35 V vs. Ag|AgCl in the CV curve, and the enhancement of the oxidation peak becomes more noticeable with an increase in glucose concentration. By comparing the electrocatalytic activities of the $CoNi_2Se_4$@NF and $CoNi_2Se_4$–rGO@NF electrodes, it can be observed that the addition of rGO led to higher oxidation current densities and less noise in the chronoamperometry plots, leading to a more distinctive peak for glucose oxidation. This enhancement can be related to the increased surface area of the rGO– $CoNi_2Se_4$ composite, as well as better conductivity of

the matrix leading to enhanced electron transfer rate. However, rGO by itself on Ni foam did not show significant electrocatalytic activity towards glucose oxidation as shown in Figure S6, ESI,† highlighting the fact that the actual catalytically active centers are in the CoNi2Se4 component (specifically Co and Ni sites). In order to achieve a high current response for the detection of glucose, choosing an optimized working potential in the presence of glucose is critical. An overly-high potential can lead to an unwanted oxygen evolution reaction resulting in lesser accessible active surface area and large background current. At the same time, detection of glucose in a wide range of concentrations at the optimal applied potential is also critical for practical application of the sensor. In this regard, the amperometric response upon consecutive addition of 0.01 mM glucose to 0.1 M NaOH was explored through a typical I–t technique and illustrated in Figure 4c. As shown in the figure, the maximum current response was observed at 0.35 V vs. Ag|AgCl, which matches well with the anodic oxidation peak, enabling excellent sensing performance for glucose oxidation. Therefore, this potential was selected as the working potential for the rest of the electrochemical experiments. The amperometric response data of the $CoNi_2Se_4$–rGO@NF electrode acquired at 0.35 V vs. Ag|AgCl in 0.1 M NaOH electrolyte under vigorous stirring of the NaOH solution at 1000 rpm are provided in Figure 4d, showing a steep current rise with every successive injection of the glucose analyte with varying concentrations. As explained above, the sensitivity and linear range of glucose detection can be found by plotting the peak current density against the glucose concentration, as shown in Figure 4e. In the concentration range between 1.0 mM and 4.0 mM, the sensor response is linear with a sensitivity of 18.890 mA mM^{-1} cm^{-2} and a correlation coefficient (R^2) of 0.9998 obtained from linear fitting of the plot shown in

Figure 4e. To the best of our knowledge, this is one of the highest sensitivities that has been reported at a low operating voltage for non-enzymatic glucose sensors (Table 1). The relatively small linear range of glucose sensing could be due to the limited exposure of the active surface sites of the electrode to the reaction intermediates at high concentrations of glucose. The limit of detection (LOD) for $CoNi_2Se_4$–rGO@NF with a signal-to noise ratio of 3 (S/N = 3) for non-enzymatic glucose sensing was found to be as low as 0.65 mM using eqn (2).

$CoNi_2Se_4$–rGO@NF can reach 95% of its steady-state current signal in less than 4 seconds, as shown in Figure 4f, which indicates a good electrocatalytic performance of the $CoNi_2Se_4$–rGO@NF electrode for non-enzymatic glucose oxidation. It should be noted here that the sensitivity of this $CoNi_2Se_4$– rGO based non-enzymatic sensor is superior to that of the average sensors. The causes of this high sensitivity are manifold: (i) the composition of the catalytic site (Co and Ni in a selenide coordination); (ii) the presence of Ni3+ in the as-prepared catalyst; (iii) the presence of rGO and a highly porous morphology of the electrode; and (iv) the direct growth of the catalytic composite on the electrode yielding a binder-free film. The mechanism of glucose oxidation to gluconolactone is believed to be initiated by the attachment of a hydroxyl group (–OH) to the catalytically active transition metal sites (Ni and Co in this case), which undergo local oxidation. The charge transfer occurring at the catalyst-electrolyte interface can further lead to oxidation of glucose.[57] Since the catalytic site undergoes local oxidation, the redox potential for the transition metal sites can have a large influence on the catalytic activity for glucose oxidation, especially the applied potential value. Recently we have probed the influence of ligand composition on the electrocatalytic activity in transition

metal-based catalysts in the context of the OER. From these studies, it has been observed that increasing the covalency around the transition metal sites by decreasing the ligand electronegativity leads to lowering of the transition metal site oxidation potential. Hence, the selenide coordination of the transition metals lowers the oxidation potential for these catalytically active sites.[58, 59] Therefore, the onset of glucose oxidation catalytic activity can occur at much lower potential compared to other sensors, which are mostly based on the elemental metal or its oxide. Additionally, the coexistence of Ni and Co in these catalysts can influence the local site oxidation by modulating the electron densities around the active sites.[60] Secondly the chalcogenide coordination also increases the lattice covalency leading to the selenides being more metallic with higher conductivity compared to the oxides. Hence, charge transfer within the catalyst grains is greatly enhanced. The inter-grain charge transfer is also improved significantly by the addition of rGO, which has a synergistic effect, as well as the porous 3D network of the Ni foam leading to high oxidation current density. The presence of Ni^{3+} in the as synthesized product is also believed to significantly improve the catalytic activity since Ni^{3+} is the actual catalytically active site for these electrochemical processes including conversion of glucose to gluconolactone.[61,62] In other Ni-based electrocatalysts, Ni is present mostly as Ni^{2+}, which is electrochemically oxidized in situ to Ni^{3+} (a step commonly known as catalyst activation). The combined effect of these factors results in onset of the catalytic activity at very low applied potentials along with achieving high current density, which is reflected in the sensitivity of the sensor.

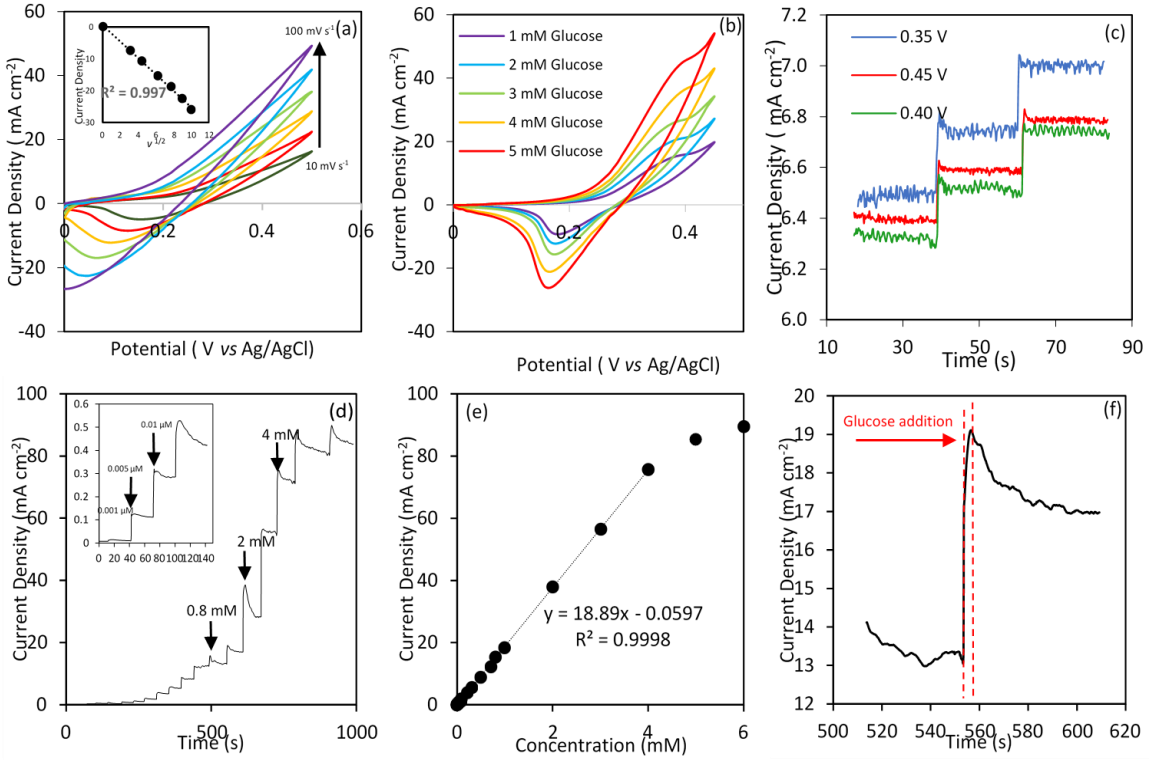

Figure 4. Electrochemical performance of $CoNi_2Se_4$–rGO@NF. Cyclic voltammograms of the $CoNi_2Se_4$–rGO@NF electrode (a) in the absence of glucose at different scan rates: 10, 20, 40, 60, 80, and 100 mV s^{-1}, and (b) at different glucose concentrations with a scan rate of 10 mV s^{-1}. (c) Amperometric current responses of $CoNi_2Se_4$–rGO@NF at different working potentials with successive addition of 0.01 mM glucose. (d) Amperometric response of $CoNi_2Se_4$–rGO@NF upon the successive addition of glucose; (inset) current response upon addition of a low concentration of glucose. (e) The calibration curve for the current response to glucose concentration. (f) Plot of the response time to reach the steady-state current.

3.4. SELECTIVITY AND STABILITY STUDIES OF $CoNi_2Se_4$-RGO@NF

The two main challenging aspects of non-enzymatic glucose sensing are the effect of possible physiological interference from interferents present in blood serum and the stability of the electrode for long-term use. The relatively high working potential employed to oxidize glucose in conventional sensors can possibly oxidize other compounds present in blood, therefore resulting in an overestimated amperometric

current value, which may have life threatening consequences such as hyperglycemia and hypoglycemia causing coma or even death. Several compounds found in human blood can interfere with glucose detection as they are strong reducing agents similar to glucose, and hence can easily be oxidized at the selected potential. Such common interfering species include ascorbic acid (AA), lactose (LA), fructose (FR), dopamine (DA), NaCl, KCl and urea. Thus, an experiment was designed to investigate the selectivity of the $CoNi_2Se_4$–rGO@NF glucose sensing device towards glucose oxidation and the results are shown in Figure 5a. The selectivity study was carried out at an applied potential of 0.35 V vs. Ag|AgCl under the same experimental conditions as mentioned above, where glucose and the interferents were added to the same electrolyte. The $CoNi_2Se_4$–rGO@NF electrode exhibits a high current response upon the addition of 1.0 mM glucose. However, the addition of 0.1 mM of the interfering compounds did not yield any detectable current response, as shown in Figure 5a. This confirmed that the present $CoNi_2Se_4$–rGO@NF electrode is selective towards glucose oxidation and can avoid interference from AA, FR, LA, DA, NaCl, KCl and urea. The selectivity of this sensor was also evaluated in the presence of a high concentration of DA and AA by measuring the CV plots in the presence of 1 mM DA, 1 mM AA, or 1 mM glucose solutions at the same potential (0.35 V) as shown in Figure S7, ESI.† It was observed that at 0.35 V, glucose was oxidized readily producing nearly double the current density compared to that of DA and AA. The CV plots of DA and AA, on the other hand, demonstrated that the onset of electro-oxidation for these compounds was at a much higher potential. This further confirms the high selectivity of $CoNi_2Se_4$–rGO@NF towards glucose oxidation at a low applied potential even in the presence of high concentrations of interferents. The

peak current density in CV is also an illustration of the sensitivity of the device and represents the saturation current density that can be achieved in the presence of 1 mM glucose in the solution. The reproducibility and consistency of the results for $CoNi_2Se_4$–rGO@NF towards glucose sensing were investigated by chronoamperometry studies for four different electrodes prepared in three different batches of freshly prepared $CoNi_2Se_4$–rGO samples, and one previously tested electrode stored at room temperature for over three months under ambient conditions. The glucose oxidation with these electrodes was measured in 0.1 M NaOH by subsequent addition of 0.01 mM glucose at regular intervals and recording the current responses after each injection. The results are shown in Figure 5b. It can be observed that addition of a similar concentration of glucose resulted in an almost equal jump in current density and almost the same response time, confirming good repeatability of the $CoNi_2Se_4$–rGO@NF electrode. Interestingly, even after three months of storage under ambient conditions, the sensor did not show any significant loss in amperometric response, confirming the excellent reliability of this electrode.

The long-term stability of the electrode was also examined by a chronoamperometry test as shown in Figure 5c, where 0.1 mM glucose was added to 0.1 M NaOH for an extended period of time in an electrolyte containing 1.0 mM glucose. As the glucose in the electrolyte got oxidized, the current density gradually decreased; however, upon addition of fresh glucose into the electrolyte after about 80000 seconds, it showed an almost identical change in current density to the pristine electrode. This amperometric test underlined the stability of this electrode and verified that there is no surface poisoning and deterioration in efficiency following long-term application. The re-

usability and reproducibility of this non-enzymatic glucose sensor are a significant advantage over enzymatic sensors, which have limited reusability due to enzyme denaturation.

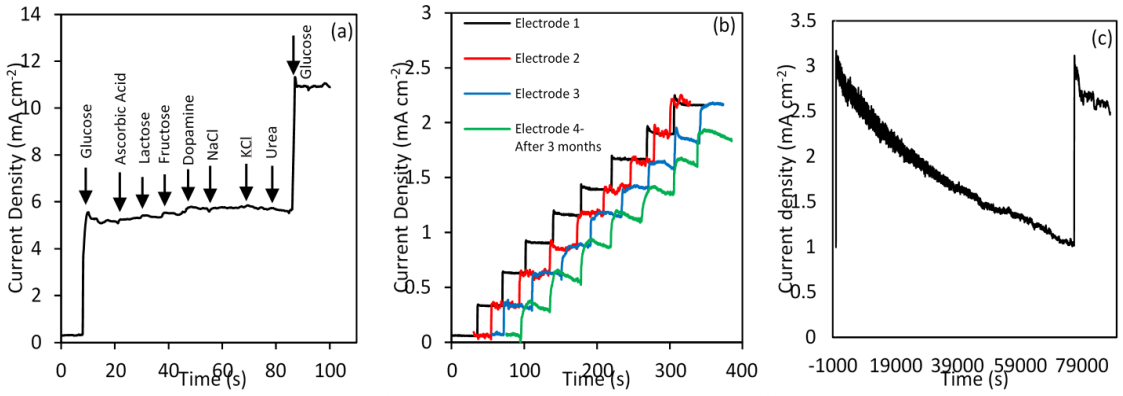

Figure 5. Selectivity and Stability of $CoNi_2Se_4$-rGO@NF. (a) The amperometric response of the $CoNi_2Se_4$–rGO on NF electrode to the successive addition of 1.0 mM glucose, and 0.1 mM ascorbic acid, lactose, fructose, dopamine, NaCl, KCl and urea. (b) The amperometric response of different batches of freshly prepared electrodes (electrodes 1, 2, and 3, and a previously used electrode stored for 3 months under ambient conditions (electrode 4)) to 0.01 mM successive additions of glucose in 0.1 M NaOH at a working potential of 0.35 V vs. Ag|AgCl. (c) Chronoamperometric long-term stability check at 0.35 V.

A comparison of the $CoNi_2Se_4$–rGO@NF glucose sensing efficiency with that of several previously reported enzymatic and non-enzymatic glucose biosensors is provided in Table 1. From this table it can be concluded that $CoNi_2Se_4$–rGO@NF indeed shows promising glucose sensing activities at a low operating voltage, with a low limit of detection, high sensitivity and fast response time along with a wide linear range. These characteristics collectively are indicative of an excellent performance of $CoNi_2Se_4$–rGO@NF as a non-enzymatic glucose sensor.

Table 1. Comparison of reported non-enzymatic glucose sensors with $CoNi_2Se_4$-rGO@NF.

Electrode	Detection Potential	Sensitivity ($\mu A\ mM^{-1}\ cm^{-2}$)	LOD (μM)	Linear range	Ref.
$CoNi_2Se_4$-rGO@NF	0.35	18890	0.651	l μM−4.0 mM	This work
solid/nanoporous Au/Co_3O_4 (In 0.5 M KOH)	0.26	12500	0.005	1 mM to 10 mM	63
CuO nanowires	0.33	0.49	0.05	0.4 μM−2.0 mM	64
NiO-GR/GCE	0.35	15.94	5.0	0.02–4.5 mM	65
Co_3O_4 UNS-$Ni(OH)_2$/GCE	0.35	1.089	1.08	5 – 40 μM	66
Electrodeposited $NiCo_2O_4$	0.4	6.69	0.38	5 – 65 μM	67
CuO NWA/CF	0.5	32330	0.02	0.10 mM–0.50 mM	68
NiO/C microspheres	0.5	30190	2.0	2 lM–1.279 mM	69
Cu_2Se SPs/CF	0.5	18660	0.25	0. 25 μM –0.237 mM	70
3D Co_3O_4/Ni	0.5	13855	1.0	0.04−3.6 mM	71
Ni^{3+}-rich surface electrode	0.5	11361; 3579.9	0.9	0.001–1, 2–4 mM	72
3D porous Ni networks	0.5	2900	0.07	5 μM−4 mM	73
$NiCo_2O_4$/3DGF	0.5	2524	0.38	Up to 80 mM	74
Ni–Co NSs/rGO	0.5	1773.61	3.79	10 μM – 2.65 mM	75
$Ni_{0.31}Co_{0.69}S_2$/rGO	0.5	1753; 954.7	0.078	1 mM to 5 mM; 5–16 mM	76
CuO NPs	0.5	1430	5.0	0.04–6.0 mM	77
$NiCoO_2$@CNT	0.5	1424	1.14	0.01–1.55 mM	78
NiO/GNS	0.5	666.71	5.0	5μM–4.2mM	79
s-NiO/GD	0.5	36.13	0.9	Up to 10 mM	80
NiNPs/PEDOT/RGO	0.5	36.15	0.8	0.001–5.1	81
$NiSe_2$-NS/GCE	0.5	5.6	0.023	0.099–1252lM	82
$NiCo_2S_4$	0.5	5.14	1.20	1−664 μM	83
NiONP/Gr	0.53	2401	0.53	0.001–15 mM	84
$Co(OH)_2$/GCE	0.53	925.21	0.93	Up to 0.13 mM	85
CuNi/C	0.54	17120	0.07	0.2 μM–2.72 mM	86
Ni_3S_2/MWCNT	0.54	3345	1.0	30–500 μM	87
Ni_3S_2/Ni foam	0.55	16460	0.82	0.0005–3 mM	88
3D Ni_3S_2/Ni foam	0.55	6148	1.2	0.005–3.0 mM	89
$CuCo_2O_4$ NWAs/CC	0.55	3930	0.50	0.001–0.93 mM	90
$NiCo_2O_4$/rGO	0.55	2082.57	0.70	0.04–1.28 mM	91
Co_3O_4 HND/GCE	0.55	708.4	0.58	2.0–6060 μM	92
$MnCo_2O_4$ nanofibers	0.55	679.5	0.01	0.05 − 800 μM	93
Co_3O_4/$NiCo_2O_4$ DSNCs@G	0.55	304	0.384	0.01–3.52 mM	94
Electrospun Co_3O_4 nanofibers	0.59	36.25	0.97	Up to 2.04 mM	95
CuO/rGO/CNT	0.6	9278	1.0	0.01−1 mM	96
Ni $(OH)_2$ nanostructure rGO	0.6	11400	15.0	0.01–30 mM	97
CoP NA/TM	0.6	5168.6	0.1	0.0005–1.50 mM	98
CuO/NiO/PANI/GCE	0.6	3402	2	20 μM –2.5 mM	99
NA/NiONF-rGO/GCE	0.6	1100	0.77	0.002–0.60 mM	100
Ni–MWNTs	0.6	67.19	0.89	3.2 μM–17.5 mM	101
Nano-SiO_2 - Pt (Enzymatic)	0.6	3.85	1.5	0.27−4.08 mM	102
3-D $Ni_3(VO_4)_2$ Nanosheet	0.62	19830	0.57	2.5–150 μM	103
CuO-ZnO NRs/FTO	0.62	2961.7	0.40	Up to 8.45 mM	104
CuS/RGO/CuS/Cu	0.65	22670	0.50	0.001–0.655 mM	105
Ni/Al-LDH on Ti foil	0.70	24.45	5.0	0.005–10.0 mM	106
TiO_2 NTs-Ni $(OH)_2$ NPs	0.70	120	5.0	0.02–1.70 mM	107

Table 2. Determination of glucose in human blood.

Sample	Measured Concentration (mM)		Deviation
	Commercial Glucometer	The developed electrode (RSD%)	
1	5.66 (102 mg/dL)	5.56 (4.12 %)	1.76%
2	5.38 (97 mg/dL)	5.27 (4.36 %)	2.04%

3.5. APPLICATION OF THE CoNi2Se4-RGO@NF ELECTRODE TOWARDS DETECTION OF HUMAN BLOOD GLUCOSE

The practical application of the $CoNi_2Se_4$–rGO@NF sensor was verified by detecting the glucose concentration in a few drops of blood obtained from participating volunteers and the results were compared with those measured using a store-bought glucometer kit (ReliOn containing typical glucose sensing strips and the meter). Details of this measurement along with the relevant plots are provided in the ESI. † Specifically, 100 mL of 1 mM glucose solution was added two times to 0.05 M NaOH to stabilize the $CoNi_2Se_4$–rGO@NF electrode response. Then, the blood sample was directly injected into the electrolytic system followed by two more additions of equal volumes of 1 mM glucose. The current response for each of these additions (1 mM glucose solution) was plotted as a function of glucose concentration and the glucose amount in the blood sample was estimated from the linear fit of the plot (after subtracting the background glucose concentrations). A typical plot for the blood glucose experiment is shown in Figure S8, ESI, † while Table 2 lists the glucose concentration as detected by a standard glucometer and the $CoNi_2Se_4$–rGO-based sensor. As can be seen from the table, the estimated concentration using the sensor was in good agreement with the value measured by the commercial glucometer (ReliOn), indicating that the $CoNi_2Se_4$–rGO@NF electrode can be utilized for practical glucose detection in blood samples. Three

measurements were performed for each sample and an acceptable relative standard deviation (RSD) of less than 5% was achieved for both samples, suggesting the reliability of this electrode for glucose sensing.

4. CONCLUSIONS

We have demonstrated a simple approach for producing $CoNi_2Se_4$–rGO on Ni Foam by a facile electrodeposition method producing a catalyst-coated and binder-free composite electrode. The as-deposited $CoNi_2Se_4$exhibited a nanoflake-like geometry with a uniform and highly 3-dimensional network of the catalytic film. Moreover, the multiple active sites in $CoNi_2Se_4$ combined with the enhanced conductivity of the reduced graphene oxide improved the electrocatalytic performance of this electrode towards glucose oxidation. The ultrahigh sensitivity (18.89 mA mM^{-1} cm^{-2}) at a low applied potential of only 0.35 V vs. Ag|AgCl, wide linear range (1 mM–4.0 mM), low detection limit (0.65 mM), short response time of less than 4 seconds with impressive selectivity, repeatability, and stability make this $CoNi_2Se_4$/rGO–NF a promising electrode to serve as a non-enzymatic glucose sensor. Moreover, the reliability of this electrochemical glucose sensor was tested by estimating the blood glucose level in two independent blood samples, and the values showed excellent similarity with the glucose level detected by a commercially available glucometer, indicating that these biosensors indeed have great potential for practical use.

ACKNOWLEDGEMENTS

This work was partially supported through funds from the National Science Foundation (DMR 1710313). The authors would like to thank Dr Sergii Chertopalov for help with Raman spectroscopy.

REFERENCES

1. H. Rao, Z. Zhang, H. Ge, X. Liu, P. Zou, X. Wang and Y. Wang, *New J. Chem.*, 2017,41, 3667-3676.

2. K.-L. Wu, Y.-M. Cai, B.-B. Jiang, W.-C. Cheong, X.-W. Wei, W. Wang, and N. Yu, *RSC Adv.*, 2017,7, 21128-21135.

3. N. Hui and J. Wang, *Journal of Electroanalytical Chemistry*,2017,798, 9–16.

4. B. Xue, K. Li, L. Feng, J. Lu and L. Zhang, *Electrochimica Acta*, 2017, 239, 36–44.

5. S. Ci, T. Huang, Z. Wen, S. Cui, S. Mao, D.A. Steeber and J. Chen, *Biosens. Bioelectron.*, 2014, 54, 251.

6. A. Sun, J. Zheng and Q. Sheng, *Electrochim. Acta*, 2012, 65, 64.

7. A. Heller, B. Feldman, *Chem. Rev.*, 2008, 108, 2482–2505.

8. H. Susanto, A.M. Samsudin, N. Rokhati, I.N. Widiasa, *Enzyme Microb. Technol.*, 2013, 52, 386–392.

9. K. Kumar Naik, A. Gangan, B. Chakraborty, S. K. Nayak, and C. S. Rout, *ACS Appl. Mater. Interfaces*, 2017, 9, 23894−23903

10. G. Dryhurst, K. Niki, *Springer Science & Business Media*, 2012.

11. F. P. Van der Zee, F. J. Cervantes, *Biotechnol. Adv.*, 2009, 27, 256−277.

12. X. Chia, A. Y. S. Eng, A. Ambrosi, S. M. Tan and M. Pumera, *Chem. Rev.*, 2015, 115, 11941–11966.

13. J.L. Qi, X. Wang, J.H. Lin, F. Zhang, J.C. Feng and W.D. Fei, *J. Mater. Chem.*, 2015, A 3, 12396–12403.

14. W. Huanga, Y. Caoa, Y. Chena, J. Peng, X. Lai and J. Tu, *Applied Surface Science*, 2017, 396, 804–811.

15. V. Neburchilov, H. Wang, J. J. Martin and Q. Wei, *J. Power Sources*, 2010, 195, 1271–1291.

16. P. Karthick Kannan and C. S. Rout, *Chem. Eur. J.*, 2015, 21, 9355 – 9359.

17. B. G. Amin, A. T. Swesi, J. Masud and M. Nath, *Chem. Commun.*, 2017, 53, 5412–5415.

18. A. Sivanantham, P. Ganesan, and S. Shanmugam, *Adv. Funct. Mater.*, 2016, 26, 4661–4672.

19. D. Liu, Q. Lu, Y. Luo, X. Sun, and A. M. Asiri, *Nanoscale*, 2015, 7, 15122–15126.

20. Q. Liu, J. Jin, and J. Zhang, *ACS Appl. Mater. Interfaces*, 2013, 5, 5002−5008.

21. S. Yun Khoo, J. Miao, H. Yang, Z. B. He, K. C. Leong, B. Liu, and T. T. Yang Tan, *Adv. Mater. Interfaces*, 2015, 2, 1500384.

22. N. Huang, S. Zhang, H. Huang, J. Liu, Y. Sun, P. Sun, C. B., L. Zheng, X. Sun, X. Zhao, *Electrochimica Acta*,2016, 192, 521–528.

23. J. Lin, S. Chou, *Electrochemistry Communications*, 2013, 37, 11–14.

24. R. Zou, Z. Zhang, M. Fung Yuen, M. Sun, J. Hu, C. Lee, and W. Zhang, *NPG Asia Materials*, 2015, 7, 8.

25. Q. Wang, L. Jiao, Y. Han, H. Du, W. Peng, Q. Huan, D. Song, Y. Si, Y. Wang, and H. Yuan, *J. Phys. Chem. C*, 2011, 115, 8300–8304.

26. L. Shen, J. Wang, G. Xu, H. Li, H. Dou, and X. Zhang, *Adv. Energy Mater.*, 2015, 5, 1400977.

27. J. Pu, T. Wang, H. Wang, Y. Tong, C. Lu, W. Kong, and Z. Wang, *ChemPlusChem*, 2014, 79, 577 – 583.

28. J. Xiao, L. Wan, S. Yang, F. Xiao, and S. Wang, *Nano Lett.*, 2014, 14, 831−838.

29. H. Wan, J. Jiang, J. Yu, Kui Xu, Ling Miao, Li Zhang, Haichao Chen, and Yunjun Ruan, *CrystEngComm*, 2013, 15, 7649-7651.

30. Shengjie Peng, Linlin Li, C. Li, H. Ta, R. Caia, H. Yu, S. Mhaisalkar, M. Srinivasan, S. Ramakrishna, and Q. Yan, *Chem. Commun.*, 2013, 49, 10178-10180.

31. A. T. Swesi, J. Masud, W. P. R. Liyanage, S. Umapathi, E. Bohannan, J. Medvedeva, and M. Nath, *Scientific Reports*, 2017, 7, 2401.

32. P. K. Kannan, B. Dinesh, C. Y. An, and C.-H. Chung, *Chemistry Select.*, 2017, 2, 1967 – 1973.

33. L. Zhang, Y. Ding, R. Li, C. Ye, G. Zhao, and Y. Wang, *J. Mater. Chem. B*, 2017, 5, 5549 – 5555.

34. G. F. Wang, X. P. He, L. L. Wang, A. X. Gu, Y. Huang, B. Fang, B. Y. Geng and X. J. Zhang, *Microchim. Acta*, 2013, 180, 161–186.

35. K. E. Toghill and R. G. Compton, *Int. J. Electrochem. Sci.*, 2010, 5, 1246–1301.

36. P. K. Kannan, C. S. Rout, *Chem. Eur.J.*, 2015, 21,9355 –9359.

37. K. E. Toghill, and R.G. Compton, *Int. J. Electrochem. Sci.*, 2010, 5, 1246-1301.

38. J. L. Gautier, E. Rios, M. Gracia, J. F. Marco and J. R. Gancedo, *Thin Solid Films*, 1997, 311, 51–57.

39. Y. Chen, Y. Li, D. Sun, D. Tian, J. Zhang and J. J. Zhu, *J. Mater. Chem.*, 2011, 21, 7604.

40. J. J. Gooding, *Electrochim. Acta*, 2005, 50, 3049.

41. L. Wu, L. Feng, J. Ren and X. Qu, *Biosens. Bioelectron.*, 2012, 34, 57.

42. D. Chen, L. Tang and J. Li, *Chem. Soc. Rev.*, 2010, 39, 3157.

43. D. Chen, H. Feng and J. Li, *Chem. Rev.*, 2012, 112, 6027.

44. S. Bong, Y. R. Kim, I. Kim, S. Woo, S. Uhm, J. Lee and H. Kim, *Electrochem. Commun.*, 2010, 12, 129.

45. D. C. Marcano, D. V. Kosynkin, J. M. Berlin, A. Sinitskii, Z. Sun, A. Slesarev, L. B. Alemany, W. Lu, and J. M. Tour, *ACS Nano*, 2010, *4* (8), 4806–4814.

46. G. Li, H. Huo and C. Xu, *J. Mater. Chem. A*, 2015, 3, 4922.

47. J. Liu, W. Lv, W. Wei, C. Zhang, Z. Li, B. Li, F. Kang and Q.-H. Yang, *J. Mater. Chem. A*, 2014, 2, 3031–3037.

48. B. Zhan, C. Liu, H. Chen, H. Shi, L. Wang, P. Chen, W. Huang and X. Dong, *Nanoscale*, 2014, 6, 7424–7429.

49. M. Gao, Y. Xu, J. Jiang, Y. Zheng and S. Yu, *J. Am. Chem. Soc.*, 2012, 134, 2930.

50. C. Jin, F. Lu, X. Cao, Z. Yang and R. Yang, *J. Mater. Chem. A*, 2013, 1, 12170.

51. T. Z. Su, Q. Z. Xu, G. F. Chen, H. Cheng, N. Li and Z. Q. Liu, *Electrochim. Acta*, 2015, 174, 1216.

52. H. Shi and G. Zhao, *J. Phys. Chem. C*, 2014, 118, 25939.

53. E. Umeshbabu, G. Rajeshkhanna, P. Justin and G. Ranga Rao, *RSC Adv.*, 2015, 5, 66657.

54. A. B. Mandale, S. Badrinarayanan, S. K. Date and A. P. B. Sinha, J. *Electron Spectrosc. Relat. Phenom.*, 1984, 33, 61.

55. X.-C. Dong, H. Xu, X.-W. Wang, Y.-X. Huang, M.-B. Chan-Park, H. Zhang, L.-H. Wang, W. Huang, and P. Chen, *ACS Nano*, 2012, 6, 3206−3213.

56. L. Zhang, Y. Ding, R. Li, C. Ye, G. Zhao, and Y. Wang, *J. Mater. Chem. B*, 2017, 5, 5549.

57. K. Tian, M. Prestgard, A. Tiwari, Materials Science and Engineering C, 2014, 41, 100–118.

58. U. De Silva, J. Masud, N. Zhang, Y. Hong, W. P. R. Liyanage, M. Asle Zaeem, and M. Nath, *J. Mater. Chem. A*, 2018, 6, 7608-7622.

59. S. Umapathi, J. Masud, A. T. Swesi, M. Nath, *Adv. Sustainable Syst.*, 2017, 1, 1700086.

60. X. Cao, Y. Hong, N. Zhang, Q. Chen, J. Masud, M. Asle Zaeem, and M. Nath, *ACS Catalysis*, 2018, 8 (9), 8273-8289.

61. C. Chen, M. Shi, M. Xue, Y. Hu, *Rsc Adv.*, 2017, 7, 22208-22214.

62. F. J. Garcia-Garcia, P. Salazar, F. Yubero, A.R. González-Elipe, *Electrochimica Acta*, 2016, 201, 38–44.

63. X.-Y. Lang, H.-Y. Fu, C. Hou, G.-F. Han, P. Yang, Y.-B. Liu, Q. Jiang, *Nature Communications*, 2013, 4:2169.

64. Z. Zhuang, X. Su, H. Yuan, Q. Sun, D. Xiao, and M. M. F. Choi, *Analyst*, 2008,133, 126-132.

65. X. Zhu, Q. Jiao, C. Zhang, X. Zuo, X. Xiao, Y. Liang, J. Nan, *Microchim. Acta*, 2013, 180, 477-483.

66. M.R. Mahmoudian, W.J. Basirun, P. M. Woi, M. Sookhakian, R. Yousefi, H. Ghadimi, Y. Alias, *Materials Science and Engineering C*, 2016, 59, 500-508.

67. K. K. Naik, S. Kumar, C. S. Rout, *RSC Adv.*, 2015, 5, 74585-74591.

68. X. Liua, W. Yanga, L. Chena, J. Jiaa, *Electrochimica Acta*, 2017, 235, 519–526.

69. Z. Cui, H. Yin, Q. Nie, *Journal of Alloys and Compounds*, 2015, 632, 402–407.

70. W. Zhu, J. Wang, W. Zhang, N. Hu, J. Wang, L. Huang, R. Wang, Y. Suo, and J. Wang, *J. Mater. Chem. B*, 2018, 6, 718-724.

71. H. Xu, C. Xia, S. Wang, F. Han, M. K. Akbari, Z. Hai, S. Zhuiykov, *Sensors and Actuators B*, 2018, 267, 93–103.

72. X. Wang, H. Jian, Q. Xiao, S. Huang, *Applied Surface Science*, 2018, 459, 40–47.

73. X. Niu, M. Lan, H. Zhao, C. Chen, *Anal. Chem.*, 2013, 85, 3561−3569.

74. M. Wu, S. Meng, Q. Wang, W. Si, W. Huang and X. Dong, *ACS Appl. Mater. Interfaces*, 2015, 7, 21089–21094.

75. L. Wang, X. Lu, Y. Ye, L. Sun and Y. Song, *Electrochim. Acta*, 2013, 114, 484–493.

76. G. Li, H. Huo, and C. Xu, *J. Mater. Chem. A*, 2015, 3, 4922–4930.

77. F. Huang, Y. Zhong, J. Chen, S. Li, Y. Li, F. Wang, S. Feng, *Anal. Methods*, 2013, 5, 3050–3055.

78. X. Tang, B. Zhang, C. Xiao, H. Zhou, X. Wang, and D. He, *Sens. Actuators B*, 2016, 222, 232–239.

79. G. Zeng, W. Li, S. Ci, J. Jia, Z. Wen, *Scientific Reports*, 2016, 6:36454.

80. H. Liu, X. Wu, B. Yang, Z. Li, L. Lei, X. Zhang, *Electrochimica Acta*, 2015, 174, 745-752.

81. N. Hui, S. Wang, H. Xie, S. Xu, S. Niu, X. Luo, *Sensors and Actuators B*, 2015, 221, 606–613.

82. S. Mani, S. Ramaraj, S.-M. Chen, B. Dinesh, T-W Chen, *Journal of Colloid and Interface Science*, 2017, 507, 378–385.

83. P. K. Kannan, C. Hu, H. Morgan, C. S. Rout, *Chem. Asian J.*, 2016, 11,1837 – 1841.

84. M.A. Kiani, M. AbbasniaTehrani, H. Sayahi, *Analytica Chimica Acta*, 2014, 839, 26-33.

85. C. Xu, Y. Cao, Y. Chen, W. Huang, D. Chen, Q. Huang, J. Tu, *Eur. J. Inorg. Chem.*, 2016, 3163–3168.

86. L. Zhang, C. Ye, X. Li, Y. Ding, H. Liang, G. Zhao, Y. Wang, *Nano-Micro Lett.*, 2018, 10:28.

87. T.-W. Lin, C.-J. Liu and C.-S. Dai, *Appl. Catal. B*, 2014, 154–155, 213–220.

88. S. Kim, S. H. Lee, M. Cho, Y. Lee, *Biosensors and Bioelectronics*, 2016, 85, 587–595.

89. H. Huo, Y. Zhao and C. Xu, *J. Mater. Chem. A*, 2014, 2, 15111-15117.

90. X. Luo, M. Huang, L. Bie, D. He, Y. Zhangb, and P. Jiang, *RSC Adv.*, 2017, 7, 23093-23101.

91. B. Wang, Y. Cao, Y. Chen, X. Lai, J. Peng, J. Tu, X. Li, *Nanotechnology*, 2017, 28, 025501 (11pp).

92. E. Zhang, Y. Xie, S. Ci, J. Jia, Z. Wen, *Biosens. Bioelectron.*, 2016, 81, 46–53.

93. Y. Zhang, L. Luo, Z. Zhang, Y. Ding, S. Liu, D. Deng, H. Zhao, Y. Chen, *J. Mater. Chem. B*, 2014, 2, 529-535.

94. B. Xue, K. Li, L. Feng, J. Lu, L. Zhang, *Electrochimica Acta*, 2017, 239, 36-44.

95. Y. Ding, Y. Wang, L. Su, M. Bellagamba, H. Zhang, Y. Lei, *Biosensors and Bioelectronics*, 2010, 26, 542-548.

96. C. Lee, S. H. Lee, M. Cho, Y. Lee, *Microchim Acta*, 2016, 183, 3285–3292.

97. R. Boukherroub, S. Szunerits, *J. Mater. Chem. A*, 2014, 2, 5525–5533.

98. Y. Liu, X. Cao, R. Kong, G. Du, A. M. Asiri, Q. Lu, and X. Sun, *J. Mater. Chem. B*, 2017, 5, 1901–1904.

99. Kh. Ghanbari, Z. Babaei, *Analytical Biochemistry*, 2016, 498, 37-46.

100. Y. Zhang, Y. Wang, J. Jia, J. Wang, *Sensors and Actuators B: Chemical*, 2012, 171, 580-587.

101. A. Sun, J. Zheng, Q. Sheng, *Sensors and Actuators B: Chemical*, 2012, 65, 64-69.

102. H. Yang, Y. Zhu, *Biosens. Bioelectron.*, 2007, 22, 2989–2993.

103. R. Kumar, T. Bhuvana, P. Rai, A. Sharma, *Journal of The Electrochemical Society*, 2018, 165 (2), B1-B8.

104. R. Ahmad, N. Tripathy, M.-S. Ahn, K. S. Bhat, T. Mahmoudi, Y. Wang, J.-Y. Yoo, D.-W. Kwon, H.-Y. Yang, Y.-B. Hahn, *Scientific Reports*, 2017, 7:5715.

105. C. Zhao, X. Wu, X. Zhang, P. Li, X. Qian, *Journal of Electroanalytical Chemistry*, 2017, 785, 172–179.

106. X. Lia, J. Liu, X. Ji, J. Jiang, R. Ding, Y. Hu, A. Hu, X. Huang, *Sensors and Actuators B: Chemical*, 2010, 147, 241-247.

107. Z.D. Gao, J. Guo, N.K. Shrestha, R. Hahn, Y.Y. Song, P. Schmuki, *Chem. Eur. J.*, 2013, 19, 15530–15534.

SUPPORTING INFORMATION

ULTRASENSITIVE AND HIGHLY SELECTIVE NON-ENZYMATIC GLUCOSE SENSOR BASED ON $CoNi_2Se_4$ /RGO NANOCOMPOSITE

Bahareh Golrokh Amin, Jahangir Masud, and Manashi Nath

Department of Chemistry, Missouri University of Science and Technology, Rolla, MO 65409.

Electrochemically Active Surface Area (ECSA)

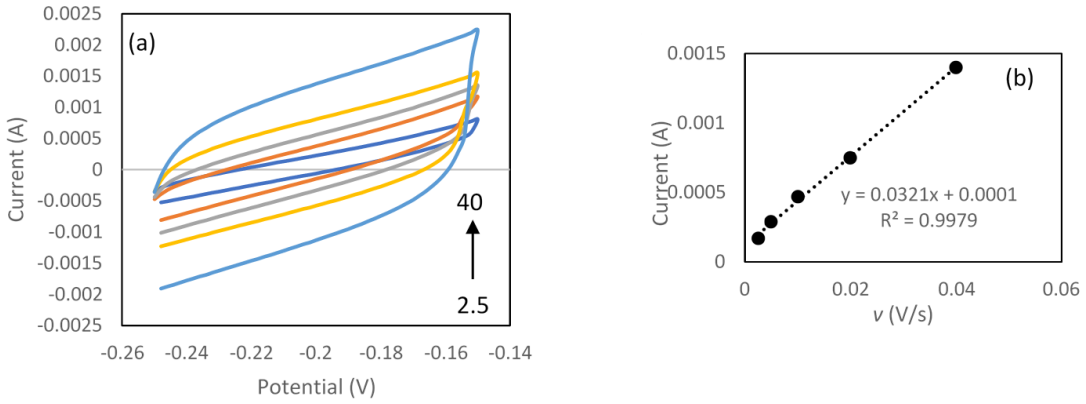

Figure S1. Electrochemically active surface area analysis of (a) CoNi2Se4-rGO@NF at different scan rates, (b) linear fitting of capacitive currents vs. scan rate.

Surface Characterizations

SEM and EDS

A FEI Helios Nanolab 600 FIB/FESEM at an acceleration voltage of 10 kV and a working distance of 5.0 mm was employed to obtain SEM image of the modified

electrode surfaces. Energy dispersive spectroscopy (EDS) accompanied by line scan analysis was also acquired from the SEM microscope.

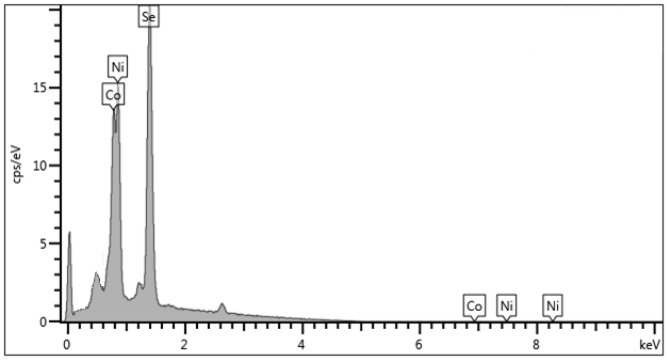

Figure S2. EDS of $CoNi_2Se_4$ on Ni Foam.

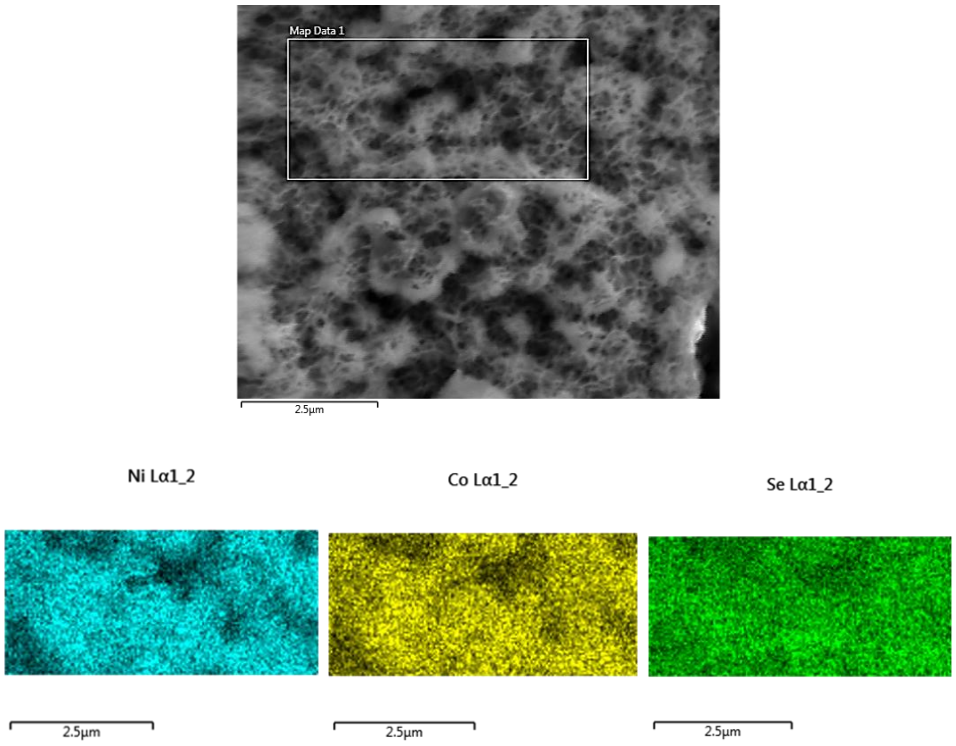

Figure S3. Elemental mapping of $CoNi_2Se_4$ on Ni Foam.

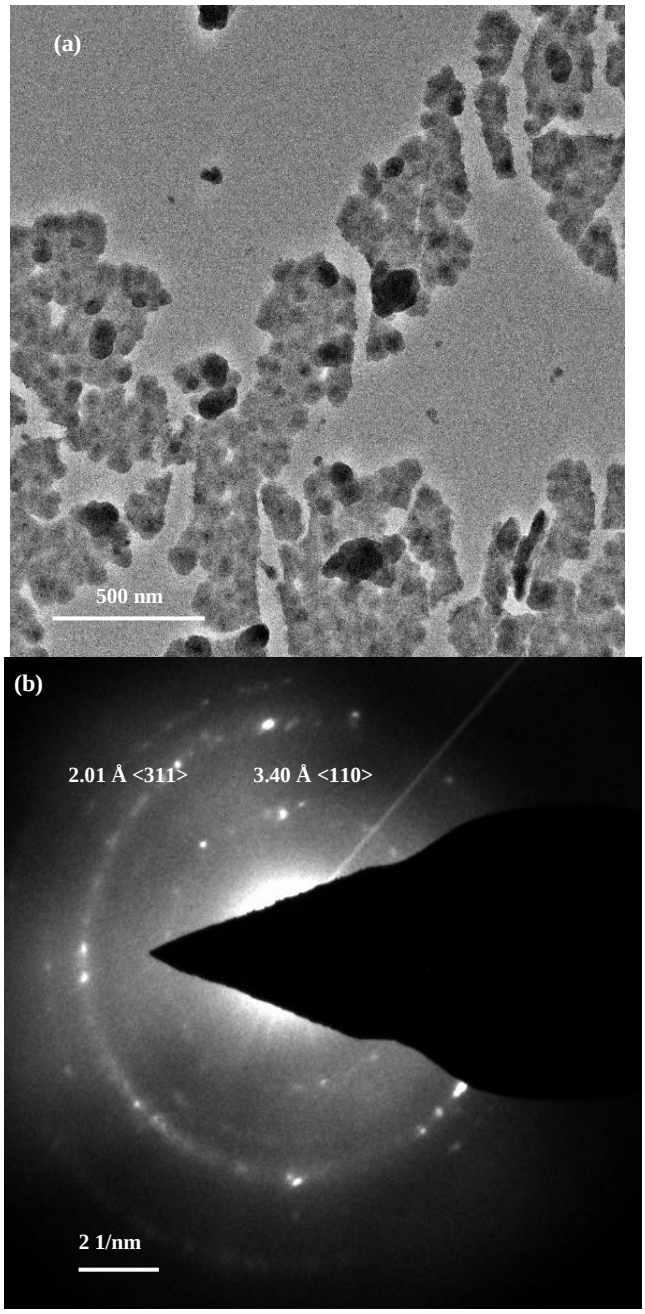

Figure S4. TEM image (a) and SAED pattern (b) of $CoNi_2Se_4$ catalyst.

XPS

KRATOS AXIS 165 X-ray Photoelectron Spectrometer using monochromatic Al X-ray source was used for all XPS measurements of the catalyst.

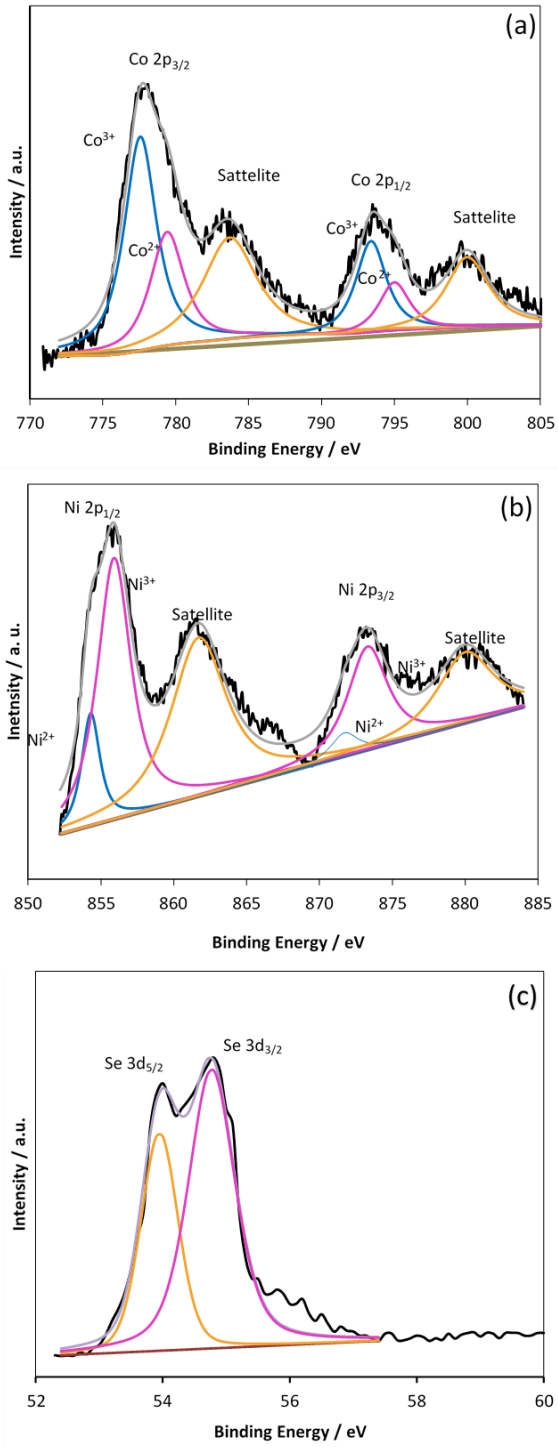

Figure S5. XPS of as-synthesized $CoNi_2Se_4$-rGO (Ni 2p, Co 2p, and Se 3d).

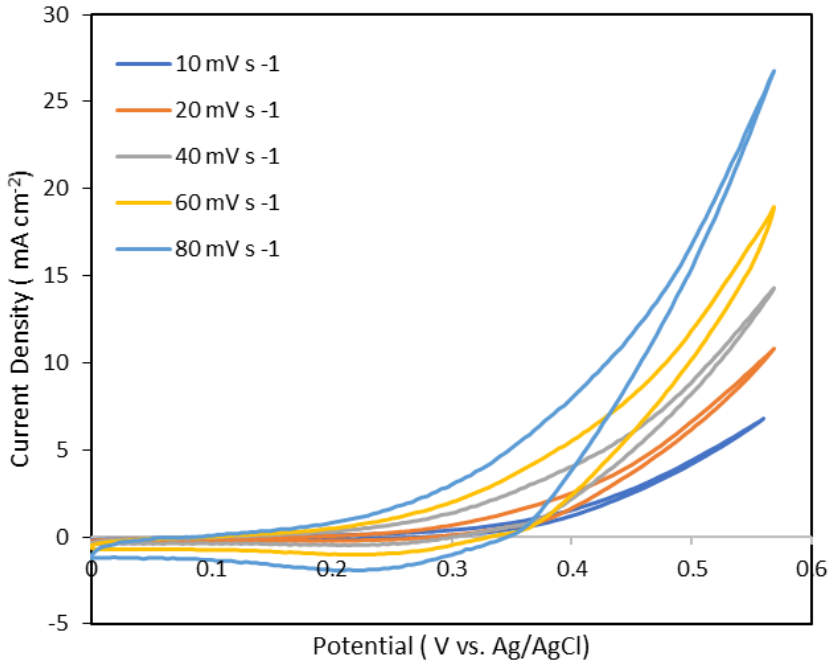

Figure S6. Cyclic voltammetry of reduced graphene oxide on Ni Foam at various scan rates at presence of 0.1 mM glucose.

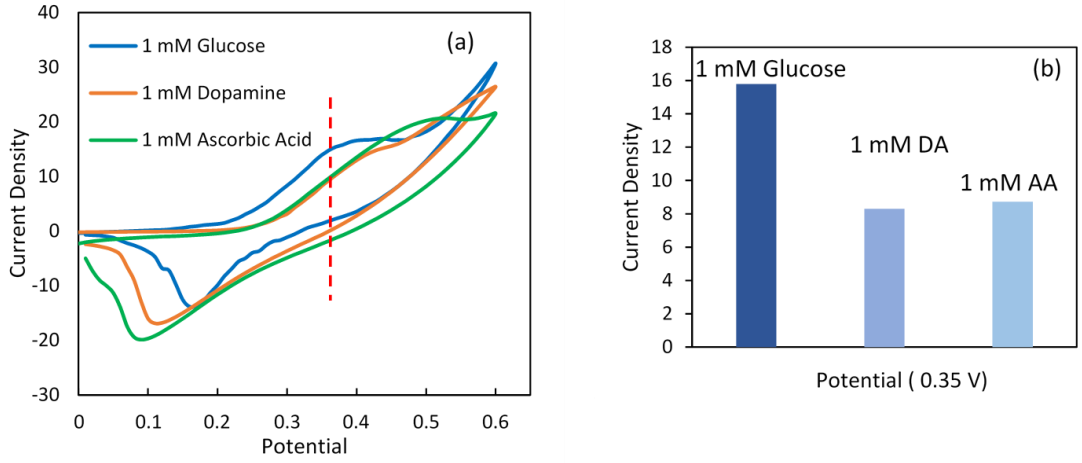

Figure S7. Selectivity of $CoNi_2Se_4$-rGO towards glucose (a) CVs of $CoNi_2Se_4$-rGO@NF in presence of 1mM of Dopamine, ascorbic acid and glucose solution separately at the same potential (0.35 V) (b) current densities at 0.35 V for 1 mM glucose, 1mM dopamine or 1 mM ascorbic acid solutions. Current densities in both plots are in mA/cm^2.

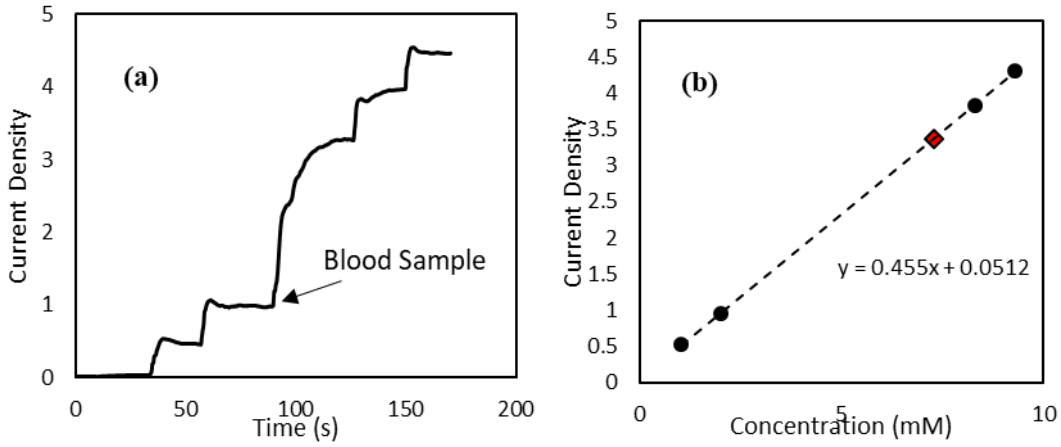

Figure S8. A typical electrochemical measurement for blood glucose determination performed through (a) amperometric response of $CoNi_2Se_4$-rGO@NF upon the addition of blood sample in 0.05 M NaOH at an applied potential of 0.35 V vs. Ag|AgCl. Current density is in mA/cm^2. (b) estimating the glucose level from the fitted linear plot of current response vs. glucose concentration.

III. ULTRASENSITIVE AND HIGHLY SELECTIVE Ni_3Te_2 AS A NON-ENZYMATIC GLUCOSE SENSOR AT EXTREMELY LOW WORKING POTENTIAL

Bahareh Golrokh Amin, Jahangir Masud, and Manashi Nath

Department of Chemistry, Missouri University of Science and Technology, Rolla, MO 65409

ABSTRACT

Developing non-enzymatic glucose biosensors has recently been at the center of attention owing to their potential application in implantable and continuous glucose monitoring system. In this article nickel telluride nanostructures with the generic formula of Ni_3Te_2 has been reported as a highly efficient electrocatalyst for glucose oxidation, functional at a low operating potential. Ni_3Te_2 nanostructures were prepared by two synthesis methods, direct electrodeposition on the electrode, and hydrothermal method. The electrodeposited Ni_3Te_2, exhibited a wide linear range of response corresponding to glucose oxidation exhibiting a high sensitivity of 41.615 mA cm^{-2} mM^{-1} and a low limit of detection (LOD) of 0.43 µM. The hydrothermally synthesized Ni_3Te_2 on the other hand, also exhibits an ultra-high sensitivity of 35.213 mA cm^{-2} mM^{-1}, and a LOD of 0.38 µM. The observation of high efficiency for glucose oxidation for both Ni_3Te_2 electrodes irrespective of synthesis method further confirms the enhanced intrinsic property of the material towards glucose oxidation. In addition to high sensitivity and low LOD, Ni_3Te_2 electrocatalyst also has good selectivity and long-term stability in 0.1 M KOH solution. Since it is operative at low applied potential of 0.35 V vs. Ag|AgCl, interference from

other electrochemically active species is reduced thus increasing the accuracy of this sensor.

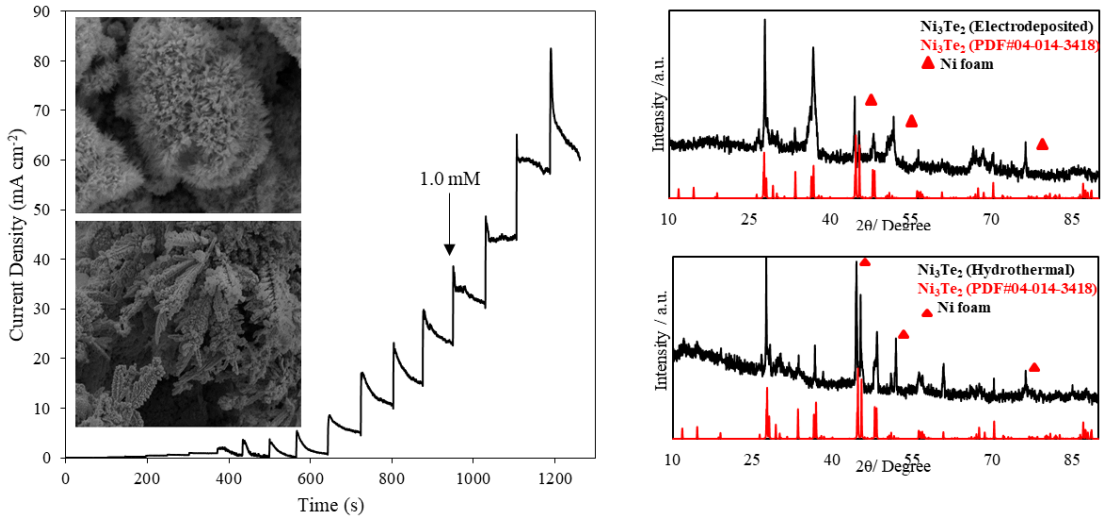

1. INTRODUCTION

In current society, diabetes has rapidly grown to be one of the leading causes of death on a global scale. Diabetes stems from abnormal blood glucose level and frequent self-monitoring and continuous testing of physiological glucose concentration is key to controlling advancement of the disease. Continuous blood glucose monitoring allows for better glycemic control, resulting in lesser fluctuation of blood glucose levels in diabetic patients. By better monitoring of the glucose concentration in blood, patients are more likely to prevent occurrence of diabetic emergencies such as hypoglycemia or hyperglycemia, as well as to avoid long-term complications associated with the disease, such as kidney failure, blindness, and high blood pressure.[1-4] The conventional approach for monitoring spread of the disease and controlling it, involves regular sampling of the

blood glucose level via finger pricking which causes anxiety, tension, and additional pain to the patients. Also, relying on blood samples collected at various times throughout the day under different physiological conditions, will provide sporadic results of glucose levels, making this approach less reliable for the purpose of administering insulins.[5, 6] Therefore, researchers are trying to develop more convenient glucose sensors, capable of continuously and reproducibly measuring glucose levels at different concentration.

With the advent of modern monitoring devices, a highly sensitive and accurate glucose measuring system should be able to reliably detect glucose from blood as well as alternative biofluids, including saliva, urine, sweat, etc. If diabetic patients are provided with such non-invasive and convenient glucose sensors, they are more likely to measure frequent glucose levels, which will allow them to optimize their insulin injections.[7, 8] However, glucose concentration in these body fluids are as low as 0 to 0.8 mmol L^{-1} for urine,[9] 0.03 to 0.08 mmol L^{-1} for saliva,[10] and 0.02 to 0.6 mmol L^{-1} for sweat,[11] requiring the glucose sensors to be highly sensitive with extremely low limit of detection (LOD) and better selectivity. The rapid response time and precise measurements achievable by electrochemical sensing methods have made glucose detection possible from body fluids other than blood.[12] However, conventionally used enzyme-based glucose sensors still fall short of these requirements since their efficiencies are influenced by changes in pH and variation of temperature in addition to difficulty of immobilizing fragile enzyme on the electrode surface. The efficiency of enzymatic glucose sensors can also be affected by the presence of other interfering compounds in blood.[13-16] Due to the high working potential required for electron transfer between thick enzyme layer and glucose molecules, other redox-active species present in blood can also oxidize/degrade, thus, affecting the

accuracy of glucose sensing.[17] According to recent research developments, all the crucial parameters including sensitivity, selectivity, LOD, and stability can be improved by employing the next-generation glucose sensing modules, namely the non-enzymatic glucose sensors.[18, 19] While enzyme-based sensors are dependent on thick enzymes to mediated electron transfer, in non-enzymatic glucose biosensors on the other hand, the process of glucose oxidation takes place directly on the electrode surface. Specific glucose oxidation electrocatalysts anchored on the electrode surface facilitates the electron transfer process at the electrode-analyte interface, thereby, decreasing the operating potential for glucose oxidation and improving efficiency of the sensor.[20-25]

Among non-enzymatic electrochemical glucose sensors, noble metals such as Au-based,[26-30] Pt-based,[31, 32] or Pd-based,[33, 34] and their alloys exhibit an enhanced conductivity with an accelerated electrochemical redox process for glucose biosensing. However, scarcity and cost of these precious metals inhibit their large-scale usage in practical implementations.[35-40] To mitigate this issue, nanocatalysts based on earth-abundant transition metals have received great attention in virtue of their excellent redox behavior, natural abundance, lower cost, functional stability in alkaline medium, and satisfactory biocompatibility.[41-43] Among transition metals, Ni-based catalysts are of interest for electrochemical non-enzymatic glucose sensing owing to their low cost and remarkably high catalytic activity arising from the facile transformation of Ni^{2+}/Ni^{3+} redox couple in alkaline medium, which facilitates electrooxidation of glucose on the electrode surface.[44-47]

Recent studies by several researchers have shown that nickel chalcogenides based electrocatalysts possess unprecedented electrochemical activity towards several energy

conversion processes such as full water splitting[48-51] and supercapacitors.[52, 53] Such enhancement of electrocatalytic activity on the Ni-chalcogenides compared to their oxide analogue is caused by the facile electrochemical redox of the active Ni center as well as decreased bandgap and increased metallicity of the chalcogenide lattice compared to the oxides which are higher bandgap insulators. The higher conductivity of the lattice also enhances electron transfer efficiency within transition metal selenides and tellurides composites compared to that in the corresponding oxides. The trend in catalytic activity from the oxides to the other chalcogenide series (sulfides, selenides, and tellurides) can also be explained through their gradual change in electronegativity of the chalcogen atom. As the electronegativity of the chalcogen atom decreases down the series, the degree of covalency in metal–chalcogen bond increases. Since, the electrocatalytic efficiency is enhanced by a higher degree of covalency in metal–anion bonding, it is expected that the catalytic efficiency will increase in the chalcogenide series from oxide to telluride.[48, 53] The larger applied potentials required for nickel-based oxides decreases the efficiency of these electrodes towards glucose biosensing. Ni-chalcogenides on the other hand, being electrochemically active at a much lower applied potential can significantly increase the catalytic efficiency for direct glucose oxidation.[54, 55]

In this study, electrocatalytic activity of nickel telluride nanostructures with the molecular formula of Ni_3Te_2 has been reported for direct glucose oxidation in alkaline medium. The Ni_3Te_2 electrocatalyst composite has been synthesized by two approaches: direct electrodeposition, as well as one-step hydrothermal synthesis. Both of these catalyst composites show similar activity towards oxidation of glucose to gluconolactone indicating that it is indeed an intrinsic property for Ni_3Te_2 independent of synthesis

method. A high sensitivity and low LOD was obtained with the Ni_3Te_2 electrocatalyst at low applied potentials for glucose oxidation, making this compound promising for non-enzymatic glucose biosensors.

2. EXPERIMENTAL

All chemicals used in this research were used as-purchased, without further purification. Nickel sulfate ($NiSO_4.6H_2O$) was purchased from Fisher Scientific, tellurium dioxide (TeO_2) and hydrazine hydrate ($N_2H_4.H_2O$) were purchased from Acros Organics. Dextrose and dopamine were purchased from Sigma-Aldrich, ascorbic acid, sodium chloride, potassium chloride and lactose were obtained from Fisher-Scientific, and fructose from Aldrich. Ni Foam was employed as substrate in both electrodeposition and hydrothermal synthesis. Deionized water (DI water) was used to prepare all the solutions. Ni foam was rinsed with dilute HCl and DI water prior to preparation of Ni_3Te_2 electrode.

2.1. ELECTRODEPOSITION OF Ni_3Te_2

Direct electrodeposition was carried out in a conventional three-electrode system using an IviumStat potentiostat, with Ni-foam is working electrode, Pt as counter and Ag|AgCl as reference electrode. The electrolyte contained 15 mM of nickel sulfate and 3 mM tellurium dioxide and was maintained at 80 °C with a pH of 2.5 by addition of dilute HCl. Ni_3Te_2 was deposited on pre-cleaned Ni foam at -1.05 V (vs. Ag|AgCl).

2.2. HYDROTHERMAL SYNTHESIS OF Ni_3Te_2

$NiSO_4 \cdot 6H_2O$ (9.0 mM) was dissolved in 15.0 mL of deionized water under vigorous magnetic stirring. Then, TeO_2 (6.0 mM) was added to the reaction mixture and stirred for 20 min to form a homogeneous solution. Finally, $N_2H_4 \cdot H_2O$ (3.0 mL) was added to the mixture and stirred continuously for another 10 min. The resulting solution was transferred into a Teflon-lined stainless-steel autoclave. Pre-cleaned Ni foam was placed inside the autoclave which was sealed and maintained at 185 °C for 20 h. Later, it was naturally cooled down to room temperature. The prepared electrode was washed several times with DI water to remove impurities. The product was dried in a vacuum oven at 60 °C for 24 h.

Detailed description of synthesis procedure and morphological and structural studies has been reported in our previous work.[48]

3. CHARACTERIZATION

Powder X-ray diffraction (PXRD). The obtained electrodeposited and hydrothermally synthesized Ni3Te2 samples were characterized by powder X-ray diffraction measurements using a Philips X-Pert X-ray diffractometer (PANalytical, Almelo, The Netherlands, $\lambda = 1.5418$ °A). The PXRD pattern was collected from 2 theta values of 10° to 90°.

Scanning electron microscopy (SEM). SEM images of Ni_3Te_2 was acquired using a FEI Helios NanoLab 600 FIB/FESEM operating at an acceleration voltage of 10 kV and a working distance of 5.0 mm to study the morphology of the product.

4. RESULTS AND DISCUSSION

4.1. MORPHOLOGY AND COMPOSITION

SEM image of the as-grown electrodeposited films show randomly oriented nanoflakes on the surface of Ni foam as shown in Figure 1a. Such nanoflake geometry expectedly increases the active surface area of the electrocatalyst composite leading to a better exposure of the catalytic sites to the analyte present in the electrolyte thus improving catalytic interaction. SEM image of the hydrothermally synthesized Ni_3Te_2, on the other hand, shows leaf-like dendritic nanostructures on the catalyst surface (Figure 1c). It is worth mentioning that Ni_3Te_2 grown on Ni foam both by electrodeposition as well as hydrothermal methods show high surface area amenable for superior catalytic activity.

The PXRD patterns of the electrodeposited Ni_3Te_2 as well as the hydrothermally synthesized Ni_3Te_2 on Ni foam (NF) shows the presence of pure Ni_3Te_2, where the diffraction peaks matched with those reported for standard Ni_3Te_2 (PDF # 04-014- 3418) as shown in Figures 1b and 1d. Both PXRD patterns show that the product formed was pure phase with no other evident impurity peaks. It was also observed that the relative peak intensities and peak widths were different between the hydrothermally synthesized and electrodeposited Ni_3Te_2. Such differences can be explained by the smaller nanostructures in the electrodeposited sample which causes broadening of the diffraction peak, and possible oriented growth in the electrodeposited film, which has been previously observed for $NiSe_2$.[51]

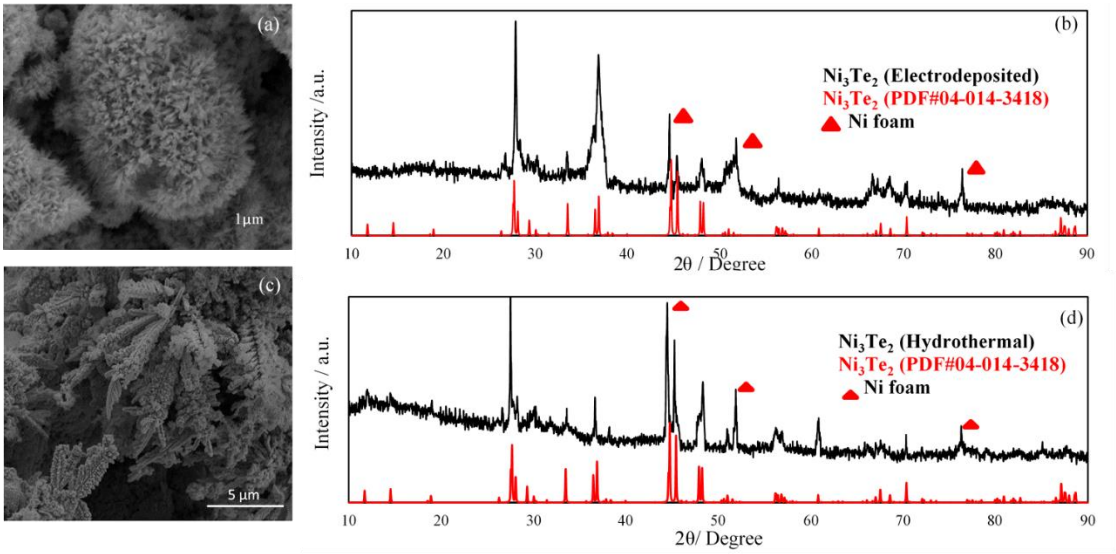

Figure 1. Characterization of electrodeposited Ni_3Te_2 catalyst. (a) SEM image on Ni foam. (b) PXRD patterns of electrodeposited Ni_3Te_2 on Ni foam. Characterization of Hydrothermally synthesized Ni_3Te_2. (c) SEM image on Ni_3Te_2-NF. (d) PXRD analysis of hydrothermally synthesized Ni_3Te_2 catalysts along with the reference (PDF # 04-014-3418) pattern.

Electrochemical Measurements: Cyclic voltammetry (CV) and chronoamperometry measurements were performed with an Iviumstat potentiostat under continuous stirring in a three-electrode electrochemical setup, where Ni_3Te_2-NF served as working electrode while a platinum mesh and Ag|AgCl electrode selected as the counter and reference electrodes, respectively. An aqueous 0.1 M KOH solution was used as the electrolyte. The limit of detection (LOD) was calculated according to the following equation (Equation 1):[56-58]

$$LOD = \frac{3SD}{N} \quad (1)$$

where SD is the standard deviation of the analyte concentration calculated from the current response of consecutive addition of glucose into the electrolyte and N is the slope

of the calibration curve which indicates the sensitivity of the electrode with signal-to-noise ratio of 3.

The electrochemical active surface area (ECSA) was estimated by measuring the double layer charging current at different scan rates based on the following equation (Equation 2):[49]

$$\text{ECSA} = \frac{C_{dl}}{C_s} \quad (2)$$

where C_s is the specific capacitance (0.040 mF cm^{-2}) in N_2 saturated 0.1 M KOH solution and C_{DL} is the double layer capacitance calculated from the slope of the plot of capacitive current (i_{DL}) in a non-faradaic double-layer region against scan rate v (V s^{-1}). The ECSA was measured to be 13.0 cm^2 for electrodeposited Ni_3Te_2 and 20.2 cm^2 for hydrothermally synthesized Ni_3Te_2 as shown in supplementary information (Figure S1 and Figure S2, respectively).

4.2. ELECTROCHEMICAL BEHAVIOR OF ELECTRODEPOSITED Ni_3Te_2-NF ELECTRODE

Cyclic voltammetry (CV) is known to be useful for investigating the electrochemical behavior of the electrode. The CV plots and influence of the scan rate on the current density of electrodeposited Ni_3Te_2 in 0.1 M KOH in absence of glucose is provided in Figure 2a. As shown in Figure. 2a and Figure S1, by increasing the scan rate from 10 mV s^{-1} to 80 mV s^{-1}, current density changes proportionally with the square root of scan rate, implying a typical diffusion-controlled electrochemical process at the surface of the electrode.

The CV response of electrodeposited Ni_3Te_2-NF electrode in presence of different concentrations of glucose in the electrolyte are presented in Figure 2b. It can be seen from this figure that an explicit oxidation peak located at 0.35 V vs. Ag|AgCl was observed in the presence of glucose with concentrations ranging from 1 mM to 4 mM. The enhancement of anodic peak current densities was more obvious with the increase of glucose concentration, suggesting high electrocatalytic activity of electrodeposited Ni_3Te_2 towards glucose electro-oxidation. It is worth mentioning that upon addition of 1.0 mM glucose, bare Ni foam did not show any oxidation peak corresponding to glucose oxidation in the working potential ranging from 0 to 0.5 V vs. Ag|AgCl (Figure S3), confirming that the substrate by itself was not an active electrocatalyst for glucose oxidation.

The large current densities achieved by electrodeposited Ni_3Te_2 electrode in presence of 4 mM glucose concentration, reveals another potential application of this electrode in non-enzymatic glucose fuel cell.[59] Currently, the development of implantable medical devices has been limited due to the slow improvements in lithium ion battery technology. Glucose fuel cells are potential candidates to replace the lithium ion batteries due to their superior long-term stability, sufficient power density and abundancy of glucose in body to generate a continuous and stable power output. However, the main challenge for enzymatic glucose fuel cells is the poor anode selectivity towards glucose oxidation in the presence of oxygen in body tissue.[50-62] Non-enzymatic glucose fuel cell with a high current response and excellent selectivity can be a feasible solution for improvements in power generation for implantable medical devices. It can be concluded

from Figure 2b that electrodeposited Ni_3Te_2 can be a potential choice for this technology, as it shows a high current density of about 45 mA cm^{-2} in presence of 4 mM glucose.

4.3. ELECTROCATALYTIC OXIDATION OF GLUCOSE ON ELECTRO-DEPOSITED Ni_3Te_2

A high amperometric current response in the detection of glucose can be strongly affected by the applied potential. Large applied potential can trigger oxygen evolution reaction at the anode, which leads to a large background anodic current and dwindling of the active surface area.[63] Therefore, to determine the optimum working potential for glucose sensing, the amperometric response of the Ni_3Te_2-NF electrode was recorded at different applied potentials. As Figure 2c shows, with successive addition of 0.01 mM of glucose into a 0.1 M KOH solution, the catalytic current of electrodeposited Ni_3Te_2-NF electrode elevated with the increase of applied potential from 0.30 V to 0.35 V, but then decays at 0.40 V potential. Therefore, 0.35 V vs. Ag|AgCl, was selected as the optimal applied potential for electrodeposited Ni_3Te_2 electrode which enables the best sensing performance for glucose oxidation. It should be noted here that this is one of the lowest potentials reported for electrocatalytic glucose oxidation and is much lower than that of oxide-based sensors. The onset of electrocatalytic glucose oxidation at such low working potential validates our initial hypothesis and confirms that replacing oxides by chalcogenides such as selenides and telluride, enhances electrode activation at lower potential and results in a high selectivity of the electrode.[64] Additionally, the reduced bandgap in selenides and tellurides leads to better electrical conductivity and charge transfer in the catalyst composite and a high current densities at low applied potentials.

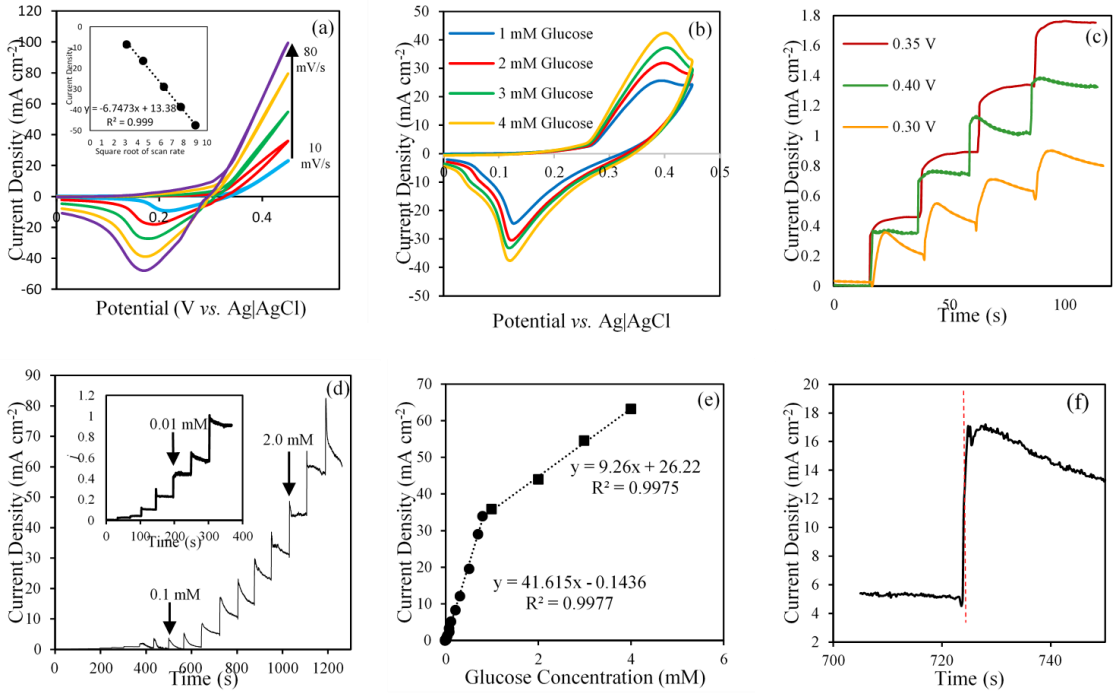

Figure 2. Electrocatalytic performance of electrodeposited Ni_3Te_2. (a) Cyclic voltammograms of electrodeposited Ni_3Te_2 at different scan rates. Onset shows cathodic peak currents of electrodeposited Ni_3Te_2 electrode vs. square root of scan rate. (b) Response of electrodeposited Ni_3Te_2-NF electrode in 0.1 M KOH containing 1, 2, 3 and 4 mM of glucose at scan rate of 10 mV s^{-1}. (c) Effect of various potentials on amperometric response of electrodeposited Ni_3Te_2 electrode to successive addition of 0.01 mM glucose. (d) Amperometric response of electrodeposited Ni_3Te_2 upon addition of different concentrations of glucose at 0.35 V. Inset shows the amperometric response in low glucose concentration. (e) The corresponding calibration curve of the response current density as a function of glucose concentration. (f) Response time of the sensor to achieve steady-state current density upon addition of glucose.

The mechanism of glucose oxidation is believed to be initiated by the hydroxyl attachment on the catalytically active transition metal site, Ni (III), which is generated *in situ* through local site-oxidation (catalyst activation). The electron transfer is then initiated between the glucose molecule and the hydroxyl activated catalytic site leading to glucose oxidation to gluconolactone and further redox of the transition metal catalytic site.[65] Since the catalytically active transition metal site undergoes a reversible oxidation-

reduction cycle during the mechanism of glucose oxidation, the redox potential for the transition metal sites can have a large influence on the catalytic efficiency for glucose oxidation, especially the applied potential value. Our previous studies have shown that the Ni^{2+}/Ni^{3+} redox potential can be shifted to more cathodic potential in Ni_3Te_2 compared to Ni-oxides,[48] thereby reducing the applied potential for catalyst activation.

The amperometric response of the electrodeposited Ni_3Te_2-NF was measured at constant applied potential of 0.35 V with successive addition of different concentrations of glucose into the alkaline solution under continuous stirring and has been shown in Figure 2d. Inset shows magnified version of amperometric response at low glucose concentrations.

As can be seen from these plots, the current response illustrated high sensitivity of the electrode to glucose concentration as low as 0.01 µM, which can easily be detected by electrodeposited Ni_3Te_2 electrode. The calibration curve shown in Figure 2e, obtained by plotting the steady-state current density values versus the glucose concentrations, reveals two linear regions. In the low glucose concentration ranges from 0.01 µM to 0.8 mM, the response is linear with an ultra-high sensitivity of 41.615 mA mM^{-1} cm^{-2} (R^2 = 0.9977). While, the second linear region between 1 mM to 4 mM shows a sensitivity of 9.26 mA mM^{-1} cm^{-2} (R^2 = 0.9975). For the linear range from 0.01 µM – 0.8 mM, based on Equation 1, the LOD was estimated to be 0.43 µM with a signal to noise ratio of 3 (S/N = 3).

As can be seen from Figure 2f, a rapid current response was achieved upon the addition of glucose, reaching the steady-state current in less than 2 seconds. The fast

response time demonstrates competent activity of electrodeposited Ni_3Te_2 electrode towards glucose sensing.

Figure 3a shows the amperometric responses of electrodeposited Ni_3Te_2 to stepwise injections of 0.01 mM of glucose to 0.1 M KOH at 0.35 V wherein, different batches of electrodes were measured under identical experimental conditions. It was observed that addition of similar concentration of glucose resulted in almost identical jumps in current density. This confirms the reliability of Ni_3Te_2 as a sensor as well as its functional stability in alkaline medium, along with reproducibility of the results.

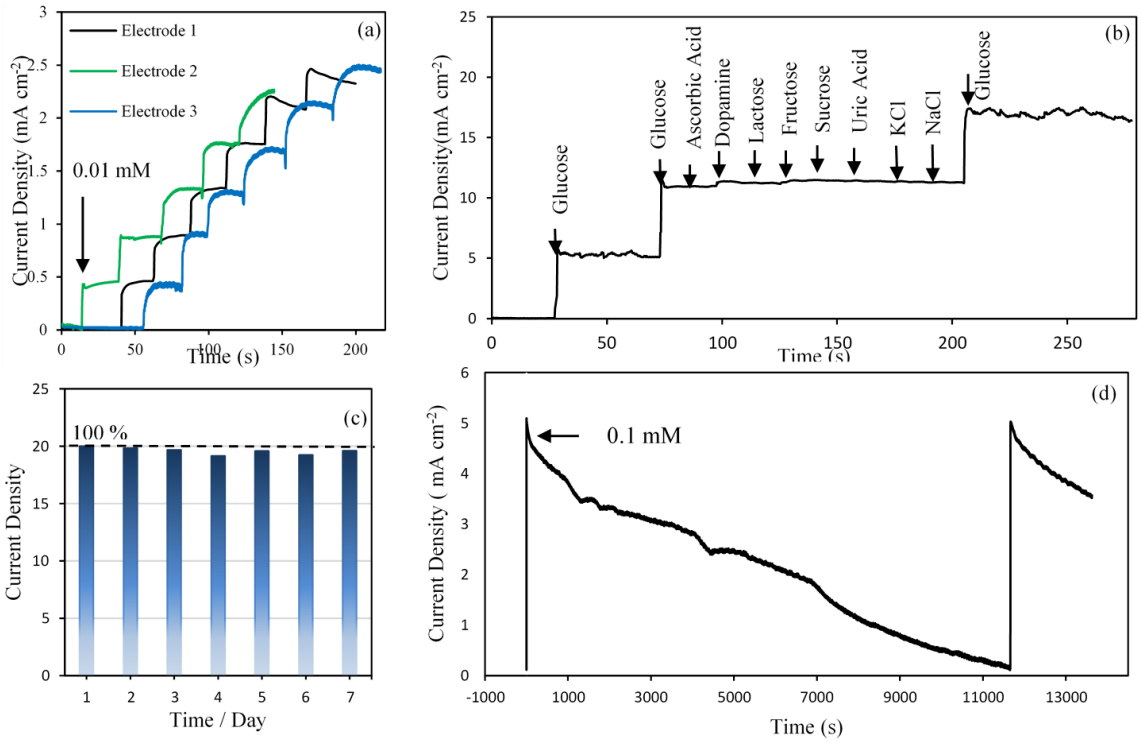

Figure 3. Selectivity and stability of electrodeposited Ni_3Te_2. (a) Amperometric response of electrodeposited Ni_3Te_2 to successive addition of 0.01 mM glucose at 0.35 V. (b) Interference assessment performance of the electrodeposited Ni_3Te_2 upon the addition of 0.1 mM glucose and 0.01 mM of interfering species as identified in the diagram. (c) The long-term stability check of the electrode measured for 7 days. (d) Prolonged chronoamperometry test with addition of 0.1 mM glucose to 0.1 M KOH.

For an electrochemical glucose sensor, selectivity is a crucial feature to assess the ability of the electrode to be utilized in practical applications. Normally, certain biomolecules such as ascorbic acid, fructose, sucrose, and lactose, co-exist with glucose in human blood. These interfering species may also under electrochemical oxidation thus producing background current signal at high applied potentials, which will affect the determination of glucose concentration accurately. Hence an experiment was conducted for examining selectivity of the electrodeposited Ni_3Te_2-NF electrode, where amperometric current response of electrodeposited Ni_3Te_2 to sequential addition of 0.1 mM of glucose and 0.01 mM of a number of interfering compounds including ascorbic acid, dopamine, lactose, fructose, sucrose, uric acid, KCl, and NaCl was measured at an applied potential of 0.35 V vs. Ag|AgCl and the results has been shown in Figure 3b. It is clearly seen that the electrochemical signals from interferant species are negligible compared to the significant jump of current density observed with addition of glucose confirming superior selectivity of Ni_3Te_2 electrode towards glucose oxidation.

Long-term stability and repeatability of the Ni_3Te_2-NF electrode towards glucose sensing was estimated by checking the electrode response to addition of similar concentration of glucose over a week where the electrode was stored under ambient conditions and reused. Figure 3c shows the results of these tests and it can be clearly seen that the electrode produced similar response throughout indicating stability and repeatability of the sensor. Even after being exposed to air for 7 days, electrodeposited Ni_3Te_2 retained at least 96% of its original current response. The reproducibility of the electrode towards the glucose oxidation was also tested by adding 0.1 mM of glucose to 0.1 M KOH under constant stirring. After almost three hours, electrodeposited Ni_3Te_2

completely oxidized all the added glucose reducing the current density to nearly zero. Fresh addition of 0.1 mM of glucose at this point immediately increased the current density to a value almost similar to the previous value as shown in Figure 3d, confirming the reproducibility of current response of the sensor.

4.4. ELECTROCHEMICAL BEHAVIOR OF HYDROTHERMALLY SYNTHESIZED Ni_3Te_2

Hydrothermally synthesized Ni_3Te_2 were assembled on the electrode surface as discussed above. Similar to electrodeposited Ni_3Te_2, hydrothermally synthesized Ni_3Te_2 was also tested for glucose sensing in 0.1 M KOH by collecting CV scans in the absence and presence of glucose. The CV plots shown in Figure 4a represent the current response in absence of glucose and were performed in the potential range from 0 to +0.45 V vs. Ag|AgCl with scan rates increasing from 10 to 80 mV s^{-1}. The cathodic current measured was proportional to the square root of scan rate as shown in the inset, suggesting a typical diffusion-controlled process for the hydrothermally prepared Ni_3Te_2-electrode.

Upon the addition of different concentrations of glucose ranging from 1 to 4 mM, notable enhancement of the anodic current density was observed while the peak oxidation potential stayed at the almost same position, demonstrating the electrode's activity towards glucose oxidation. It is well-established that the enhancement of the oxidative current is attributed to the electro-oxidation of glucose in presence of Ni (III).[66]

The high current density of almost 30 mA cm^{-2} is achieved by the hydrothermally prepared Ni_3Te_2 in the presence of 4 mM glucose. This result shows that the hydrothermally prepared Ni_3Te_2 electrodes, similar to those made through

electrodeposition, have the potential of being used in devices for energy conversion from glucose.

4.5. GLUCOSE OXIDATION WITH HYDROTHERMALLY PREPARED Ni_3Te_2 ELECTRODE

As mentioned above, applied potential can strongly affect the magnitude of current response for the glucose sensor. Therefore, we have analyzed the current response with respect to variations in applied potential to select the optimal potential. Figure 4c shows the amperometric responses of hydrothermally synthesized Ni_3Te_2 to the sequential addition of 0.1 mM of glucose at different applied potentials ranging from 0.30 V to 0.40 V. Based on the observed current response, the optimal potential for the amperometric detection of glucose was selected to be 0.35 V vs. Ag|AgCl, which aligns with CV results mentioned above.

Amperometric response upon successive addition of different concentrations of glucose into constantly stirred 0.1 M KOH solution was measured at 0.35 V and has been shown in Figure 4d. In this figure, distinct increases in amperometric currents were observed with the stepwise increase of the added glucose concentration, demonstrating the superior catalytic ability of hydrothermally prepared Ni_3Te_2 electrode for glucose electrooxidation. Inset shows the current response of the sensor in the region of low added glucose concentrations confirming the ability of the sensor to reliably detect even minute amounts of glucose which leads to high sensitivity of the electrode towards glucose electrooxidation.

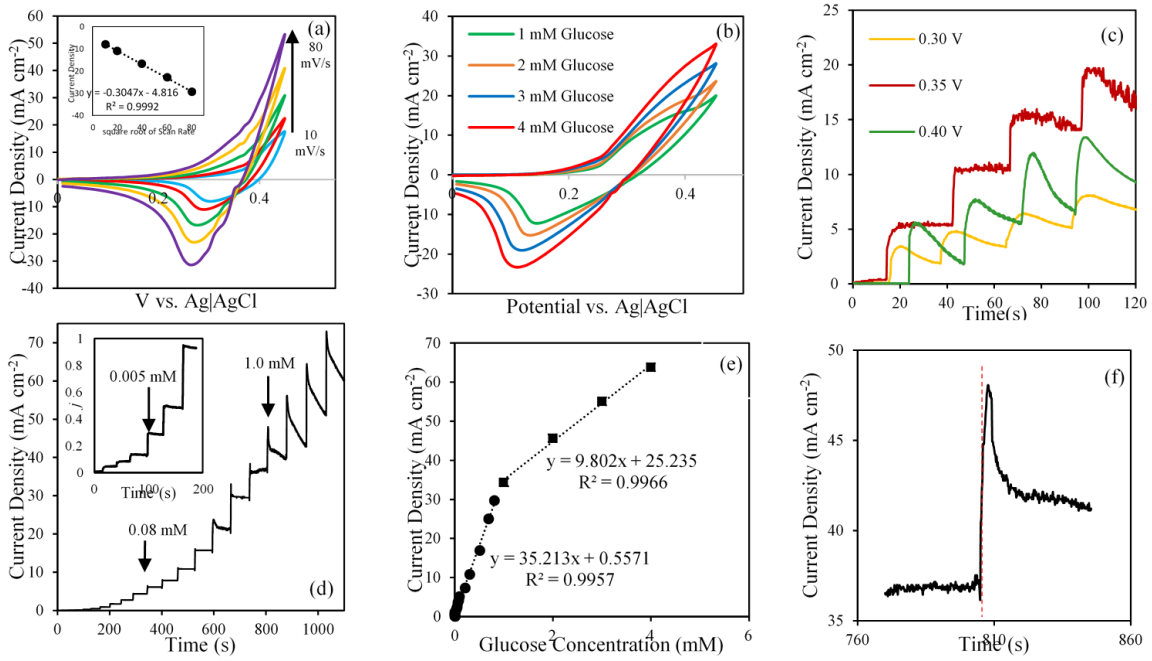

Figure 4. Electrocatalytic activity of hydrothermally prepared Ni_3Te_2. (a) CVs of the hydrothermally synthesized Ni_3Te_2 in 0.1 M KOH medium at various scan rates (10 to 80 mV s^{-1}). Inset shows cathodic peak currents of hydrothermally synthesized Ni_3Te_2-NF electrodes as a function of square root of scan rate. (b) CVs of the hydrothermally prepared Ni_3Te_2 electrode with glucose concentration increased from 1 to 4 mM. (c) Amperometric responses at different working potentials ranging from 0.30 to 0.40 V to successive addition of 0.1 mM glucose to 0.1 M KOH. (d) Amperometric response of the hydrothermally synthesized Ni_3Te_2 at 0.35 V to stepwise addition of different concentrations of glucose. Inset shows the zoomed in response of the electrode at lower glucose concentration. (e) corresponding calibration curve of response current density vs. glucose concentration. (f) The response time of the electrode to glucose oxidation.

The amperometric current response with addition of varying amounts of glucose was used to obtain the calibration curve as shown in Figure 4e, it was observed that there were two linear regions in the calibration curve, one at the lower glucose concentration (up to 0.8 mM) and the higher glucose concentration (1 - 4 mM). The linear fit in the low glucose concentration region (0.01 µM to 0.8 mM), showed an ultra-high sensitivity of 35.213 mA mM^{-1} cm^{-2} (R^2=0.9957). The LOD was as low as 0.38 µM, based on the signal/noise value of 3 (S/N = 3). The sensitivity in the higher glucose concentration from

1.0 mM to 4.0 mM was calculated to be 9.802 mA mM^{-1} cm^{-2} (R^2=0.9966). At higher glucose concentration, the amperometric current density gradually reaches to a saturation due to the presence of adsorbed reaction intermediates on the electrode surface covering the available active sites. This may lead to insufficient active sites to oxidize the incoming glucose on the electrode surface. Addition of glucose in the vicinity of the electrode produces a sharp increase in current density with a response time less than 4 s as can be seen in Figure 4f. Such low response time verifying the high catalytic activity of hydrothermally prepared Ni_3Te_2 towards glucose oxidation.

The reproducibility of the results as well as reliability of these measurements were tested by measuring the electrochemical response from several electrodes assembled from different batches of hydrothermally synthesized Ni_3Te_2. It was observed that the different electrodes showed an almost identical jump in current densities with the addition of same concentrations of glucose (0.1 mM) in 0.1 M KOH at 0.35 V vs. Ag|AgCl as shown in Figure 5a. Such identical current response between different electrodes and different addition events, confirmed the excellent stability and reproducibility of these electrodes.

One of the major challenges in non-enzymatic glucose sensing, as mentioned above, is to eliminate the interference from biomolecules coexisting in blood such as dopamine, ascorbic acid, urea, salts, fructose etc. In physiological conditions, the level of glucose is much higher than that of these interfering species (<0.5 mM).[64, 66] Hence, the selectivity of the hydrothermally synthesized Ni_3Te_2-NF electrode was determined towards glucose oxidation in presence of added interferent species by measuring the current response upon addition of 0.1 mM of glucose followed by successive additions of 0.01 mM of ascorbic acid, dopamine, lactose, fructose, sucrose, uric acid, KCl and

NaCl as shown in Figure 5b. It was found that the hydrothermally prepared Ni_3Te_2 electrode provides remarkable response only for glucose electrooxidation, while the addition of other species had a negligible effect on the anodic current.

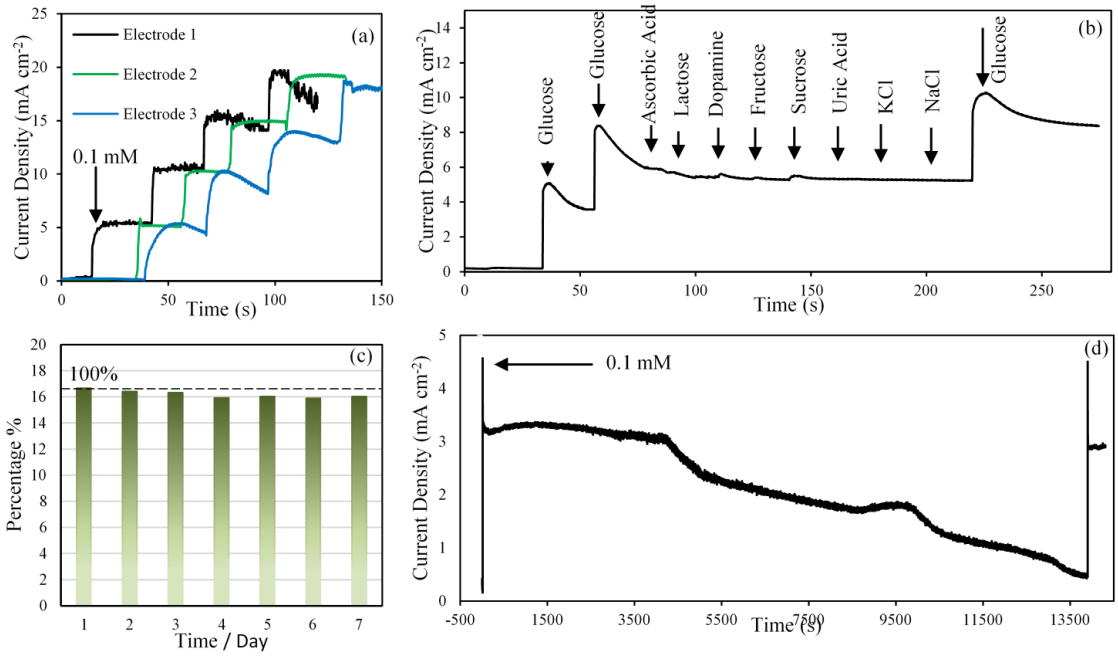

Figure 5. Selectivity and stability of hydrothermally synthesized Ni_3Te_2. (a) The amperometric response of different hydrothermally synthesized Ni_3Te_2-NF electrodes to stepwise addition of similar concentrations of glucose in an alkaline solution. (b) Amperometric response of the electrode to addition of glucose (0.1 mM) and other interfering species (0.01 mM) as mentioned in the diagram. (c) The extensive stability check of the Ni_3Te_2-NF electrode measured for 7 days. (d) Continuous chronoamperometric test to addition of identical concentrations of glucose as well as the complete oxidation time.

The long-term stability of this non-enzymatic sensor was also evaluated through amperometric response for specific concentration of glucose recorded for over a week (Figure 5c). The hydrothermally prepared Ni_3Te_2 electrode was stored in air when not in use and was reused for this study. The results indicate that the sensor retained more than

94% of its initial current response, suggesting the favorable long-term stability and reproducibility of this non-enzymatic glucose sensor.

In order to investigate the cyclability of the hydrothermally prepared Ni_3Te_2 electrode a chronoamperometry experiment was carried out where 0.1 mM glucose was injected to 0.1 M of KOH at 0.35 V and the oxidation current was allowed to decay down indicating full oxidation of the added glucose. This electrode needed almost five hours to convert all the added glucose to gluconolactone. 0.1 mM glucose solution was added again to this electrolyte which resulted in similar current density as the initial addition of glucose (Figure 5d) confirming data reliability and reproducibility for long term tests.

4.6. HUMAN BLOOD GLUCOSE DETERMINATION

To verify the possibility of the Ni_3Te_2 sensor in practical application, Ni_3Te_2-NF electrode was used to test the human blood glucose concentration. As provided in Table S1, Ni_3Te_2 sensor shows excellent performance towards glucose detection. First, the human blood samples obtained from three participating volunteers were tested with the commercially available glucometer (ReliOn). The electrochemical test was carried out by initially adding 100 μL of 1 mM glucose solution 2 times to the electrolyte in order to stabilize the system's current response. Then, 100 μL of the human blood sample was directly injected into the 0.05 M KOH followed by two more additions of 1 mM glucose. The current response for each of the standard glucose additions (i.e. 1 mM glucose solution) was recorded and plotted as a function of concentration producing a linear plot as shown in Figure S4.

The level of the glucose present in the blood sample was estimated from the linear fit of the plot (after subtracting the background glucose concentrations). [64] As shown in Table S1, the glucose concentration measured with Ni_3Te_2 based sensor, regardless of the fabrication method, was in good agreement with the results obtained from the commercial glucometer, confirming the possibility of Ni_3Te_2 as a promising sensor for human blood glucose testing.

Another growing emphasis for non-enzymatic glucose, especially with respect to continuous glucose monitoring system is to develop sensors that can detect very low amounts of glucose present in other bodily fluids such as sweat, urine, tears, tissue fluid etc. Detecting sudden jumps in glucose levels is also important to control diabetes. Hence, to demonstrate the capability of the Ni_3Te_2 electrode for testing low concentrations of glucose, such as those that might be present in tissue and other biological fluids, different solutions containing low concentrations of glucose were prepared, and the level of glucose was tested with a commercially available glucose biosensor. Then, the glucose solutions were added to our three-electrode system to measure the current responses.

As shown in Table S1, the results from both electrodeposited Ni_3Te_2 and hydrothermally synthesized Ni_3Te_2 were in good agreement with the results obtained from ReliOn glucometer. The relative standard deviation (RSD) below 3.5% verified the superior electrochemical performance of Ni_3Te_2 as a promising candidate for an effective glucose sensing platform.

Moreover, the possibility of detecting small changes in glucose level in a glucose enriched solution was tested. Figure 6a and Figure 6d shows the injection of 0.1, 1 and 5

µM of glucose to 0.1 M KOH and the corresponding changes in current density for electrodeposited Ni_3Te_2 as well as hydrothermally synthesized Ni_3Te_2, respectively. Then, 5mM of glucose was added to 0.1 M KOH solution to resemble the normal glucose level in blood. Figures 6b and figure 6c demonstrates the effect of injection of 5, 1 and 0.1 µM of glucose to this alkaline solution containing 5 mM glucose for electrodeposited and hydrothermally prepared Ni_3Te_2, respectively.

It should be noted here that small change in glucose level was detected reliably even in the presence of high glucose concentration. The difference between the current response measured from glucose addition to an alkaline medium with zero initial concentration of glucose and the injection of similar concentrations of glucose to an electrolyte containing 5 mM of glucose was compared in Figure 6c and Figure 6e. It can be concluded from these figures that, the standard deviation in detecting small glucose concentration reliably was small in the lower concentration range.

In the higher glucose concentration range, detecting accurate concentration of glucose was challenging due to the considerable background current generated by the presence of excess amount of glucose, which reduced the availability of the active sites for new analyte on the catalyst surface. However, Ni_3Te_2 electrode can successfully detect even minute amounts of increase in glucose concentration in a glucose-rich medium to a reliable extent. Such capabilities will be extremely useful to detect spikes in glucose concentrations under physiological conditions.

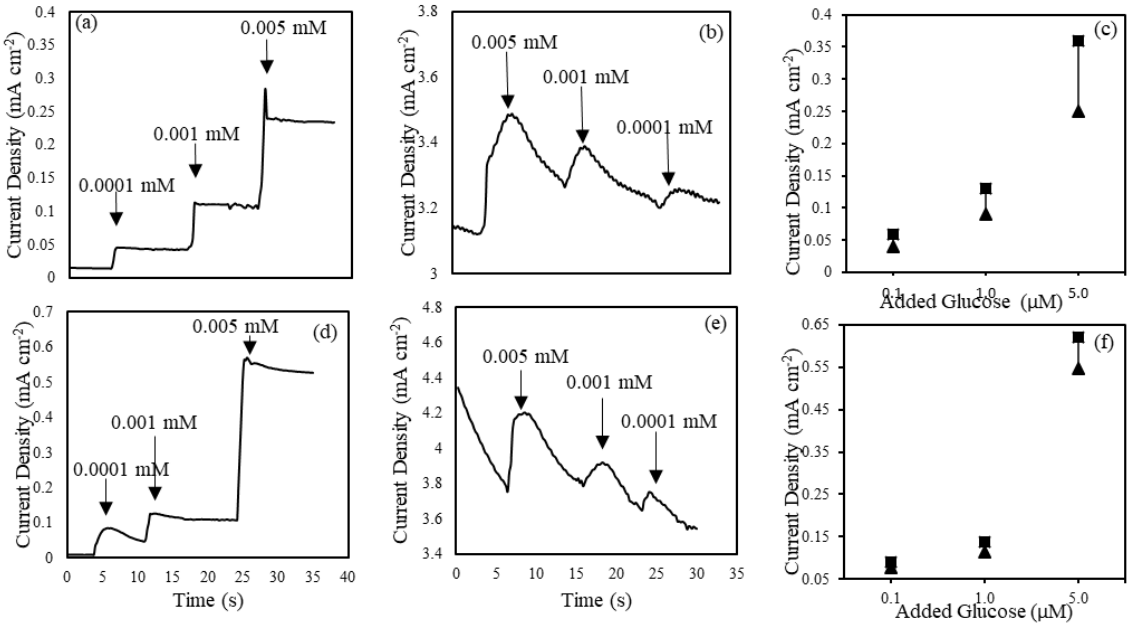

Figure 6. Sensitivity test of Ni_3Te_2-NF. (a) Successive addition of 0.1, 1 and 5 μM of glucose to 0.1 M KOH [using electrodeposited Ni_3Te_2]. (b) Reverse injections of 5, 1 and 0.1 μM of glucose to 0.1 M KOH solution containing 5 mM of glucose. (c) Difference between current densities measured for electrodeposited Ni_3Te_2-NF electrode. (d) Stepwise addition of low concentrations of glucose to 0.1 M KOH [using hydrothermally prepared Ni_3Te_2-NF electrode]. (e) Addition of low concentrations of glucose to 0.1 M KOH solution containing 5 mM of glucose. (f) The difference between current densities measured for hydrothermally synthesized Ni_3Te_2-NF electrode.

To the best of our knowledge, the functional parameters for this non-enzymatic sensor based on Ni_3Te_2 including sensitivity, LOD, and working potential are considerably better than the previously reported sensors as can be seen from the comparison Table S2. It can be concluded from this table that, the extremely low working potential along with ultrahigh sensitivity of Ni_3Te_2 validated our initial hypothesis that, replacing oxides and selenides with tellurides can lower the band gap, enhance redox activity of the Ni site, and consequently lowering the applied potential to 0.35 V vs. Ag|AgCl. From our previous research it was also observed that Ni_3Te_2 surface exhibited

favorable -OH adsorption kinetics on the Ni-site leading to catalyst activation at lower potential.[48] Since glucose oxidation follows catalyst activation and initiates at the *S*-OH site, (*S* = catalytically active transition metal ion), improved catalyst activation at low applied potential will have a positive influence on enhancing the glucose oxidation catalytic activity. The low working potential can overcome one of the biggest challenges associated with these non-enzymatic sensors which is the selectivity of the electrode towards glucose oxidation. This modest working potential will make Ni_3Te_2 an ideal candidate for smaller, economical and energy efficient glucometers.

5. CONCLUSION

In this study, two convenient electrochemical synthesis processes of electrodeposition and hydrothermal synthesis were employed to prepare Ni_3Te_2 nanostructures on Ni foam. The morphology, composition, and electrocatalytic performance of the binder-free electrodes were carefully characterized by various techniques. Both developed non-enzymatic sensors showed a superior catalytic activity towards the electrochemical oxidation of glucose. For electrodeposited Ni_3Te_2, an extremely high sensitivity of 41.615 mA cm^{-2} mM^{-1} with a low LOD of 0.43 µM in a range between 0.01 µM to 0.8 mM and 9.26 mA cm^{-2} mM^{-1} for the range of 1.0 mM to 4.0 mM was measured along with the other advantages associated with this electrode such as fast response, excellent selectivity and long- term stability and repeatability. The hydrothermally synthesized Ni_3Te_2 electrode also provides a high sensitivity of 35.213 mA cm^{-2} mM^{-1} from 0.01 µM to 0.8 mM with a LOD as low as 0.38 µM, and 9.802 mA

cm^{-2} mM^{-1} from 1 mM to 4 mM. Excellent selectivity, reproducibility of current response and long-term functional stability of this electrode verified the intrinsic properties of Ni_3Te_2 towards glucose sensing through direct electro-oxidation. It can be concluded that Ni_3Te_2 is a potential material for the development of enzyme-free sensor for reliable glucose determination.

ACKNOWLEDGMENT

The authors like to thank Materials Research Center for equipment usage.

REFERENCES

1. Qian, Q.; Hu, Q.; Li, L.; Shi, P.; Zhou, J.; Kong J.; Zhang, X.; Sun, G.; Huang, W.; Sensitive fiber microelectrode made of nickel hydroxide nanosheets embedded in highly-aligned carbon nanotube scaffold for nonenzymatic glucose determination, *Sensors and Actuators B*, 2018, *257*, 23–28.

2. Kim, S.; Lee, S.H.; Cho, M.; Lee, Y.; Solvent-assisted morphology confinement of a nickel sulfide nanostructure and its application for non-enzymatic glucose sensor, *Biosen. Bioelectron.*, 2016, *85*, 587–595.

3. Nichols, S.P.; Koh, A.; Storm, W.L.; Shin, J.H.; Schoenfisch, M.H.; Biocompatible materials for continuous glucose monitoring devices, *Chem. Rev.*, 2013, *113*, 2528.

4. Turner, A.P.F.; Biosensors: sense and sensibility, *Chem. Soc. Rev.*,2013, *42*, 3184–3196.

5. Tian, K.; Prestgard, M.; Tiwari, A; A review of recent advances in nonenzymatic glucose sensors, *Materials Science and Engineering C*, 2014, *41*, 100–118.

6. Bandodkar, A. J.; Wang, J; Non-invasive wearable electrochemical sensors: a review, *Trends in Biotechnology*, 2014, *32*, 7.

7. Hammock, M.L.; Chortos, A. Tee, B. C.-K.; Tok, J. B.-H.; Bao, Z.; The evolution of electronic skin (e-skin): a brief history, design considerations, and recent progress, *Adv. Mat.*, 2013, *25*, 5997–6038.

8. Windmiller, J.R.; Wang, J.; Wearable electrochemical sensors and biosensors: a review., *Electroanalysis*, 2013, *25*, 29–46.

9. Lankelma, J.; Nie, Z.; Carrilho, E.; Whitesides, G. M.; Paper-Based Analytical Device for Electrochemical Flow-Injection Analysis of Glucose in Urine, *Anal.Chem.*, 2012, *84* (9), 4147−4152.

10. Ye, D.; Liang, G.; Li, H.; Luo, J.; Zhang, S.; Chen, H.; Kong, J.; A novel nonenzymatic sensor based on CuO nanoneedle/graphene/carbon nanofiber modified electrode for probing glucose in saliva, *Talanta*, 2013, *116*, 223−230.

11. Moyer, J.; Wilson, D.; Finkelshtein, I.; Wong, B.; Potts, R.; Correlation between sweat glucose and blood glucose in subjects with diabetes, *Diabetes Technol. Ther.*, 2012, *14* (5), 398−402.

12. Wang, J.; Xu, L.; Lu, Y.; Sheng, K.; Liu, W.; Chen, C.; Li, Y.; Dong, B.; Song, H.; Engineered IrO_2@NiO Core−Shell Nanowires for Sensitive Nonenzymatic Detection of Trace Glucose in Saliva, *Anal. Chem.*, 2016, 88, 12346−12353.

13. Ramachandran, K.; Kumar, T. Raj; Justice Babu, K.; Gnana Kumar, G.; Ni-Co bimetal nanowires filled multiwalled carbon nanotubes for the highly sensitive and selective non-enzymatic glucose sensor applications, *Scientific Reports*, 2016, *6*, 36583.

14. Ronkainen, N.J.; Halsall, H.B.; Heineman, W.R.; Electrochemical biosensors, *Chem. Soc. Rev.*, 2012, *39*, 1747–1763.

15. Liu, S.; Ma, Y.; Cui, M.; Luo, X.; Enhanced electrochemical biosensing of alpha-fetoprotein based on three-dimensional macroporous conducting polymer polyaniline, *Sens. Actuators B: Chem.*, 2018, *225*, 2568–2574.

16. Bao, S.J.; Li, C.M.; Zang, J.F.; Cui, X.Q.; Qiao, Y.; Guo, J.; New nanostructured TiO_2 for direct electrochemistry and glucose sensor applications, *Adv Funct. Mater.*, 2008, *18*, 591–599.

17. Tee, S. Y.; Teng, C. P.; Ye, E.; Metal nanostructures for non-enzymatic glucose sensing, Materials Science and Engineering C, 2017, 70, 1018–1030.

18. Wang, G.; He, X.; Wang, L.; Gu, A.; Huang, Y.; Fang, B.; Geng, B.; Zhang, X.; Non-enzymatic electrochemical sensing of glucose, *Microchim Acta*, 2013, *180*,161–186.

19. Huang, W.; Cao, Y.; Chen, Y.; Peng, J.; Lai, X.; Tu, J.; Fast synthesis of porous $NiCo_2O_4$ hollow nanospheres for a high-sensitivity non-enzymatic glucose sensor, *Applied Surface Science*, 2017, 396, 804–811.

20. Rajendran, S.; Manoj, D.; Raju, K.; Dionysiou, D. D.; Naushad, M.; Gracia, F.; Cornejo, L.; Gracia-Pinilla, M.A.; Ahamad, T.; Influence of mesoporous defect induced mixed-valent $NiO(Ni^{2+}/Ni^{3+})$-TiO_2 nanocomposite for non-enzymatic glucose biosensors, *Sensors and Actuators B*, 2018, *264*, 27–37.

21. Benjamin, M.; Manoj, D.; Thenmozhi, K.; Bhagat, P.R.; Saravanakumar, D.; Senthilkumar, S.; A bioinspired ionic liquid tagged cobalt-salophen complex for nonenzymatic detection of glucose, *Biosens. Bioelectron*, 2017, *91*, 380–387.

22. Si, P.; Huang, Y.; Wang, T.; Ma, J.; Nanomaterials for electrochemical non-enzymatic glucose biosensors, *RSC Adv.*, 2013, *3*, 3487.

23. Tian, K.; Prestgard, M.; Tiwari, A.; A review of recent advances in non-enzymatic glucose sensors, *Materials Science and Engineering C*, 2014, *41*, 100118.

24. Toghill, K.E.; Compton, R.G.; Electrochemical Non-enzymatic Glucose Sensors: A Perspective and an Evaluation, *Int. J. Electrochem. Sci.*, 2010, *5*, 1246.

25. Zhu, Z.; Gancedo, L.G.; Flewitt, A.J.; Xie, H.; Moussy, F.; Milne, W.I.; A critical review of glucose biosensors based on carbon nanomaterials: carbon nanotubes and graphene, *Sensors*, 2012, *12*, 5996–6022.

26. Han, L.; Zhang, S.; Han, L.; Yang, D-P.; Hou, C.; Liu, A.; Porous gold cluster film prepared from Au@BSA microspheres for electrochemical nonenzymatic glucose sensor, *Electrochimica Acta*, 2014, 138, 109-114.

27. Fu, S.; Fan, G.; Yang, L.; Li, F.; Non-enzymatic glucose sensor based on Au nanoparticles decorated ternary Ni-Al layered double hydroxide/single-walled carbon nanotubes/graphene nanocomposite, *Electrochimica Acta*, 2015, 152, 146-154.

28. Shen, N.; Xu, H.; Zhao, W.; Zhao, Y.; Zhang, X.; Highly Responsive and Ultrasensitive Non-Enzymatic Electrochemical Glucose Sensor Based on Au Foam, *Sensors*, 2019, 19, 1203.

29. Shim, K.; Lee, W-C.; Park, M-S.; Shahabuddin, M.; Yamauchi, Y.; Hossain, S. A.; Shim, Y-B.; Kim, J. H.; Au decorated core-shell structured Au@Pt for the glucose oxidation reaction, *Sensors and Actuators B: Chemical*, 2019, 278, 88-96.

30. Shen, C.; Su, J.; Li, X.; Luo, J.; Yang, M.; Electrochemical sensing platform based on Pd–Au bimetallic cluster for non-enzymatic detection of glucose, *Sensors and Actuators B: Chemical*, 2015, 209, 695-700.

31. Lee, S.; Lee, J.; Park, S.; Boo, H.; Kim, H. C.; Chung, T. D.; Disposable non-enzymatic blood glucose sensing strip based on nanoporous platinum particles, *Applied Materials Today*, 2018, 10, 24-29.

32. Hoa, L. T.; Sun, K. G.; Hur, S. H.; Highly sensitive non-enzymatic glucose sensor based on Pt nanoparticle decorated graphene oxide hydrogel, *Sensors and Actuators B: Chemical*, 2015, 210, 618-623.

33. Wu, Y-S.; Wu, Z-W.; Lee, C-L.; Concave Pd core/ island Pt shell nanoparticles: Synthesis and their promising activities toward neutral glucose oxidation, *Sensors and Actuators B: Chemical*, 2019, 281, 1-7.

34. Ye, J-S.; Chen, C-W.; Lee, C-L.; Pd nanocube as non-enzymatic glucose sensor, *Sensors and Actuators B: Chemical*, 2015, 208, 569-574.

35. Wang, L.; Lu, X.; Wen, C.; Xie, Y.; Miao, L.; Chen, S.; Li, H.; Li, P.; Song, Y.; One-step synthesis of Pt–NiO nanoplate array/reduced graphene oxide nanocomposites for nonenzymatic glucose sensing, *J. Mater. Chem.*, 2015, *3*, 608–616.

36. Madhu, R.; Veeramani, V.; Chen, S.M.; Manikandan, A.; Lo, A.Y.; Chueh, Y.L.; Honeycomb-like porous carbon-cobalt oxide nanocomposite for high-performance enzyme-less glucose sensor and supercapacitor applications, *ACS Appl. Mater. Interfaces*, 2015, *7*, 15812–15820,

37. Xiea, F.; Liub, T., Xieb, L.; Sunb, X.; Luo, Y.; Metallic nickel nitride nanosheet: An efficient catalyst electrode for sensitive and selective non-enzymatic glucose sensing, *Sensors and Actuators B*, 2018, *255*, 2794–2799.

38. Fang, Y.; Li, C.; Bo, J.; Henzie, J.; Yamauchi, Y.; Asahi, T.; Chiral sensing with mesoporous Pd@Pt nanoparticles, *Chem. Electro Chem.*, 2017, *4*, 1832–1835.

39. Hsu, C.; Lin, J.; Hsu, D.; Wang, S.; Lin, S.; Hsueh, T.; Enhanced non-enzymatic glucose biosensor of ZnO nanowires via decorated Pt nanoparticles and illuminated with UV/green light emitting diodes, *Sens. Actuators B*, 2017, *238*, 150–159.

40. Tekbasoglu, T.; Soganci, T.; Ak, M.; Koca, A.; Sener, M.K.; Enhancing biosensor properties of conducting polymers via copolymerization: synthesis of EDOT-substituted bis(2-pyridylimino) isoindolato-palladium complex and electrochemical sensing of glucose by its copolymerized film, *Biosens.Bioelectron*, 2017, *87*, 81–88.

41. He, G.; Tian, L.; Cai, Y.; Wu, S.; Su, Y.; Yan, H.; Pu, W.; Zhang, J.; Li, L.; Sensitive Nonenzymatic Electrochemical Glucose Detection Based on Hollow Porous NiO, *Nanoscale Research Letters*, 2018, *13*, 3.

42. Wang, L.; Ye, Y.; Shen, Y.; Wang, F.; Lu, X.; Xie, Y.; Chen, S.; Tan, H.; Xu, F.; Song, Y.; Hierarchical nanocomposites of Co3O4/polyaniline nanowire arrays/reduced graphene oxide sheets for amino acid detection, *Sens. Actuators B: Chem.*, 2014, *203*, 864–872.

43. Liu, T.; Lib, M.; Dong, P.; Zhang, Y.; Zhou, M.; Designing and synthesizing various nickel nitride (Ni_3N) nanosheets dispersed carbon nanomaterials with different structures and porosities as the high-efficiency non-enzymatic sensors, *Sensors and Actuators B*, 2018, *260*, 962–975.

44. Chen, C.; Shi, M.; Xue, M.; Hu, Y.; Synthesis of nickel (II) coordination polymers and conversion into porous NiO nanorods with excellent electrocatalytic performance for glucose detection, *Rsc Adv.*, 2017, *7*, 22208-22214.

45. Toghill K.E.; Xiao L.; Phillips M.A.; Compton R.G.; The non-enzymatic determination of glucose using an electrolytically fabricated nickel microparticle modified boron-doped diamond electrode or nickel foil electrode, *Sens Actuator B: Chem*, 2010, *147*, 642.

46. Garcia-Garcia, F.J.; Salazar, P.; Yubero, F.; González-Elipe, A.R.; Non-enzymatic Glucose electrochemical sensor made of porous NiO thin films prepared by reactive magnetron sputtering at oblique angles, *Electrochimica Acta*, 2016, *201*, 38–44.

47. Safavi, A.; Maleki, N.; Farjami, E.; Fabrication of a glucose sensor based on a novel nanocomposite electrode, *Biosensors and Bioelectronics*, 2009, *24*, 1655–1660.

48. De Silva, U.; Masud, J.; Zhang, N.; Hong, Y.; Liyanage, W. P. R.; Asle Zaeem, M.; Nath, M.; Nickel telluride as a bifunctional electrocatalyst for efficient water splitting in alkaline medium, *J. Mater. Chem. A*, 2018,*6*, 7608-7622.

49. Amin, B. G.; Swesi, A. T.; Masud, J.; Nath, M.; $CoNi_2Se_4$ as an efficient bifunctional electrocatalyst for overall water splitting, *Chem. Commun.*, 2017,*53*, 5412-5415.

50. Masud, J.; Liyanage, W. P. R.; Cao, X.; Saxena A.; Nath, M.; Copper selenides as high-efficiency electrocatalysts for oxygen evolution reaction, *ACS Appl. Energy Mater.*, 2018, *1*, 4075−4083.

51. Swesi, A. T.; Masud, J.; Liyanage, W. R.P.; Umapathi, S.; Bohannan, E.; Medvedeva, J.; Nath, M.; textured $NiSe_2$ film: bifunctional electrocatalyst for full water splitting at remarkably low overpotential with high energy efficiency, *Scientific Reports*, 2017, 7, 2401.

52. Shen, L.; Wang, J.; Xu, G.; Li, H.; Dou, H.; Zhang, X.; $NiCo_2S_4$ nanosheets grown on nitrogen-doped carbon foams as an advanced electrode for supercapacitors, *Adv. Energy Mater*. 2015, *5*, 1400977.

53. Wang, S.; Li, W.; Xin, L.; Wu, M.; Long, Y.; Huang, H.; Lou, X.; Facile synthesis of truncated cube-like $NiSe_2$ single crystals for high-performance asymmetric supercapacitors, *Chemical Engineering Journal*, 2017, *330*, 15, 1334-1341.

54. Shamsipur, M.; Najafi M.; Hosseini M.R.; Highly improved electrooxidation of glucose at a nickel (II) oxide/multi-walled carbon nanotube modified glassy carbon electrode, *Bioelectrochemistry*, 2010, *77*, 120–124.

55. Mani, S.; Ramaraj, S.; Chen, S.-M.; Dinesh, B.; Chen, T.-W.; Two-dimensional metal chalcogenides analogous $NiSe_2$ nanosheets and its efficient electrocatalytic performance towards glucose sensing, *Journal of Colloid and Interface Science*, 2017, *507*, 378–385.

56. Li, G.; Huo, H.; Xu, C.; $Ni_{0.31}Co_{0.69}S_2$ nanoparticles uniformly anchored on a porous reduced graphene oxide framework for a high-performance non-enzymatic glucose sensor, *J. Mater. Chem. A*, 2015,*3*, 4922-4930.

57. Liu, J.; Lv, W.; Wei, W.; Zhang, C.; Li, Z.; Li, B.; Kang, F.; Yang, Q.-H.; A three-dimensional graphene skeleton as a fast electron and ion transport network for electrochemical applications, *J. Mater. Chem. A*, 2014, *2*, 3031–3037.

58. Zhan, B., Liu, C.; Chen, H.; Shi, H.; Wang, L.; Chen, P.; Huang, W.; Dong, X.; Free-standing electrochemical electrode based on Ni $(OH)_2$/3D graphene foam for nonenzymatic glucose detection, Nanoscale, 2014, *6*, 7424–7429.

59. Erikson, D.; Oncescu, V.; High volumetric power density, non-enzymatic, glucose fuel cells, *Scientific Reports*, 2013, 3, 1226.

60. Kerzenmacher, S.; Ducrée, J.; Zengerlea, R.; Stetten, F.von; Energy harvesting by implantable abiotically catalyzed glucose fuel cells, *Journal of Power Sources*, 2008, 182, 1–17.

61. Su, C.-H.; Sun, C.-L.; Peng, S.-Y.; Wu, J.-J.; Huang, Y.-H.; Liao, Y.-C.; High performance non-enzymatic graphene-based glucose fuel cell operated under moderate temperatures and a neutral solution, Journal of the Taiwan Institute of Chemical Engineers, 2018, 6, 57.

62. Zhao, Y.; Fan, L.; Gao, D.; Ren, J.; Hong, B.; High-power non-enzymatic glucose biofuel cells based on three-dimensional platinum nanoclusters immobilized on multiwalled carbon nanotubes, *Electrochimica Acta*, 2014, 145, 159–169.

63. Zhang, L.; Ding, Y.; Li, R.; Ye, C.; Zhao, G.; Wang, Y.; Ni-Based metal–organic framework derived Ni@C nanosheets on a Ni foam substrate as a supersensitive non-enzymatic glucose sensor, J. Mater. Chem. B, 2017,5, 5549-5555.

64. Amin G. B.; Masud, J.; Nath, M.; Non-enzymatic glucose sensor based on $CoNi_2Se_4$ /rGO nanocomposite with Ultrahigh sensitivity at low working potential, *J. Mater. Chem. B,* 2019, 7, 2338–2348.

65. Tian, K.; Prestgard, M.; Tiwari, A.; A review of recent advances in nonenzymatic glucose sensors, *Materials Science and Engineering C*, 2014, *41*, 100–118.

66. Niu, X.; Lan, M.; Zhao, H.; Chen, C.; Highly Sensitive and Selective Nonenzymatic Detection of Glucose Using Three-Dimensional Porous Nickel Nanostructures, *Anal. Chem.*, 2013, *85*, 3561−3569.

SUPPORTING INFORMATION

ULTRA-SENSITIVE AND HIGHLY SELECTIVE Ni_3Te_2 AS A NON-ENZYMATIC GLUCOSE SENSOR AT EXTREMELY LOW WORKING POTENTIAL

Bahareh Golrokh Amin, Umanga De Silva, Manashi Nath

Department of Chemistry, Missouri University of Science and Technology

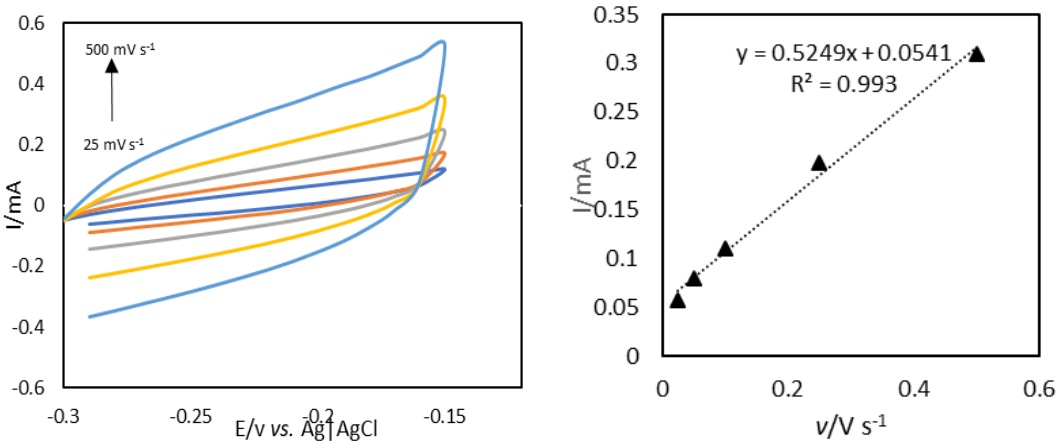

Figure S1. ECSA for electrodeposited Ni_3Te_2.

ECSA was measured using the formula, ECSA = C_{dl}/C_s, where Cs is the specific capacitance of the sample or the capacitance of an atomically smooth planar surface of the material per unit area under identical electrolyte conditions (for this article Cs = 0.04 mF cm^{-2} in 0.1M KOH was used). The ECSA was estimated to be 13 cm^{-2}.

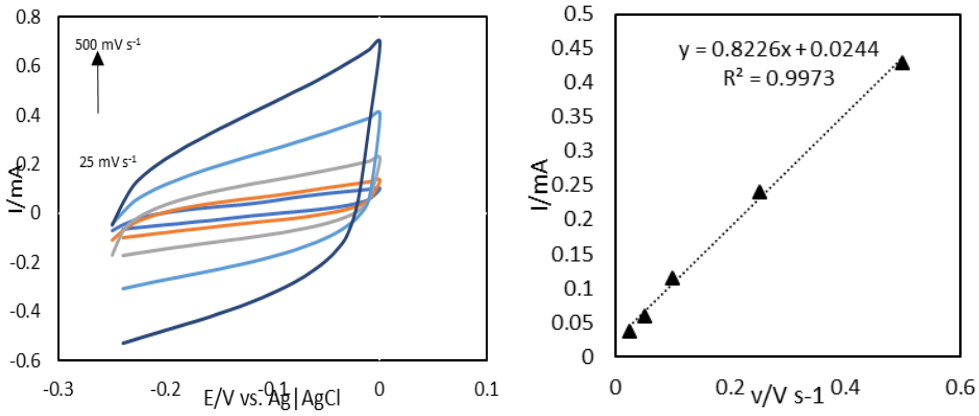

Figure S2. ECSA for Hydrothermal Ni_3Te_2.

ECSA was measured using the formula, ECSA = C_{dl} /C_s, where Cs is the specific capacitance of the sample or the capacitance of an atomically smooth planar surface of the material per unit area under identical electrolyte conditions (for this article C_s = 0.04 mF cm^{-2} in 0.1M KOH was used). The ECSA was estimated to be 20.2 cm^{-2}.

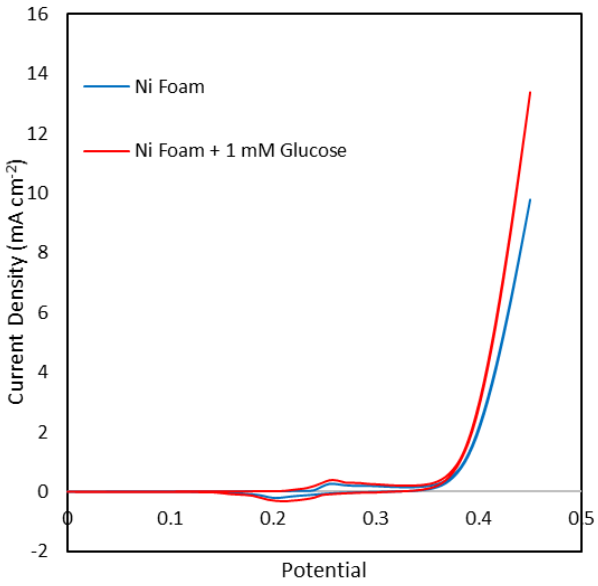

Figure S3. Cyclic Voltammetry of Ni Foam in absence and presence of glucose.

Table S1. Concentration of glucose of different samples measured by commercially available glucometer and as prepared Ni_3Te_2 electrodes.

Sample	Glucometer (mg/dL)	Ni_3Te_2(ED) (mM)	RSD (%, n=3)	Ni_3Te_2(Hy) (mM)	RSD (%, n=3)
1	24 (1.33mM)	1.38	1.67	1.31	1.34
2	31 (1.72mM)	1.84	1.59	1.79	1.40
3	49 (2.72mM)	2.77	2.43	2.44	2.74
4	63 (3.49mM)	3.62	2.64	3.13	3.15
5	76 (4.21mM)	4.33	2.53	4.04	3.48
Blood 1	98 (5.43 mM)	5.5	2.41	5.44	2.62
Blood 2	106 (5.88 mM)	5.92	2.54	5.90	2.13
Blood 3	110 (6.10 mM)	6.13	3.12	6.11	3.75

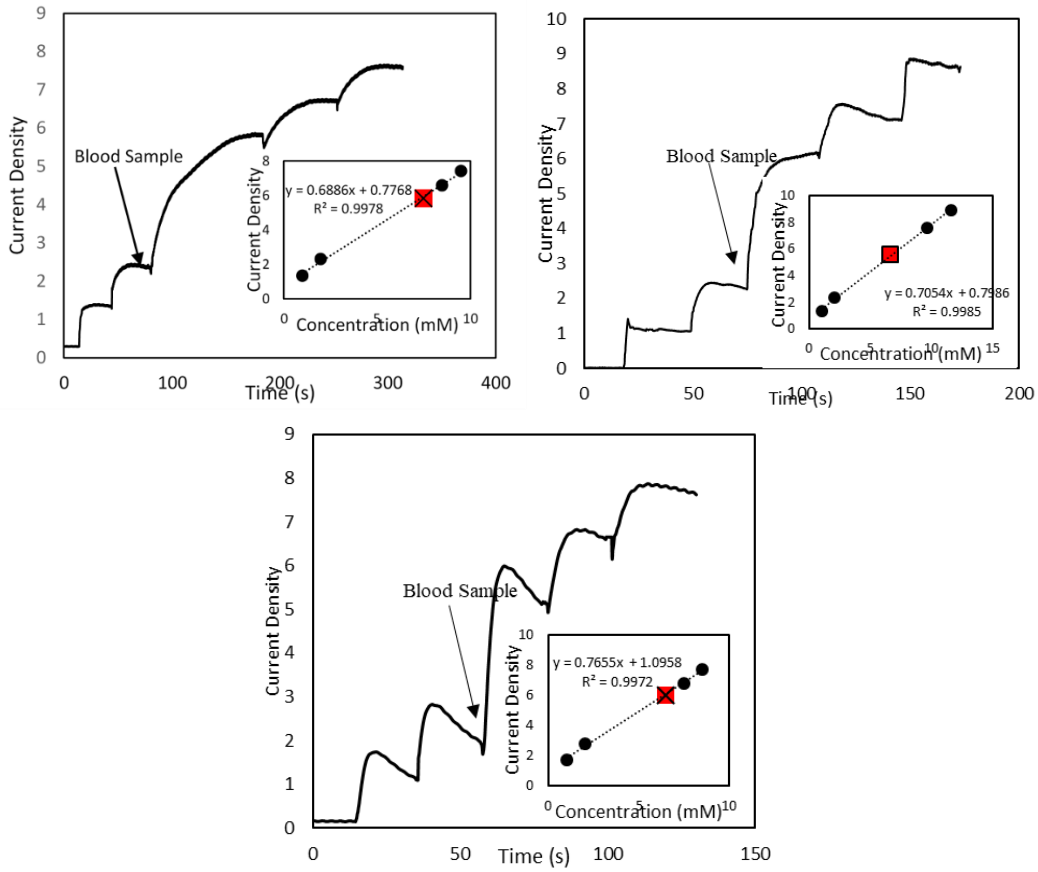

Figure S4. Plot of randomly selected test to measure the blood glucose level.

Table S2. Comparison of the Ni_3Te_2 electrode with other reported non-enzymatic

Electrode	Applied potential	Sensitivity ($mA\ mM^{-1}\ cm^{-2}$)	Linear range	LOD (μM)	Ref.
Electrodeposited Ni_3Te_2	0.35 V	41.615	0.01 μM –0.8 mM	0.43	This work
		9.26	1 mM – 4 mM		
Hydrothermal Ni_3Te_2	0.35 V	35.213	0.01 μM –0.8 mM	0.38	This work
		9.802	1.0 mM – 4 mM		
$CoNi_2Se_4$-rGO@NF	0.35 V	**18.89**	1 μM–4.0 mM	0.65	1
NiO-GR/GCE	0.35 V	0.016	0.02–4.5 mM	5.0	2
Electrodeposited $NiCo_2O_4$	0.4 V	0.0067	5 – 65 μM	0.38	3
$Ni(OH)_2$ nanosheets	0.46 V	**12.2**	20 μM –10.5 mM	0.645	4
CuO NWA/CF	0.5 V	**32.33**	0.10 mM–0.50 mM	0.02	5
NiO/C microspheres	0.5 V	**30.19**	2 lM–1.279 mM	2.0	6
Cu_2Se SPs/CF	0.5 V	**18.66**	0. 25 μM –0.237 mM	0.25	7
3D Co_3O_4/Ni	0.5 V	**13.855**	0.04−3.6 mM	1.0	8
Ni^{3+}-rich surface electrode	0.5 V	**11.36**	0.001–1 mM	0.9	9
		3.58	2–4 mM		
3D porous Ni networks	0.5 V	2.90	5 μM−4 mM	0.07	10
$NiCo_2O_4$/3DGF	0.5 V	2.524	Up to 80 mM	0.38	11
Ni–Co NSs/rGO	0.5 V	1.774	10 μM – 2.65 mM	3.79	12
3D porous Ni	0.5 V	2.9	0.5 μM to 4 mM	0.07	13
$Ni_{0.31}Co_{0.69}S_2$/rGO	0.5 V	1.753	1 mM to 5 mM	0.078	14
		0.955	5–16 mM		
NiO-MWCNTs	0.5 V	1.696	1 μM–200 μM	0.011	15
NiO/NCS	0.53 V	0.219	2 μM–600 μM	0.31	16
		0.0878	800 μM–2.5mM		
NiO nanosheets	-	0.8381	5 μM –2.31mM	0.145	17
CuNi/C Nanosheet	0.54 V	**17.12**	0.2 μM –2.72 mM	0.066	18
Ni_3S_2/MWCNT	0.54 V	3.345	30–500 μM	1.0	19
Ni_3S_2/Ni foam	0.55 V	**16.46**	0.0005–3 mM	0.82	20
3D Ni_3S_2/Ni foam	0.55 V	6.148	0.005–3.0 mM	1.2	21
$Ni(OH)_2$/3D	0.55 V	2.65	1 μM – 1.17 mM	0.34	22
Cu@porous carbon	0.55 V	10.1	1μM−6.0 mM	0.60	23
3D NiO hollow sphere/rGO	0.58 V	2.04	9 μM–1.129 mM	0.82	24
Ni $(OH)_2$ nanostructure modified rGO	0.6 V	11.4	0.01–30 mM	15.0	25
3-D $Ni_3(VO4)_2$ Nanosheet	0.62 V	**19.83**	2.5–150 μM	0.57	26
CuS/RGO/CuS/Cu	0.65 V	**22.67**	0.001–0.655 mM	0.50	27

REFERENCES

1. Amin, B.G.; Masud, J.; Nath, M.; *J. Mater. Chem. B*, 2019, 7, 2338--2348.

2. Zhu, X.; Jiao, Q.; Zhang, C.; Zuo, X.; Xiao, X.; Liang, Y.; Nan, J.; Amperometric nonenzymatic determination of glucose based on a glassy carbon electrode modified with nickel (II) oxides and graphene, *Microchim. Acta*, 2013, *180*, 477-483.

3. Naik, K. K.; Kumar, S.; Rout, C. S.; Electrodeposited spinel $NiCo_2O_4$ nanosheet arrays for glucose sensing application, *RSC Adv.*, 2015, *5*, 74585-74591.

4. Qian, Q.; Hu, Q.; Li, L.; Shi, P.; Zhou, J.; Kong, J.; Zhang, X.; Sun, G.; Huang, W.; Sensitive fiber microelectrode made of nickel hydroxide nanosheets embedded in highly-aligned carbon nanotube scaffold for nonenzymatic glucose determination, *Sensors and Actuators B*, 2018, *257*, 23–28.

5. Liua, X.; Yanga, W.; Chena, L.; Jiaa, J.; Three-Dimensional Copper foam supported CuO nanowire arrays: an efficient non-enzymatic glucose sensor, *Electrochimica Acta*, 2017, *235*, 519–526.

6. Cui, Z.; Yin, H.; Nie, Q.; Controllable preparation of hierarchically core–shell structure NiO/C microspheres for non-enzymatic glucose sensor, *Journal of Alloys and Compounds*, 2015, *632*, 402–407.

7. Zhu, W.; Wang, J.; Zhang, W.; Hu, N.; Wang, J.; Huang, L.; Wang, R.; Suo, Y.; Wang, J.; Monolithic copper selenide submicron particulate film/copper foam anode catalyst for ultrasensitive electrochemical glucose sensing in human blood serum, *J. Mater. Chem. B*, 2018, *6*, 718-724

8. Xu, H.; Xia, C.; Wang, S.; Han, F.; Akbari, M. K.; Hai, Z.; Zhuiykov, S.; Electrochemical non-enzymatic glucose sensor based on hierarchical 3D Co_3O_4/Ni heterostructure electrode for pushing sensitivity boundary to a new limit, *Sensors and Actuators B*, 2018, *267*, 93–103.

9. Wang, X.; Jian, H.; Xiao, Q.; Huang, S.; Ammonium nickel phosphate on nickel foam with a Ni^{3+}-rich surface for ultrasensitive nonenzymatic glucose sensors, *Applied Surface Science*, 2018, *459*, 40–47.

10. Niu, X.; Lan, M.; Zhao, H.; Chen, C.; Highly Sensitive and Selective Nonenzymatic Detection of Glucose Using Three-Dimensional Porous Nickel Nanostructures, *Anal. Chem.*, 2013, *85*, 3561−3569.

11. Wu, M.; Meng, S.; Wang, Q.; Si, W.; Huang, W.; Dong, X.; Nickel–Cobalt Oxide Decorated Three-Dimensional Graphene as an Enzyme Mimic for Glucose and Calcium Detection, *ACS Appl. Mater. Interfaces*, 2015, *7*, 21089–21094.

12. L. Wang, X. Lu, Y. Ye, L. Sun and Y. Song, *Electrochim. Acta*, 2013, 114, 484–493

13. Niu, X.; Lan, M.; Zhao, H.; Chen, C.; Highly Sensitive and Selective Nonenzymatic Detection of Glucose Using Three-Dimensional Porous Nickel Nanostructures, *Anal. Chem.*, 2013, *85*, 3561−3569.

14. Li, G.; Huo, H.; Xu, C.; $Ni_{0.31}Co_{0.69}S_2$ nanoparticles uniformly anchored on a porous reduced graphene oxide framework for a high-performance non-enzymatic glucose sensor, *J. Mater. Chem. A*, 2015, *3*, 4922–4930.

15. Prasad, R.; Bhat, B. R.; Multi-wall carbon nanotube–NiO nanoparticle composite as enzyme-free electrochemical glucose sensor, *Sensors and Actuators B*, 2015, *220*, 81–90.

16. Zhu, J.; Yin, H.; Gong, J.; Al-Furjan, M.S.H.; Nie Q.; In situ growth of Ni/NiO on N-doped carbon spheres with excellent electrocatalytic performance for non-enzymatic glucose detection, *Journal of Alloys and Compounds*, 2018, *748*, 145-153.

17. Guo, M.; Wei, L.; Qu, Y.; Zeng, F.; Yuan, C.*;* One-step electrochemical exfoliation of nanoparticles-assembled NiO nanosheets for non-enzymatic glucose biosensor, *Materials Letters*, 2018, 213, 174–177.

18. (18) Zhang, L.; Ye, C.; Li, X.; Ding Y.; Liang H.; Zhao, G.; Wang, Y.; A CuNi/C Nanosheet Array Based on a Metal–Organic Framework Derivate as a Supersensitive Non-Enzymatic Glucose Sensor, *Nano-Micro Lett.*, 2018, *10*, 28.

19. Lin, T.-W.; Liu, C.-J.; Dai, C.-S.; Ni_3S_2/carbon nanotube nanocomposite as electrode material for hydrogen evolution reaction in alkaline electrolyte and enzyme-free glucose detection *Appl. Catal. B*, 2014, 154– 155, 213–220.

20. Kim, S.; Lee, S. H.; Cho, M.; Lee, Y.; Solvent-assisted morphology confinement of a nickel sulfide nanostructure and its application for non-enzymatic glucose sensor, *Biosensors and Bioelectronics*, 2016, *85*, 587–595.

21. Huo, H.; Zhao, Y.; Xu, C.; 3D Ni_3S_2 nanosheet arrays supported on Ni foam for high-performance supercapacitor and non-enzymatic glucose detection, *J. Mater. Chem. A*, 2014, *2*, 15111-15117.

22. Zhan, B.; Liu, C.; Chen, H.; Shi, H.; Wang, L.; Chen, P, Huang, W.; Dong, X.; Free-standing electrochemical electrode based on $Ni(OH)_2$/3D graphene foam for nonenzymatic glucose detection, *Nanoscale*, 2014,*6*, 7424-7429.

23. Zhanga, X.; Luo, J, Tang, P.; Morante, J.R.; Arbiol, J.; Xue, C.; Li, Q.; Fransaer, J.; Ultrasensitive binder-free glucose sensors based on the pyrolysis of in situ grown Cu MOF, *Sensors and Actuators B*, 2018, *254*, 272–281.

24. Huang, W.; Ding, S.; Chen, Y.; Hao, W.; Lai, X.; Peng, J.; Tu, J.; Cao, Y.; Li, X.; 3D NiO hollow sphere/reduced graphene oxide composite for high performance glucose biosensor, *Scientific Reports*, 2017, *7*, 5220.

25. Subramanian, P.; Niedziolka-Jonsson, J.; Lesniewski, A.; Wang, Q.; Li, M.; Boukherroub, R.; Szunerits, S.; Preparation of reduced graphene oxide–$Ni(OH)_2$ composites by electrophoretic deposition: application for non-enzymatic glucose sensing, *J. Mater. Chem. A*, 2014, *2*, 5525–5533.

26. Kumar, R.; Bhuvana, T.; Rai, P.; Sharma, A.; Highly Sensitive Non-Enzymatic Glucose Detection Using 3-D $Ni_3(VO_4)_2$ Nanosheet Arrays Directly Grown on Ni Foam, *Journal of The Electrochemical Society*, 2018, *165* (2), B1-B8.

27. Zhao, C.; Wu, X.; Zhang, X.; Li, P.; Qian, X.; Facile synthesis of layered CuS/RGO/CuS nanocomposite on Cu foam for ultrasensitive nonenzymatic detection of glucose, *Journal of Electroanalytical Chemistry*, 2017, *785*, 172–179.

IV. FACILE ONE-POT SYNTHESIS OF $NiCo_2Se_4$/RGO ON NI FOAM FOR HIGH PERFORMANCE HYBRID SUPERCAPACITOR

Bahareh Golrokh Amin, Jahangir Masud, and Manashi Nath

Department of Chemistry, Missouri University of Science and Technology, Rolla, MO 65409

ABSTRACT

A facile, innovative synthesis for fabrication of $NiCo_2Se_4$/rGO on Ni foam nanocomposite via simple hydrothermal reaction is proposed. The as-prepared $NiCo_2Se_4$/rGO@Ni foam electrode was tested through XRD, TEM, SEM, and EDS to characterize the morphology and the purity of the material. The bimetallic electrode exhibited outstanding electrochemical performance with high specific capacitance of 2038.55 F g^{-1} at 1 A g^{-1}. $NiCo_2Se_4$/rGO@Ni foam exhibit a satisfying cycling stability after 1000 cycles by retaining 90% of its initial capacity. A superior energy density of 67.01 W h kg^{-1} along with high power density of 903.61 W $kg^{-}1$ further improved the high performance of this electrode towards hybrid supercapacitor. The excellent electrochemical performance of the $NiCo_2Se_4$/rGO@Ni foam can be explained through the high electrocatalytic activity of $NiCo_2Se_4$ in combination with reduced graphene oxide which increases the conductivity and surface area of the electrode. This study proved that $NiCo_2Se_4$/rGO@Ni foam can be utilized as a high energy density-high power density electrode in energy storage applications.

1. INTRODUCTION

The rapidly-increasing global demand for an alternative, renewable energy system encouraged researchers to explore for high-performance energy storage technologies to store the energy harnessed from the eco-friendly sources.[1-4] Numerous endeavors were made to elevate the performance of the dominating energy storage technology, namely, the batteries, particularly Li-ion batteries which has shown significant progress over the last several decades.[5,6] However, regardless of the high energy density that batteries can provide, they are still not fulfilling all our energy storage demands since they are suffering from low power density, slow charge-discharge rate, and limited cycle life. Gradual degradation of the batteries in storing and delivering energy throughout their lifetime can be attributed to their deficiency in undergoing a fully reversible redox reaction in a charge-discharge process.[7-10]

Electrochemical supercapacitors have been introduced to bridge the gap between electrolytic capacitors (with high power density and low energy density) and rechargeable batteries (with high energy density and low power density). Supercapacitors are known as one the most promising energy storage devices owing to their high specific capacitance, promising power density, short charge-discharge time, longer lifespan, and being safer to use compared to batteries.[11-14] Contrary to Li-ion battery technology, supercapacitors, operate over wider temperature ranges due to the simpler electrochemical mechanism of storing charge. This results in lower thermo-chemical heat, consequently, making these safer devices to store energy.[5] The supercapacitors can be classified in three categories based on the charge storage mechanism and use of active

electrode materials: (i) electrochemical double layer capacitor (EDLC) which stores charge in highly porous or high surface area electrodes such as carbon-based materials including graphene, CNTs etc.[15-17] (ii) Pseudocapacitors, also known as redox supercapacitors, which stores charge through reversible electrochemical redox reactions using the variable oxidation states of transition metal based centers in the corresponding oxides [18-21], hydroxides [21-24], chalcogenides [25-28] as electrode materials. (iii) Hybrid electrochemical capacitor which are the combination of both EDLCs and pseudocapacitors and incorporate redox-active transition metal-based centers onto high surface area, porous electrodes.[29-32]

EDLCs store charge electrostatically via generation of the electrical double layer in the non-faradaic region at the interface between the electrode and the electrolyte. Hence, without diffusion limitations, the response to changes in potential is fast and leads to high power density.[29] Recently, graphene, a two-dimensional sheet of hexagonally bonded network of carbon atoms, has been used as the electrode material for EDLCs due to its extraordinary electrical and thermal properties along the basal plane.[33,34] However, due to the low specific capacitance of EDLCs, they are unable to replace Li-ion batteries, as they cannot provide the energy density necessary for practical applications.[33,35] On the other hand, reversible electrochemical redox reactions occurring within the inner surface of the electroactive materials or at the electrode-electrolyte interface is the primary charge storage mechanism of a pseudocapacitor.[36,37]

The overall performance of the supercapacitors can be further boosted by combining the non-faradaic process of EDLCs with the faradaic process of pseudocapacitors thereby leading to hybrid supercapacitors. The hybrid supercapacitor

shows higher capacitance with improved energy and power density than either EDLCs or pseudocapacitors.[38-41] As mentioned above, the electrochemical performance of supercapacitors is mainly related to the electrode materials and their properties. Therefore, extensive research has been done to fabricate new electrode composites to serve in energy storage applications.

Recently, transition metal-based compounds have been widely investigated in several electrochemical applications such as full water splitting [42-45], non-enzymatic glucose sensing, [46,47] and supercapacitors [48-50] due to their abundance, cost-effectiveness, good electrical conductivity and more importantly excellent electrocatalytic activity. Very recently, transition metal chalcogenides (TMCs), in particular, selenide-based compounds have been extensively investigated as potential electrocatalysts in energy conversion devices, wherein, their electrocatalytic performance was significantly improved owing to the tunable redox properties of the active transition metal reaction center. Moreover, the small bandgap and high degree of covalency of the selenide-based compounds enhances charge transport properties which promotes better electrical conductivity, making them significantly better electrocatalysts compared to their respective oxide counterparts.[46,51,52]

Among several types of TMC Ni-Co-based selenides are favorable as pseudocapacitor electrode materials, due to their desirable electrochemical activity in alkaline electrolytes arising from the tunability of the Ni^{2+}/Ni^{3+} and Co^{2+}/Co^{3+} redox potential by varying cation coordination and doping. The spinel structure of $NiCo_2Se_4$ with several catalytically active sites of nickel (Ni^{3+}) occupying the octahedral sites, and cobalt (Co^{3+} and Co^{2+}) distributed over both octahedral and tetrahedral sites, offers

numerous pathways for possible charge transport, increasing the surface area exposed to the solution and reducing the transport path length.[53-55]

The high surface area along with improved electrical conductivity and good electrochemical stability of the reduced graphene oxide (rGO) in combination with TMCs on a conductive substrate can further enhance the supercapacitive property of the nanocomposite. Therefore, in this article we have reported for the first time the supercapacitor performance of $NiCo_2Se_4$@rGO on Ni foam synthesized by a one-step hydrothermal method. The $NiCo_2Se_4$@rGO on Ni foam electrode showed high specific capacitance of 2038.55 F g^{-1} at 1 A g^{-1} with excellent energy density of 67.01 W h kg^{-1} and power density of 903.61 W kg^{-1} and good cycling stability that retains 90% of its maximum capacity after 1000 cycles.

2. EXPERIMENTAL

2.1. PREPARATION OF THE NI FOAM SUBSTRATE

Prior to deposition, the Ni foam substrate was immersed into a solution of diluted HCl and was sonicated for 15 minutes. Then, the Ni foam was rinsed with deionized (DI) water several times and dried in an oven under 60 ºC for 10 minutes.

2.2. PREPARATION OF GRAPHENE OXIDE (GO)

Graphene oxide (GO) Graphene oxide (GO) was first prepared by a modified Hummers' method using natural graphite, following procedure that has been reported in detail in our previous publication.[46]

2.3. SYNTHESIS OF $NiCo_2Se_4$/RGO @Ni FOAM

$NiSO_4$ was obtained from Alfa Aesar, $CoSO_4$ was purchased from Mallinckrodt, and SeO_2 was purchased from Acros Organics. All chemicals were of analytical grade and used directly without further purification. Scheme 1 shows the synthesis process of $NiCo_2Se_4$/rGO via one-step hydrothermal method of growing material directly on the Ni foam surface without the need of a binder. First, 10 mM $NiSO_4$ along with 25 mM of $CoSO_4$ and 45 mM of SeO_2 were dissolved and mixed in a solution of ethanol (2 ml) and DI water (8 ml) under vigorous stirring to form a homogeneous solution. Then, 0.05 g of freshly prepared graphene oxide was added to the mixture and stirred for 15 minutes. Afterwards, hydrazine hydrate (5 drops) was added to the solution, and pre-cleaned Ni foam was placed inside the vial and stirred for about 30 minutes. Later, the mixture along with the Ni foam was transferred into a Teflon-lined stainless-steel autoclave and heated in an oven at 145 ºC for 8 h. The autoclave then was naturally cooled down to the room temperature overnight. The prepared electrode ($NiCo_2Se_4$-rGO@NF) was rinsed several times with DI water, and then dried at 60 ºC for about 12 h. Finally, the ingrown $NiCo_2Se_4$-rGO on the surface of Ni foam electrode was subjected to thermal annealing in the presence of rapid flow of N_2 gas in a closed flask at 300 ºC for 2 minutes.

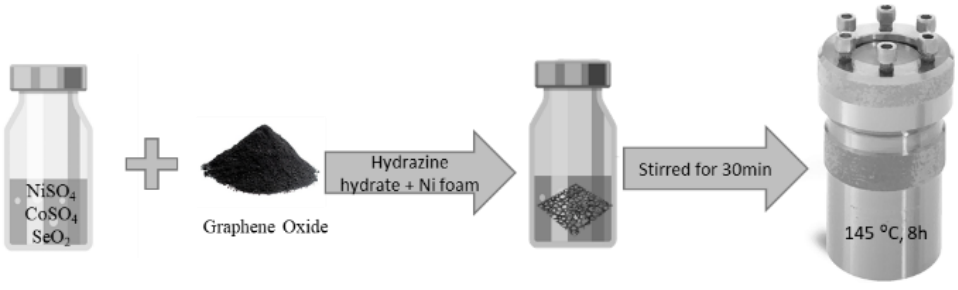

Scheme 1. Preparation of $NiCo_2Se_4$/rGO @Ni foam.

2.4. MATERIALS CHARACTERIZATION

2.4.1. Powder X-ray Diffraction. The hydrothermally synthesized product was characterized using a Philips X-Pert X-ray diffractometer (PANalytical, Almelo, The Netherlands) with CuKa (1.5418 A) radiation.

2.4.2. Scanning Electron Microscopy (SEM). The SEM image of the electrode surfaces was obtained using a FEI Helios NanoLab 600 FIB/FESEM at an acceleration voltage of 10 kV and a working distance of 4.5 mm. Energy dispersive spectroscopy (EDS) was also obtained from the SEM microscope.

2.4.3. Transmission Electron Microscopy (TEM). High resolution TEM (HRTEM) images and selected area electron diffraction (SAED) patterns of $NiCo_2Se_4$ and $NiCo_2Se_4$/rGO powders were obtained using a FEI Tecnai F20. The probe current is 1.2 nA with a spot size of less than 2 nm. STEM mode in the TEM was also used for dark field imaging where the convergence angle was 13 mrad with a camera length of 30 mm.

2.5. ELECTROCHEMICAL MEASUREMENTS

The electrochemical measurements, including electrochemical impedance spectroscopy (EIS), cyclic voltammetry (CV), and galvanostatic charge–discharge was measured using an IviumStat potentiostat. All the electrochemical measurements were performed at 25 ºC in 1 M KOH aqueous solution with different current densities of 1, 2, 3, 5, 6, 8 and 10 A g-1.

The specific capacitance of the electrode was calculated from the galvanostatic discharge curves according to the following equation: (eqn. 1)) [5,14,19]

$$C = \frac{I\Delta t}{m\Delta V} \quad (1)$$

where *I* is the discharge current, Δt is the time for a full discharge, ΔV stands for the potential window, m is the mass loading of the active material on the electrode and C is the specific capacitance (F g^{-1}). The energy density (E) and power density (P) were calculated based on the following equations (eqn. 2 eqn. 3): [13,56]

$$E = \frac{1}{2} C(\Delta V)^2 \times \frac{1000}{3600} \quad (2)$$

$$P = \frac{E}{\Delta t} \quad (3)$$

where *C* is the capacitance (F g^{-1}), ΔV is the potential window (V), and Δt is the discharge time (s).

3. RESULTS AND DISCUSSION

The The crystalline phase of the $NiCo_2Se_4$-rGO powder was characterized using powder X-ray diffraction (pxrd) technique. As shown in Figure 1(a), the pxrd pattern confirmed the formation of pure crystalline structure of the $NiCo_2Se_4$-rGO] where the diffraction peaks matched well with the reported standard pattern (PDF No. 04-006-5241). The chemical composition of as-synthesized $NiCo_2Se_4$ powder without rGO was also analyzed and has been provided in the supplementary information. As shown in Figure S1, ESI†, all the diffraction peaks taken from the as-prepared powder can be indexed to the standard PDF card (PDF No. 04-006-5241). Similarity of the pxrd patterns of $NiCo_2Se_4$ powder with and without rGO indicated that the presence of rGO did not have any significant impact on formation of the crystalline phase of the material. TEM analysis confirmed the nanostructure morphology of $NiCo_2Se_4$-rGO and $NiCo_2Se_4$ as has been shown in Figure 1 (b) and S2 (a), respectively. It can be seen that the $NiCo_2Se_4$

particles were randomly distributed on rGO surface (Figure 1(b)). On the other hand, rGO-free $NiCo_2Se_4$ showed agglomeration of nanoparticles with the smooth surfaces (Figure S2). Selected area electron diffraction (SAED) patterns were performed to confirm the crystallinity of catalyst and has been shown in Figures 1 (c) and S2 (b). SAED pattern obtained from $NiCo_2Se_4$/rGO could be indexed to the (111), (311), and (020) planes (Figure 1c) and similarly, (111) and (311) planes were observed for $NiCo_2Se_4$ catalyst (Figure S2b). The surface composition and morphology of the $NiCo_2Se_4$/rGO@NF and $NiCo_2Se_4$ were tested using energy dispersed X-ray spectroscopy (EDS) and scanning electron microscopy (SEM). Figure 1 (d) shows the EDS result for $NiCo_2Se_4$/rGO@NF which confirmed that the electrode was indeed composed of Ni, Co, and Se with an approximate elemental ratio of 1:2:4 for Ni:Co:Se. Similar EDS results were obtained for $NiCo_2Se_4$ synthesized in absence of rGO as shown in Figure S3, ESI†. SEM images were collected on the $NiCo_2Se_4$@Ni foam and $NiCo_2Se_4$-rGO@Ni foam to study the surface morphology of these electrodes as well to investigate the effect of adding rGO on the morphology. Figure S4, ESI† shows the uniform growth of $NiCo_2Se_4$ directly on the Ni foam. As can be seen from this image, the morphology of the film was granular comprised of ill-defined nanostructures. Interestingly it was observed that adding GO to the reaction mixture led to a dramatic change on the product morphology. Figure 1 (e) and Figure 1 (f) shows typical SEM images at low and high magnification of the $NiCo_2Se_4$-rGO@NF electrode, respectively. As can be observed from these images, addition of rGO led to the formation of petal-like nanostructures vertically arranged on the Ni foam. Such thin plate-like structures are expected to have extremely high accessible surface area, large exposure of the transition

metal active sites as well as availability of edges which can show low charge transfer resistance. Such attributes are extremely beneficial for charge storage applications. The change in morphology can be possibly explained by the hypothesis that in the presence of rGO, the growing $NiCo_2Se_4$ nuclei adheres itself to the rGO sheet, followed by controlled growth of the nuclei along the preferred lattice directions. The petal shaped structure of $NiCo_2Se_4$-rGO directly grown on the Ni foam provides high surface area for this composite which can also enhance permeation of the electrolyte ion.

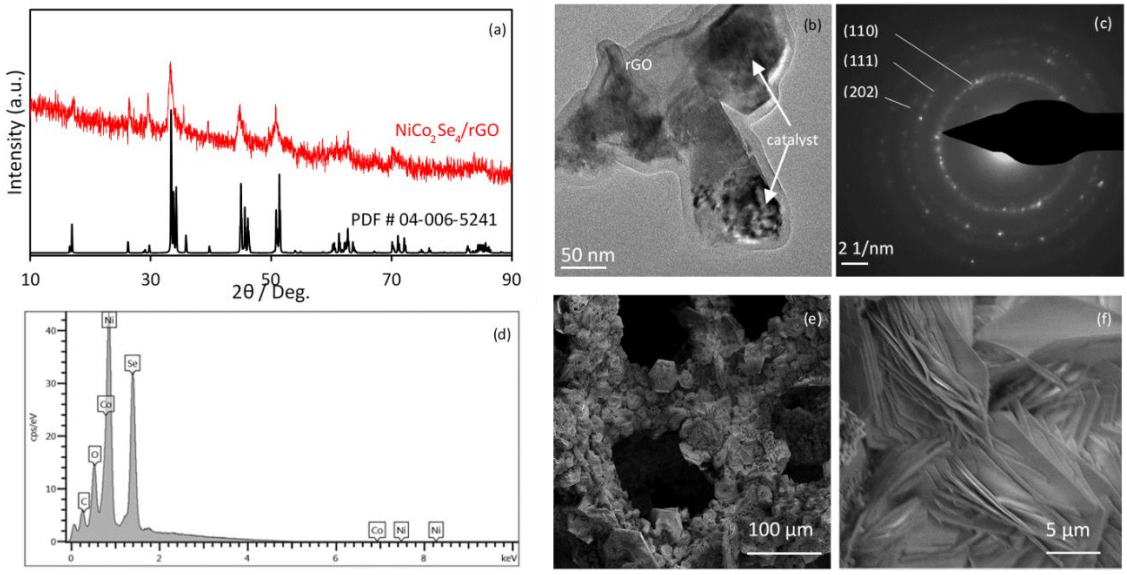

Figure 1. Characterization techniques for $NiCo_2Se_4$-rGO. (a) XRD pattern of $NiCo_2Se_4$/rGO@NF (b) TEM image of $NiCo_2Se_4$/rGO@NF (c) selected area electron diffraction (SAED) pattern of $NiCo_2Se_4$/rGO@NF (d) EDS microanalysis of the hybrid electrode (e) Low magnification SEM image of $NiCo_2Se_4$/rGO on Ni foam (f) High magnified SEM image of $NiCo_2Se_4$/rGO on Ni foam substrate.

The electrochemical performance of the $NiCo_2Se_4$-rGO@NF electrode was examined using cyclic voltammetry (CV) and galvanostatic charge – discharge cycles in

a freshly prepared 1 M KOH aqueous solution. In Figure 2(a) the near rectangular CV curve of rGO on Ni foam in the potential range of 0 – 0.6 V *vs*. Ag|AgCl is typical of EDLC charge storage mechanism as could be expected from porous conducting carbonaceous matrix.[15-17] With Ni Co_2Se_4 on the other hand, the distinctive redox peak in the potential range of 0 - 0.5 V vs. Ag|AgCl verified the electrochemical pseudocapacitor-like behavior for this compound. The CV curve of $NiCo_2Se_4$-rGO@NF as shown in Figure 2(a) clearly shows a pair of oxidation and reduction peaks, illustrating the electrochemical behavior of the electrodes resulting from pseudocapacitive charge storage in conjunction with EDLC behavior which led to a wider potential range of -0.2 – 0.5 V *vs*. Ag|AgCl for electrochemical activity. The larger integral area of the $NiCo_2Se_4$-rGO@NF from the CV curve verified the larger specific capacitance for this compound compared to those of rGO and $NiCo_2Se_4$@NF electrodes. The charge storage of $NiCo_2Se_4$-rGO@NF can be attributed to the redox reaction between Ni^{2+}/Ni^{3+}, Co^{3+}/Co^{4+}, and Co^{2+}/Co^{3+}.[57,58] $NiCo_2Se_4$ crystallizes in a spinel structure type where divalent Ni occupies the tetradehral sites whereas, trivalent Co occupies the vacancy ordered octahedral layers. However, scrambling of the metal ions between the octahedral and tetrahedral sites has been observed quite frequently in these spinel compounds leading to presence of mixed oxidation states such as Ni^{2+}/Ni^{3+} and Co^{2+}/Co^{3+}. Hence, the co-existence of Ni and Co in $NiCo_2Se_4$ provides richer redox-active reaction sites available on the surface of the electrode composite for electrolyte ions to be adsorbed and desorbed reversibly. Figure 4 (b) indicates the CV curves of the $NiCo_2Se_4$-rGO@NF within the potential window of -0.2 to 0.5 V at different scan rates ranging from 10 - 80 mV s^{-1}. With increasing the scan rate, position of the oxidation and reduction peaks were

changed. The anodic peaks shifted towards more positive potentials while the cathodic peaks moved to negative potentials, confirming the pseudocapacitance behavior of the electrode. It is worth mentioning that, $NiCo_2Se_4$-rGO@NF exhibited excellent reversibility and rate performance as there was no noticeable distortion in the shape of the redox peak with increase of the scan rates.[59] Figure S5, ESI† shows the relationship between the oxidation and reduction peak currents as a function of the scan rate indicating a linear dependence of anodic and cathodic peak currents on the scan rate.

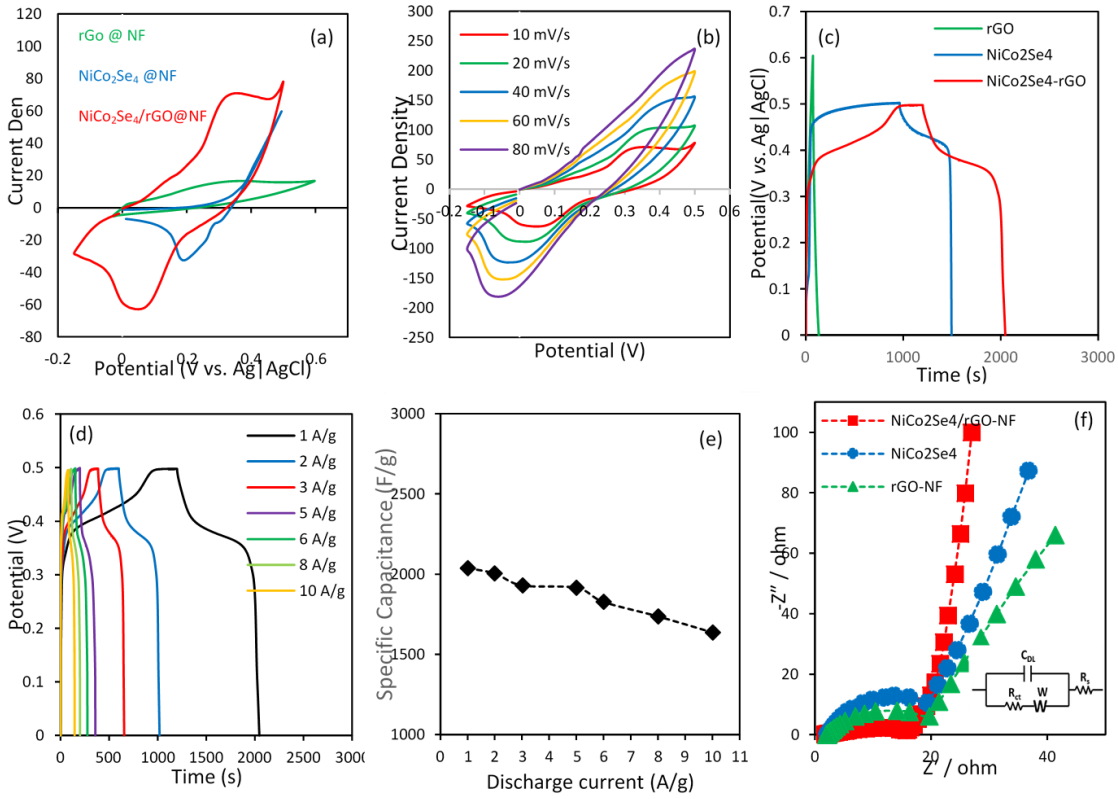

Figure 2. Energy storage performance of $NiCo_2Se_4$-rGO. (a) Cyclic voltammograms of rGO@NF, $NiCo_2Se_4$@NF and $NiCo_2Se_4$/rGO@NF at a scan rate of 10 mV s^{-1} (b) CV plot of $NiCo_2Se_4$/rGO@NF at different scan rates ranging from 10 – 80 mV s^{-1} (c) Galvanostatic charge – discharge curves at 1 A g^{-1} (d) Galvanostatic charge – discharge curve of $NiCo_2Se_4$/rGO@NF at different current densities (e) Specific capacitance at different current densities (f) Nyquist plot showing the imaginary part vs. real part of impedance.

Figure 2 (c) displays the galvanostatic charge – discharge curve of $NiCo_2Se_4$-rGO@NF, $NiCo_2Se_4$@NF and rGO@NF electrodes at the current density of 1 A g^{-1}. The triangle shaped charge – discharge curve of rGO@NF is characteristic of a typical EDLC behavior attributable to the small mass transfer resistance and good charge mobility on the rGO@NF electrode composite. The nature of the galvanostatic discharge curve for rGO@NF agrees well with the results obtained from the CV verifying a non-faradic reaction of storing charge in the potential range from 0 – 0.6 V.

The galvanostatic discharge curves corresponding to $NiCo_2Se_4$-rGO@NF and $NiCo_2Se_4$@NF, on the other hand, demonstrated a normal pseudocapacitive behavior as it showed a decrease in potential until reaching a plateau at 0.4 V and 0.45 V for $NiCo_2Se_4$-rGO@NF and $NiCo_2Se_4$@NF, respectively, then the potential showed a slow decay until it reached 0.0 V. The galvanostatic discharge curves of $NiCo_2Se_4$-rGO@NF and $NiCo_2Se_4$@NF were compatible with the result obtained from the CV curves which is based upon faradaic redox reaction at the electrode/electrolyte interface within the same potential window. The symmetrical shapes of galvanostatic charge - discharge curves of $NiCo_2Se_4$-rGO@NF indicates its superior chemical reversibility during the charge – discharge process. In order to evaluate the feasibility of $NiCo_2Se_4$-rGO@NF as a hybrid supercapacitor, charge – discharge measurements were performed at different current densities from 1 to 10 A g^{-1} in the potential range of 0 – 0.5 V *vs*. Ag|AgCl (Figure 2(d)). The specific capacitance (C_{sp}) which indicates the electro-sorption rate and capacity of the $NiCo_2Se_4$-rGO@NF was calculated from the galvanostatic charge – discharge measurements based on eqn. 1. As shown in Figure 2(e), $NiCo_2Se_4$-rGO@NF yields high specific capacitance of 2038.55, 2004.8, 1930.12, 1915.66, 1827.18, 1737.06, and

1636.62 F g^{-1} at current densities of 1, 2, 3, 5, 6, 8, and 10 A g^{-1}, respectively. The higher specific capacitance at low current densities can be attributed to the complete adsorption and desorption of the hydroxyl groups from the electrolyte to the inner and outer surface of the electrode composite thereby leading to higher charge transfer. At high current densities, on the other hand, the ions at the outer surface of the electrode are mostly responsible for the charge storage process as the electrolyte has limited access to the inner pores. Accordingly, the specific capacity decreases gradually with increasing the applied current density.[60,61]

As shown in Table 1, a significantly higher charge storage capacity of $NiCo_2Se_4$-rGO@NF (2038.55 F g^{-1} at 1.0 A g^{-1}) was achieved compared to that of the $NiCo_2Se_4$ @NF (1477.6 F g^{-1}) and rGO @NF (238.88 F g^{-1}). The high catalytic performance of this electrode as a supercapacitor can be further explained by the larger space between lattice structure of the $NiCo_2Se_4$ due to the elongation between layers. This can facilitate the electron transport in the structure.[5,11]

Table 1. Comparison between specific capacitance and potential windows of rGO, $NiCo_2Se_4$, and $NiCo_2Se_4$/rGO@NF.

Sample	Potential window (V)	Specific Capacitance (F g^{-1})
rGO	0.0 – 0.6	238.8
$NiCo_2Se_4$	0.0 – 0.5	1477.6
$NiCo_2Se_4$ / rGO	0.0 – 0.5	2038.55

The electrochemical performance of active electrode materials was evaluated further by electrochemical impedance spectroscopy (EIS) over the frequency range of 0.1

Hz–100 kHz, in a 1 M KOH electrolyte for $NiCo_2Se_4$-rGO@NF, $NiCo_2Se_4$@NF and rGO@NF to provide kinetic and mechanistic information of the electroactive materials, the charge transfer rate as well as the adsorption/desorption rate of hydroxyl ion on the electrode/electrolyte interface. The charge transfer resistance (R_{ct}) was measured from the EIS plot in the high frequency region as shown in Figure 2f. It was observed that the R_{ct} values as well as the circular arc for $NiCo_2Se_4$-rGO@NF was smaller than $NiCo_2Se_4$@NF and rGO@NF composite electrodes, indicating faster kinetics for charge transfer at the electrode-electrolyte interface. Such favorable charge transfer results in higher impingement of surface hydroxyl ions leading to higher capacitance. The lower frequency region of the EIS plots illustrates the diffusive resistance of the composite electrodes which influences the mobility of charge carriers within the electrode composite. As can be seen from Figure 2(f), the R_s value which is an indication of ionic resistance of the electrolyte, the inner resistance of the electrode material, and the resistance between the current collector and the electrode for $NiCo_2Se_4$-rGO@NF composite shows lower resistance. $NiCo_2Se_4$@NF on the other hand, shows higher film resistance highlighting the effect on addition of rGO to the composite electrode in enhancing conductivity of the electrode composite.

Stability under several charge-discharge cycles is another key performance metrics for the practical applications of supercapacitors. Figure 3(a) shows the behavior of $NiCo_2Se_4$-rGO@NF composite electrode under several repetitive charge-discharge cycles at 5 $A.g^{-1}$. It was observed that $NiCo_2Se_4$-rGO@NF was able to maintain around 90% of its initial specific capacitance after 1000 charge/discharge cycles of stability check.

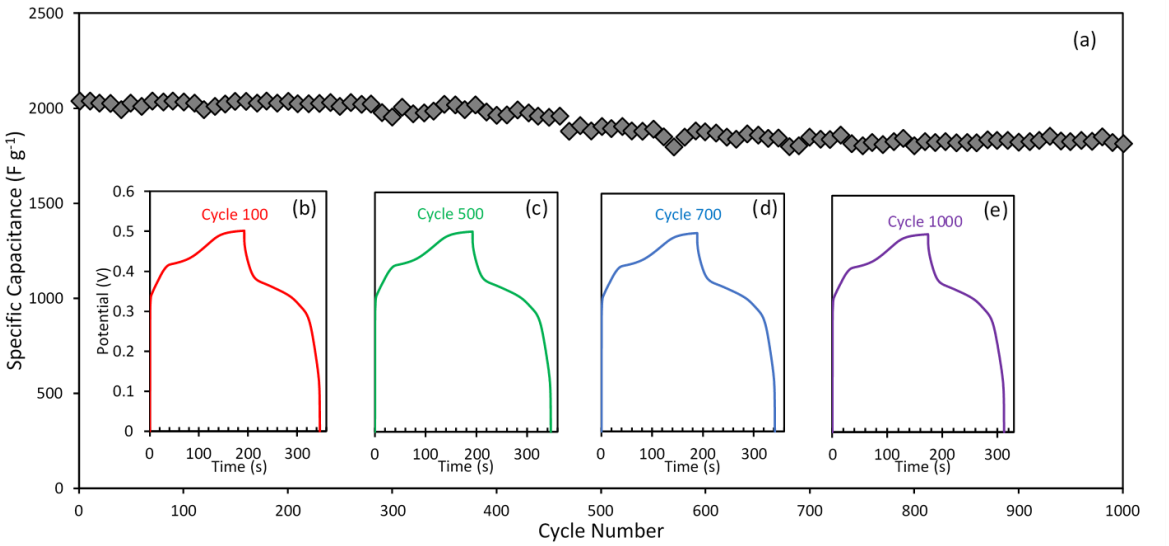

Figure 3. Cycling stability of $NiCo_2Se_4$-rGO@NF. (a) Specific capacitance vs. cycle number at a current density of 5 A g^{-1} for stability check (b) Galvanostatic charge – discharge plot of the cycle number 100 (c) Cycle 500 (d) cycle number 700 and (e) 1000th charge – discharge curve.

The high stability of the $NiCo_2Se_4$-rGO@NF can be attributed to the higher active surface area and facile charge transport caused by the interactions between $NiCo_2Se_4$ and rGO in this nanocomposite which preserves the capacitance during the charge and release of ions. First 100 cycles for the $NiCo_2Se_4$-rGO decorated on the Ni foam substrate within the potential range of 0 to 0.5 V at a current density of 5.0 A g^{-1} exhibited a symmetrical shape with almost similar discharge time without much disparity from the first cycle, which indicates a highly reversible and sustainable of charge storage process . Cycle 100 shown in Figure 3(b) exhibit a specific capacitance of 2032.89F g^{-1}, Cycle 500 (Figure 3(c)) revealed C_{sp} of 1903.94 F g^{-1}, 1847.88 F g^{-1} was measured for cycle 700 (Figure 3(c)), and cycle 1000 displayed in Figure 3(d) a specific capacitance of 1814.63 F g^{-1}.

To examine the possibility of $NiCo_2Se_4$-rGO@NF as a flexible electrode for hybrid supercapacitor, the electrochemical characteristics of the as-prepared $NiCo_2Se_4$-rGO@NF electrode was estimated as a function of catalyst deformation by measuring the galvanostatic charge – discharge curves under three different bending angles of 180º, 90º, 20º shown in Figure 4(a). Figure 4(b), (c) and (d) present photographic images of the normal and bending position of the $NiCo_2Se_4$-rGO@NF electrode. As shown in the galvanostatic curves, identical charge–discharge time and behavior were observed for hybrid electrode under normal and bending conditions. This indicates that contorted $NiCo_2Se_4$-rGO@NF electrode retained its mechanical stability as a flexible energy storage device for practical applications.

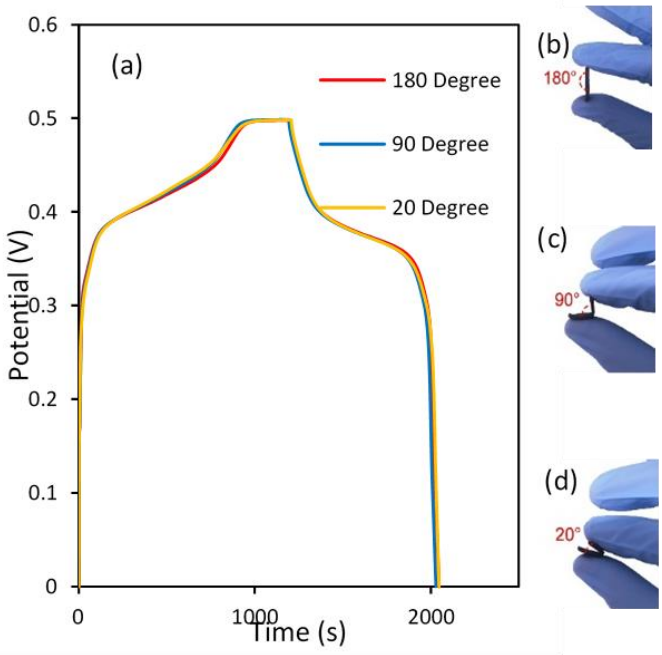

Figure 4. Mechanical stability check for $NiCo_2Se_4$-rGO. (a) Galvanostatic charge – discharge curve of normal and bending position of $NiCo_2Se_4$/rGO on Ni foam in 1 M KOH (b) photographic image of $NiCo_2Se_4$/rGO@NF electrode under normal position of 180º, (c) 90º deformation (d) 20º bending position.

4. CONCLUSION

$NiCo_2Se_4$-rGO@NF was synthesized through a simple one-pot hydrothermal process. The merits of using $NiCo_2Se_4$-rGO on Ni foam were as follows: first, the petal-like nanostructured morphology can provide a high specific surface area, resulting in enhanced electroactive sites for electrochemical storage. The correlation between the morphology of the electrode and the performance of the energy storage system has also been reported in other studies.[62] Also, The $NiCo_2Se_4$-rGO@NF electroactive material possess higher conductivity than $NiCo_2Se_4$@NF and rGO@NF, which can facilitate a pathway for electron transport. Furthermore, the $NiCo_2Se_4$-rGO@NF electrode depicts a high specific capacitance value of 2038.55 F g^{-1} at a current density of 1 A g^{-1}. The superior energy density of 67.01 Wh kg^{-1}, high power density of 903.61 W kg^{-1} along with an excellent mechanical stability at different bending conditions, and great stability after 1000 cycles of $NiCo_2Se_4$-rGO@NF makes it a promising candidate in the future of energy storage technology.

REFERENCES

1. Y. Tang, S. Chen, S. Mu, T. Chen, Y. Qiao, S. Yu, and F. Gao, *ACS Appl. Mater. Interfaces*, 2016, 8, 9721–9732.

2. J. Chang, Z. Gao, X. Wang, D. Wu, F. Xu, X. Wang, Y. Guo, and K. Jiang, *Electrochim. Acta*, 2015, 157, 290–298.

3. Y. Wen, S. Peng, Z. Wang, J. Hao, T. Qin, S. Lu, J. Zhang, D. He, X. Fan, and G. Cao, *J. Mater. Chem. A*, 2017, 5, 7144–7152.

4. S. Zheng, X. Li, B. Yan, Q. Hu, Y. Xu, X. Xiao, H. Xue, and H. Pang, *Advanced Energy Materials*, 2017, 7, 1602733.

5. S. Srinivasa Rao, I. K. Durga, N. Kundakarla, D. Punnoose, C. V. V. M. Gopi, A. E. Reddy, M. Jagadeesh, and H.-J. Kim, *New J. Chem.*, 2017, 41, 10037—10047.

6. Z.-S. Wu, Y.-Z. Tan, S. Zheng, S. Wang, K. Parvez, J. Qin, X. Shi, C. Sun, X. Bao, X. Feng, and K. Mullen, *J. Am. Chem. Soc.*, 2017, 139, 4506−4512.

7. H. Chen, S. Chen, M. Fan, C. Li, D. Chen, G. Tian, and K. Shu, *J. Mater. Chem. A*, 2015, 3, 23653–23659.

8. P. Simon and Y. Gogotsi, *Nat. Mater.*, 2008, 7, 845.

9. Q. Q. Xiong, J. P. Tu, X. H. Xia, X. Y. Zhao, C. D. Gu, and X. L. Wang, *Nanoscale*, 2013, 5, 7906–7912.

10. M. Zhi, C. Xiang, J. Li, M. Li, and N. Wu, *Nanoscale*, 2013, 5, 72.

11. Y. Li, L. Xu, M. Jia, L. L. Cui, J. Gao, and X.-J. Jin, *Journal of The Electrochemical Society*, 2018, 165, 303-310.

12. H. Yan, T. Li, K. Qiu, Y. Lu, J. Cheng, Y. Liu, J. Xu, Y. Luo, *J Solid State Electrochem*, 2015, 19, 3169–3175.

13. Y. Tian, Y. Ruan, J. Zhang, Z. Yang, J. Jiang, C. Wang, *Electrochimica Acta*, 2017, 250, 327–334.

14. A. Pendashteh, S. E. Moosavifard, M. S. Rahmanifar, Y. Wang, M. F. El-Kady, R. B. Kaner, and M. F. Mousavi, *Chem. Mater.*, 2015, 27, 3919−3926.

15. S. K. Kim, T. Ha, C. Lee, H. Chang, H. D. Jang, *Macromol. Rapid Commun.*, 2019, 1800832.

16. M. Chen, D. Yu, X. Zheng, X. Dong, *J. Energy Storage*, 2019, 21, 105-112.

17. J. Huang, B.G. Sumpter, V. Meunier, *Angew. Chem. Int. Ed.*, 2008, 47, 520-524.

18. S. Sahoo, S. Zhang, J.-J. Shim, *Electrochimica Acta*, 2016, 216, 386-396.

19. Y. Zhang, M. Park, H. Y. Kim, S.-J. Park, *Journal of Colloid and Interface Science*, 2017, 500, 155-163.

20. M. Sethi, D. K. Bhat, *Journal of Alloys and Compounds*, 2019, 781, 1013-1020.

21. Y.-R. Zhu, P.-P. Peng, J.-Z. Wu, T.-F. Yi, Y. Xie, S. Luo, *Solid State Ionics*, 2019, 336, 110-119.

22. S. Wen, K. Qin, P. Liu, N. Zhaoa, C. Shi, L. Ma, E. Liu, *Journal of Alloys and Compounds*, 2019, 783, 625-632.

23. W. Ge, W. Peng, A. Encinas, M. F. Ruiz, S. Song, *Chem. Phys.*, 2019, 521, 55-60.

24. M. Xie, Z. Xu, S. Duan, Z. Tian, Y. Zhang, K. Xiang, M. Lin, X. Guo, W. Ding, *Nano Res.*, 2018, 11, 216-224.

25. N. S. Arul, J. I. Han, *Materials Letters*, 2016, 181, 345-349.

26. Q. Bao, J. Wu, L. Fan, J. Ge, J. Dong, J. Jia, J. Zeng, *J. Lin, Journal of Energy Chemistry*, 2017, 26, 1252-1259.

27. Y. Zhang, A. Pan, Y. Wang, X. Cao, Z. Zhou, T. Zhu, S. Liang, G. Cao, *Energy Storage Materials*, 2017, 8, 28-34.

28. X. Wang, B. Liu, Q. Wang, W. Song, X. Hou, D. Chen, Y.B. Cheng, G. Shen, *Adv. Mater.*, 2013, 25, 1479–1486.

29. D. Jiang, H. Liang, W. Yang, Y. Liu, X. Cao, J. Zhang, C. Li, J. Liu, J. J. Gooding, *Carbon*, 2019, 146, 557-567.

30. V. Ojha, K. Kato, M. A. Kabbani, G. Babu, P. M. Ajayan, *ChemistrySelect*, 2019, 4, 1098–1102.

31. R. Wang, X. Yan, J. Lang, Z. Zheng, P. Zhang, *J. Mater. Chem. A*, 2014, 2, 12724-12732.

32. X. Zhao, C. Johnston, P. S. Grant, *J. Mater. Chem.*, 2009, 19, 8755-8760.

33. V. H. R. Souza, M. M. Oliveira, A. J. G. Zarbin, *Journal of Power Sources*, 2017, 348, 87-93.

34. Y. Zhu, S. Murali, W. Cai, X. Li, J.W. Suk, J.R. Potts, R.S. Ruoff, *Adv. Mater.*, 2010, 22, 3906-3924.

35. R. Chen, L. Liu, L. Hou, J. Zhou, F. Gao, *Chem. Electro. Chem.*, 2017,4, 2250–2259.

36. N.-L. Wu, *Mater. Chem. Phys.*, 2002, 75, 6-11.

37. V.H. Nguyen, J.-J. Shim, *Electrochim. Acta*, 2015, 166, 302-309.

38. M. A. Garakani, S. Abouali, Z.-L. Xu, J. Huang, J.-Q. Huanga, J.-K. Kim, *J. Mater. Chem. A*, 2017,5, 3547-3557.

39. V.H. Nguyen, J.-J. Shim, *Synth. Met.*, 2015, 207, 110-115.

40. H.-W. Wang, Z.-Ai Hu, Y.-Q. Chang, Y.-L. Chen, H.-Y. Wu, Z.-Y. Zhang, Y.-Y. Yang, *J. Mater. Chem.*, 2011, 21, 10504-10511.

41. Q. Li, C. Lu, C. Chen, L. Xie, Y. Liu, Y. Li, Q. Kong, H. Wang, *Energy Storage Materials*, 2017, 8, 59-67.

42. B. G. Amin, A. T. Swesi, J. Masud, M. Nath, *Chem. Commun.*, 2017, 53, 5412-5415.

43. J. Masud, M. Nath, *ACS Energy Lett.*, 2016, 1, 27–31.

44. U. D. Silva, J. Masud, N. Zhang, Y. Hong, W. P. R. Liyanage, M. A. Zaeem, M. Nath, *J. Mater. Chem. A*, 2018, 6, 7608-7622.

45. J. Masud, A. T. Swesi, W. P. R. Liyanage, M. Nath, *ACS Appl. Mater. Interfaces*, 2016, 8, 17292–17302.

46. B. G. Amin, J. Masud, M. Nath, *J. Mater. Chem. B*, 2019,7, 2338-2348.

47. B. G. Amin, U. D. Silva, J. Masud, M. Nath, *ACS Omega*, 2019.

48. Y. Gu, L.-Q. Fan, J.-L. Huang, C.-L. Geng, J.-M. Lin, M.-L. Huang, Y.-F. Huang, J.-H. Wu, *Journal of Power Sources*, 2019, 425, 60-68.

49. J. Yang, Z. Sun, J. Wang, J. Zhang, Y. Qin, J. You, L. Xu, *Cryst. Eng. Comm.*, 2019, 21, 994-1000.

50. A. M. Zardkhoshoui, S. S. H. Davarani, A. A. Asgharinezhad, *Dalton Trans.*, 2019, 48, 4274-4282.

51. A. T. Swesi, J. Masud, W. P. R. Liyanage, S. Umapathi, E. Bohannan, J. Medvedeva and M. Nath, *Sci. Rep.*, 2017, 7, 2401.

52. P. K. Kannan, B. Dinesh, C. Y. An and C.-H. Chung, *ChemistrySelect*, 2017, 2, 1967–1973.

53. X. Chen, D. Chen, X. Guo, R. Wang, H. Zhang, *ACS Appl. Mater. Interfaces*, 2017, 9, 18774−18781.

54. L. Ma, Y. Hu, R. Chen, G. Zhu, T. Chen, H. Lv, Y. Wang, J. Liang, H. Liu, C. Yan, H. Zhu, Z. Tie, Z. Jin, J. Liu, *Nano Energy*, 2016, 24, 139-147.

55. T. Zhu, G. Zhang, T. Hu, Z. He, Y. Lu, G. Wang, H. Guo, J. Luo, C. Lin, Y. Chen, *J. Mater. Sci.*, 2016, 51, 1903−1913.

56. Y.-Z. Su, K. Xiao, N. Li, Z.-Q. Liu, S.-Z. Qiao, *J. Mater. Chem. A*, 2014,2, 13845-13853.

57. L. Mei, T. Yang, C. Xu, M. Zhang, L. Chen, Q. Li and T. Wang, *Nano Energy*, 2014, 3, 36–45.

58. Q. Wang, Y. Ma, Y. Wu, D. Zhang, M. Miao, *Chem. Sus. Chem.*, 2017, 10, 1-10.

59. Z. Chen, D.-B. Xiong, X. Zhang, H. Ma, M. Xia, Y. Zhao, *Nanoscale*, 2016, 8, 6636-6645.

60. M. H. Naveen, K. Shim, Md. S. A. Hossain, J. H. Kim, Y. B. Shim, *Adv. Energy Mater.*, 2016, 1602002, 1–9.

61. M. D. Stoller and R. S. Ruoff, *Energy Environ. Sci.*, 2010, 3, 1294–1301.

SUPPORTING INFORMATION

FACILE ONE-POT SYNTHESIS OF $NiCo_2Se_4$/RGO ON Ni FOAM FOR HIGH PERFORMANCE HYBRID SUPERCAPACITOR

Bahareh Golrokh Amin, Jahangir Masud, Manashi Nath

Department of Chemistry, Missouri University of Science and Technology, Rolla, MO 65409

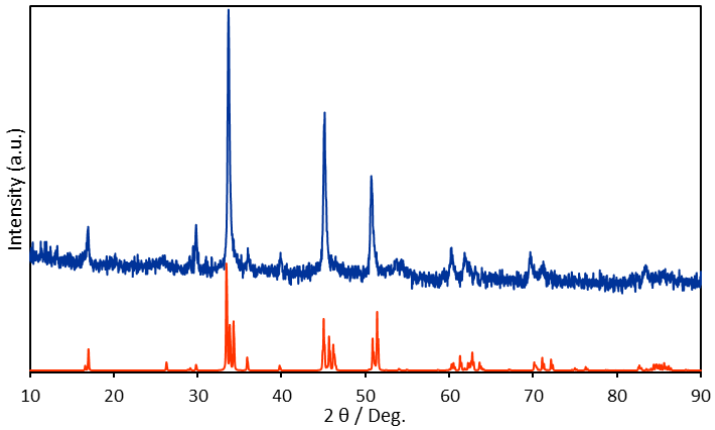

Figure S1. XRD patterns of $NiCo_2Se_4$ along with the reference spectra (PDF No. 04-006-5241).

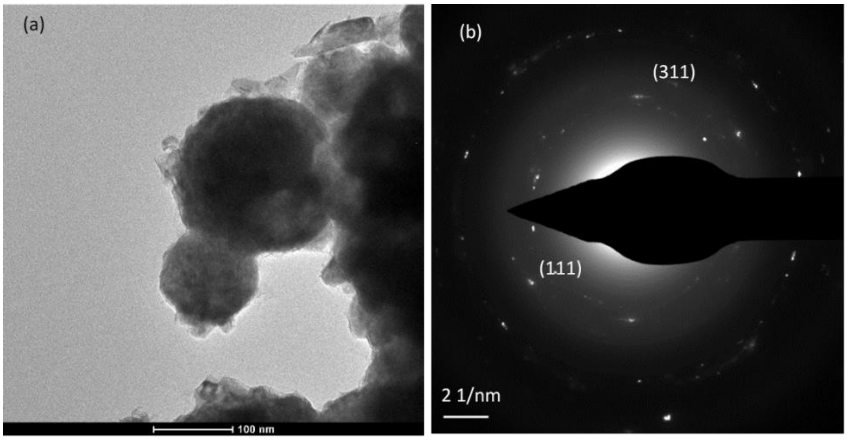

Figure S2. TEM (a) and SAED (b) of $NiCo_2Se_4$.

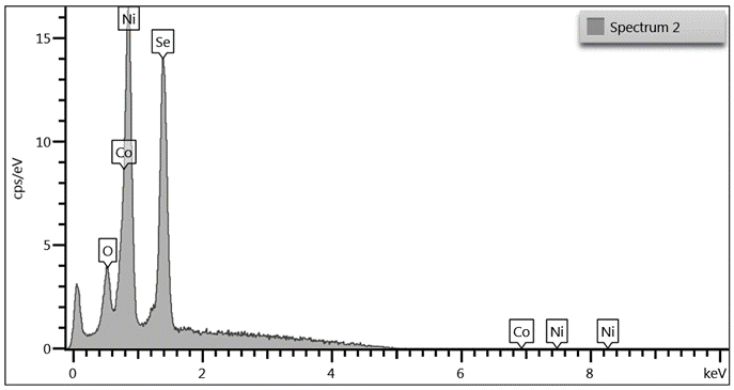

Figure S3. EDS analysis of $NiCo_2Se_4$.

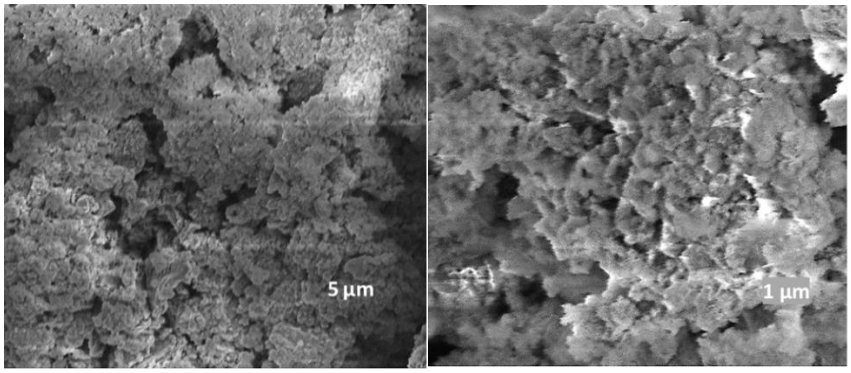

Figure S4. SEM images of $NiCo_2Se_4$ with different magnification.

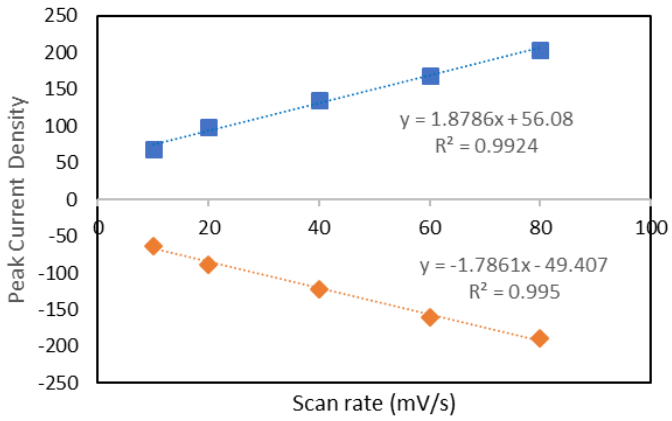

Figure S5. Relationship between the oxidation and reduction peak currents as a function of the scan rate.

Table S1. Comparison of previously reported catalysts in energy storage applications.

Electrode	Specific Capacitance	Energy Density ($Wh\ kg^{-1}$)	Power Density ($W\ kg^{-1}$)	Ref.
$NiCo_2S_4$	1440 @ 3 A g^{-1}	28.3	245	1
$Ni_{0.85}Se$ on Ni foam	1115 @ 1 A g^{-1}	32.2	789.6	2
$Ni_{1.5}Co_{1.5}S_4$	1093 @ 1 A g^{-1}	37.6	775	3
$Co_{0.85}Se$	1378 @ 1 A g^{-1}	39.7	789.6	4
$NiSe_2$	1044 @ 3 A g^{-1}	44.8	969.7	5
Mo_9Se_{11}	601 @ 1 A g^{-1}	42	960	6
$MoSe_2$ on Ni foam	2020 @ 1 A g^{-1}	-	-	7
$NiCo_2S_4$	1612.95 @ 5 A g^{-1}	56	-	8
$NiCo_2Se_4$@carbon microsphere	1394 @ 0.5 A g^{-1}	101	749	9
$NiCo_2Se_4$/rGO@NF	2038.55 @ 1 A g^{-1}	67.01	903.61	This work

REFERENCES

1. Y. Zhu, Z. Wu, M. Jing, X. Yang, W. Song, X. Ji, *Journal of Power Sources*, 2015, 273, 584-590.

2. C. Gong, M. Huang, J. Zhang, M. Lai, L. Fan, J. Lina, J. Wu, *RSC Adv.*, 2015, 5, 81474-81481.

3. H. Chen, J. Jiang, Y. Zhao, L. Zhang, D. Guoa, D. Xia, *J. Mater. Chem. A*, 2015,3, 428-437.

4. C. Gong, M. Huang, P. Zhou, Z. Sun, L. Fan, J. Lin, J. Wu, *Applied Surface Science*, 2016, 362, 30, 469-476.

5. S. Wang, W. Li, L. Xin, M. Wu, Y. Long, H. Huang, X. Lou, *Chem. Eng. J.*, 2017, 330, 1334 – 1341.

6. R.A. Aziz, S.K. Muzakir, I.I. Misnon, J. Ismail, R. Jose, *J. Alloys Compd.*, 2016, 673, 390-398.

7. X. Liu, J.-Z. Zhang, K.-J. Huang, P. Hao, *Chem. Eng. J.*, 2016, 302, 437–445.

8. S. Srinivasa Rao, I. K. Durga, N. Kundakarla, D. Punnoose, C. V. V. M. Gopi, A. E. Reddy, M. Jagadeesh, and H.-J. Kim, *New J. Chem.*, 2017, 41, 10037—10047.

9. 11. Y. Li, L. Xu, M. Jia, L. L. Cui, J. Gao, and X.-J. Jin, *Journal of The Electrochemical Society*, 2018, 165, 303-310.

SECTION

2. CONCLUSIONS

Limitations in large-scale production of previously reported electrode materials and their non-optimal performances in variety of application including full water splitting, non-enzymatic glucose sensing, and supercapacitors motivated us to search for an earth abundant and economical electrode material with superior electrocatalytic activity.

Transition metal chalcogenides are able to meet the requirements for mass production. Since transition metals are the active sites of the electrocatalytic processes, modifying the local coordination environment around the metal center can enhance the performance of the electrode. Therefore, these group of compounds were selected to be evaluated for their application in energy storage, energy conversion, and biosensing.

Experimental analysis on $CoNi_2Se_4$ revealed its higher performance as an efficient electrocatalyst in water splitting compared to the previously reported $NiCo_2O_4$, were oxygen is substituted with selenide. $CoNi_2Se_4$ produces 10 mA cm^{-2} at a cell voltage of 1.61 V. For OER, an overpotential of 160 mV is needed to achieve 10 mA cm^{-2}, which is one of the lowest overpotentials reported to date (Figure 2.1).

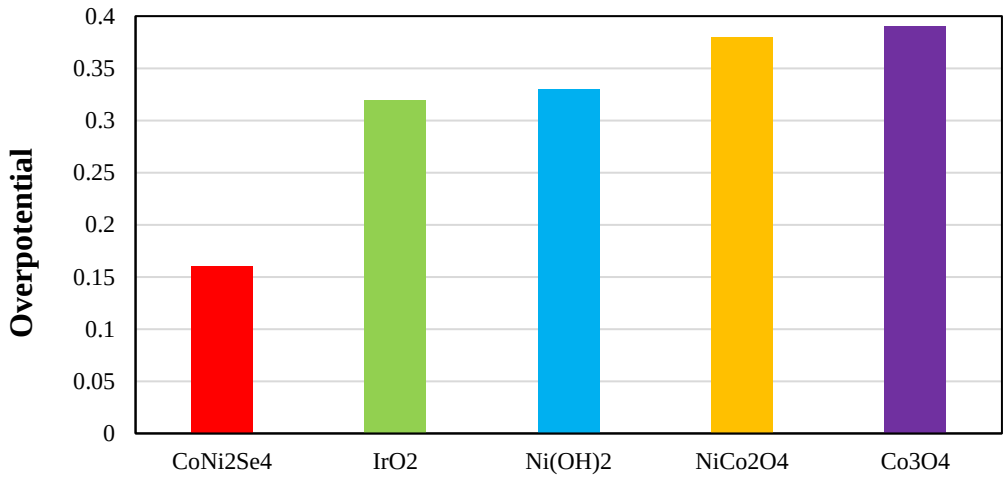

Figure 2.1. $CoNi_2Se_4$ compared to other materials as an OER electrocatalyst.

Investigation on $CoNi_2Se_4$- reduced graphene oxide declares its high performance towards non-enzymatic glucose sensing by achieving a superior sensitivity of 18.89 mA mM^{-1} cm^{-2} in a wide linear response from 1 µM to 4.0 mM at a very low applied potential of +0.35 V vs. Ag|AgCl, which results in higher selectivity of the electrode.

To further verify applicability and correctness of our hypotheses, selenide is replaced by telluride to examine the performance of resulting electrode in non-enzymatic glucose sensing. To verify our method of changing anion coordination, we performed experiments on Ni_3Te_2, fabricated with electrodeposition technique, which resulted in an excellent sensitivity of 41.615 mA cm^{-2} mM^{-1} and a low LOD value of 0.43 µM. To further verify that the performance of this electrode is not solely related to its fabrication method, we repeated the same experiments on a hydrothermally synthesized Ni_3Te_2 and achieved a sensitivity of 35.213 mA cm^{-2} mM^{-1} and an LOD of 0.38 µM (Figure 2.2 and Figure 2.3).

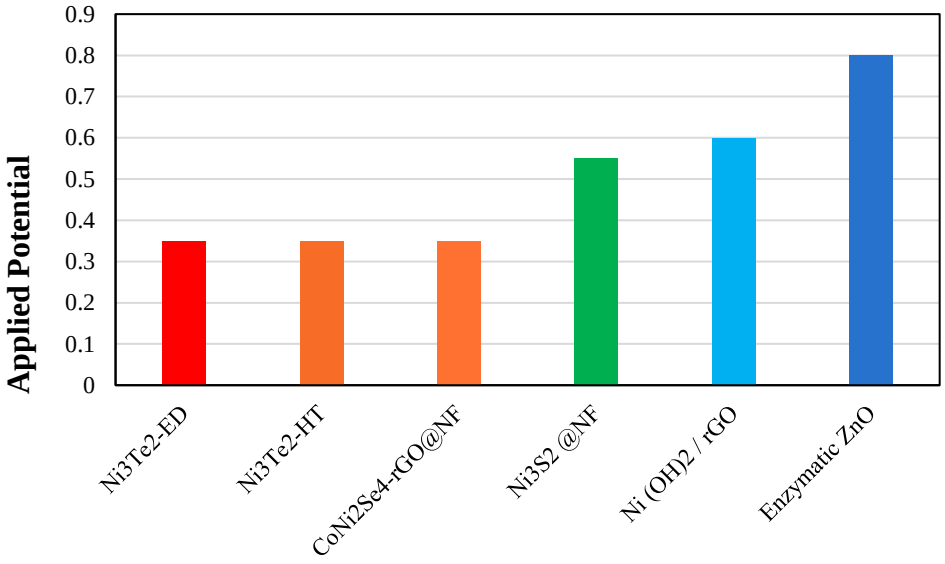

Figure 2.2. Improvements of applied potential in chalcogenide-based electrode compared to others.

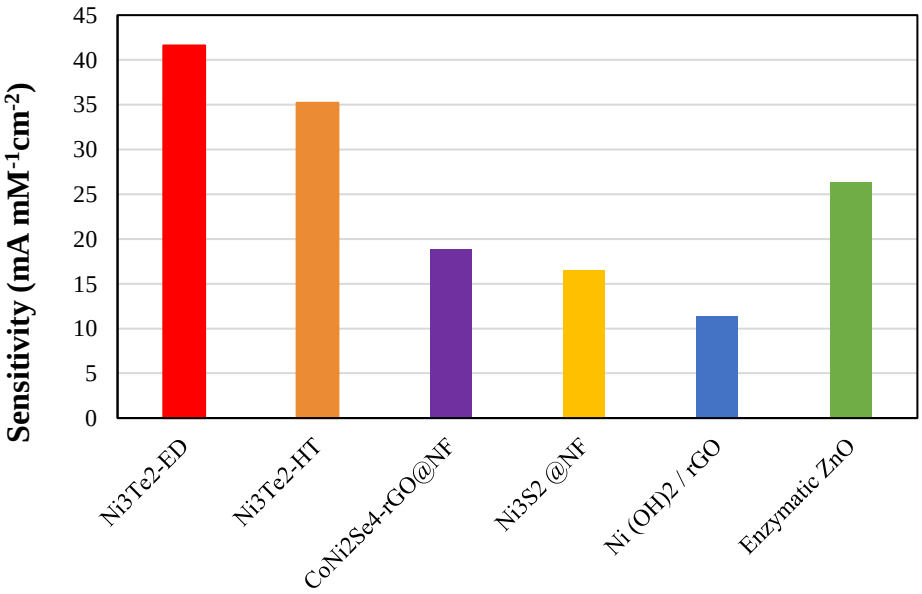

Figure 2.3. Improvements in sensitivity of chalcogenide-based electrode compared to others.

As an energy storage material, $NiCo_2Se_4$- reduced graphene oxide was studied and revealed a high specific capacity of 2038.55 F g^{-1}, energy density of 67.01 W h kg^{-1}, a good cycling stability, and a power density of 903.61 W kg^{-1}. This again exhibits an increase in the catalytic performance of selenide-based electrodes in comparison with previously reported oxide-based electrodes for their application in supercapacitor (Figure 2.4).

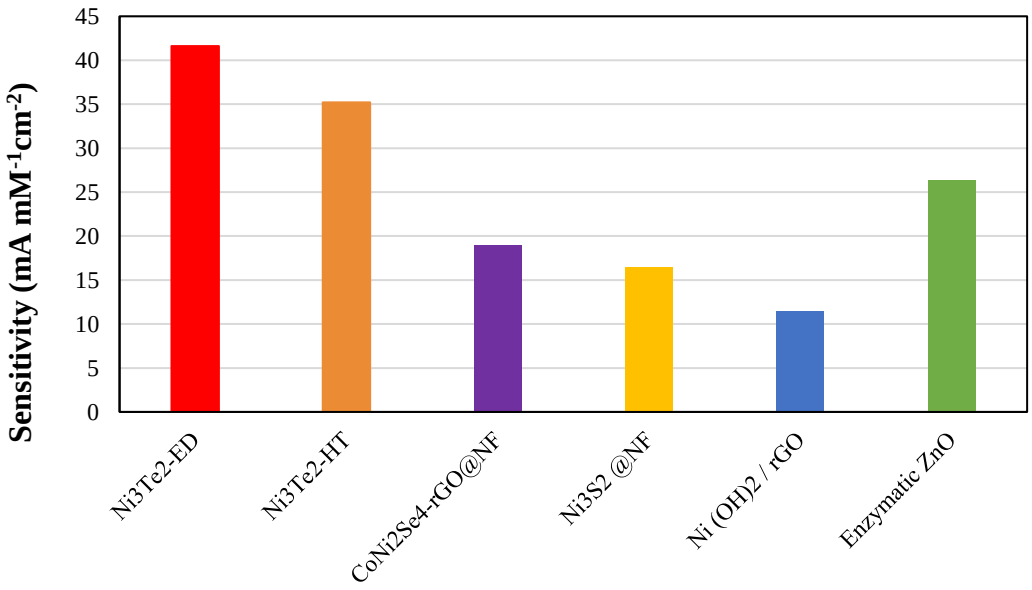

Figure 2.4. Improvements in specific capacitance of chalcogenide-based electrodes compared to others for energy storage.

BIBLIOGRAPHY

1. B.G. Amin, A.T. Swesi, J. Masud, M. Nath, *Chemical Communications*, 2017, 53, 5412-5415.

2. A. T. Swesi, J. Masud, W. P. R. Liyanage, S. Umapathi, E. Bohannan, J. Medvedeva & M. Nath, *Scientific Reports*, 2017, 7, 2401.

3. U. D. Silva, J. Masud, N. Zhang, Y. Hong, W. P. R. Liyanage, M. A. Zaeem, M. Nath, *Journal of Materials Chemistry A*, 2018, 6, 7608-7622.

4. M. Tahir, L. Pan, F. Idrees, X. Zhang, L. Wang, J.-J. Zou, Z. L. Wang, *Nano Energy*, 2017, 37, 136–157.

5. Y. Dou, T. Liao, Z. Ma, D. Tian, Q. Liu, F. Xiao, Z. Sun, J. Ho Kim, S. Xue Dou, *Nano Energy*, 2016, 30, 267–275.

6. G. Wu, A. Santandreu, W. Kellogg, S. Gupta, O. Ogoke, H. Zhang, H.-L. Wang, L. Dai, *Nano Energy*, 2016, 29, 83–110.

7. S. Chen, S. S. Thind, A. Chen, *Electrochemistry Communications*, 2016, 63, 10–17.

8. M.G. Walter, E.L. Warren, J.R. McKone, S.W. Boettcher, Q.X. Mi, E.A. Santori, N.S. Lewis, *Chemical Reviews*, 2010, 110, 6446–6473.

9. G. W. Crabtree, M. S. Dresselhaus, M. V. Buchanan, *Physics Today*, 2004, 57, 39–44.

10. M. Gong, D.-Y. Wang, C.-C. Chen, B.-J. Hwang, H. Dai, *Nano Research*, 2016, 9(1), 28–46.

11. M. S. Dresselhaus, I. L. Thomas, *Nature*, 2001, 414, 332–337.

12. C. Meng, T. Ling, T.-Y. Ma, H. Wang, Z. Hu, Y. Zhou, J. Mao, X.-W. Du, M. Jaroniec, S.-Z. Qiao, *Advanced Materials*, 2017, 29 (9), 1604607.

13. S. Anantharaj, S. R. Ede, K. Sakthikumar, K. Karthick, S. Mishra, S. Kundu, *ACS Catalysis*, 2016, 6, 8069−8097.

14. J. Yu, L. Qi, M. Jaroniec, *Journal of Physical Chemistry C*, 2010, 114 (30), 13118-13125.

15. R. Subbaraman, D. Tripkovic, D. Strmcnik, K.-C. Chang, M. Uchimura, A.P. Paulikas, V. Stamenkovic, N. M. Markovic, *Science*, 2011, 334, 1256-1260.

16. Y. Yan, B. Y. Xia, B. Zhao, X. Wang, *Journal of Materials Chemistry A*, 2016, 4, 17587.

17. T. Audichon, T. W. Napporn, C. Canaff, C. Morais, C. Comminges, K. B. Kokoh, *Journal of Physical Chemistry C*, 2016, 120, 5, 2562-2573.

18. J. Sato, H. Kobayashi, K. Ikarashi, N. Saito, H. Nishiyama, Y. Inoue, *Journal of Physical Chemistry B*, 2004, 108, 14, 4369-4375.

19. S. E. Habas, H. A. S. Platt, M. F. A. M. van Hest, D.S. Ginley, *Chemical Reviews*, 2010, 110, 6571–6594.

20. Z.-F. Huang, J. Song, K. Li, M. Tahir, Y.-T. Wang, L. Pan, L. Wang, X. Zhang, J.-J. Zou, *Journal of the American Chemical Society*, 2016, 138, 1359–1365.

21. H. Wang, H. W. Lee, Y. Deng, Z. Lu, P. C. Hsu, Y. Liu, D. Lin and Y. Cui, *Nature Communications*, 2015, 6, 7261.

22. J. Luo, J.-H. Im, M. T. Mayer, M. Schreier, M. K. Nazeeruddin, N.-G. Park, S. D. Tilley, H. J. Fan and M. Gratzel, *Science*, 2014, 345, 1593–1596.

23. C. Zhang, B. Wang, X. Shen, J. Liu, X. Kong, S.S.C. Chuang, D. Yang, A. Dong, Z. Peng, *Nano Energy*, 2016, 30, 503–510.

24. Q. Li, G. S. Hutchings, W. Yu, Y. Zhou, R. V. Forest, R. Tao, J. Rosen, B. T. Yonemoto, Z. Cao, H. Zheng, J. Q. Xiao, F. Jiao, J. G. Chen, *Nature Communications*, 2015, 6, 6567

25. X. Wang, R. Su, H. Aslan, J. Kibsgaard, S. Wendt, L. Meng, M. Dong, Y. Huang, F. Besenbacher, *Nano Energy*, 2015, 12, 9-18.

26. J. Luo, J. H. Im, M. T. Mayer, M. Schreier, M. K. Nazeeruddin, N. G. Park, S. D. Tilley, H. J. Fan, M. Gratzel, *Science*, 2014, 345, 1593-1596.

27. M. Gong, W. Zhou, M. C. Tsai, J. Zhou, M. Guan, M. C. Lin, B. Zhang, Y. Hu, D. Y. Wang, J. Yang, S. J. Pennycook, B. J. Hwang, H. Dai, *Nature Communications*, 2014, 5, 4695.

28. Y. Shi, H. Li, L. J. Li, *Chemical Society Reviews*, 2015, 44, 2744-2756.

29. Z. Lv, N. Mahmood, M. Tahir, L. Pan, X. Zhang, J.-J. Zou, *Nanoscale*, 2016, 8, 18250–18269.

30. A. T. Swesi, J. Masud, M. Nath, *Energy & Environmental Science*, 2016,9, 1771-1782.

31. H. B. Wu, B. Y. Xia, L. Yu, X. Y. Yu, X. W. Lou, *Nature Communications*, 2015, 6, 6512.

32. X. Fan, H. Zhou, X. Guo, *ACS Nano*, 2015, 9, 5125-5134.

33. C. G. Morales-Guio, L. A. Stern, X. Hu, *Chemical Society Reviews*, 2014, 43, 6555-6569.

34. Y. Jiao, Y. Zheng, M. Jaroniec, S. Z. Qiao, *Chemical Society Reviews*, 2015, 44, 2060-2086.

35. Y. Zheng, Y. Jiao, Y. Zhu, L. H. Li, Y. Han, Y. Chen, A. Du, M. Jaroniec, S. Z. Qiao, *Nature Communications*, 2014, 5, 3783.

36. X. Zou and Y. Zhang, *Chemical Society Reviews*, 2015, 44, 5148–5180.

37. Z. Xia, *Nature Energy*, 2016, 1, 16155.

38. Y. Gorlin, T.F. Jaramillo, *Journal of the American Chemical Society*, 2010, 132, 13612–13614.

39. M. Gong, Y. Li, H. Wang, Y. Liang, J.Z. Wu, J. Zhou, J. Wang, T. Regier, F. Wei, H. Dai, *Journal of the American Chemical Society*, 2013, 135, 8452–8455.

40. T. R. Cook, D. K. Dogutan, S. Y. Reece, Y. Surendranath, T. S. Teets and D. G. Nocera, *Chemical Reviews*, 2010, 110, 6474– 6502.

41. B. E. Conway, L. Bai, M. A. Sattar, *International Journal of Hydrogen Energy*, 1987, 9, 607.

42. M. Busch, N.B. Halck, U.I. Kramm, S. Siahrostami, P. Krtil, J. Rossmeisl, *Nano Energy*, 2016, 29, 126–135.

43. M. Gong, H. Dai, *Nano Research*, 2015, 8, 23–39.

44. A. Lasia, Hydrogen Evolution Reaction, Handbook of Fuel Cells, *John Wiley & Sons*, 2010.

45. N. Danilovic, R. Subbaraman, D. Strmcnik, V. R. Stamenkovic, N. M Markovic, *Journal of the Serbian Chemical Society*, 2013, 78, 2007–2015.

46. M. Gong, H. Dai, *Nano Research*, 2015, 8, 23–39.

47. J. Masud, S. Umapathi, N. Ashokan, M. Nath, *Journal of Materials Chemistry A*, 2016, 4, 9750–9754.

48. N. S. Lewis, D. G. Nocera, *Proceedings of the National Academy of Sciences*, 2006, 103, 15729–15735.

49. E. Fabbri, A. Habereder, K. Waltar, R. Kotz, T. J. Schmidt, *Catalysis Science & Technology*, 2014, 4, 3800–3821.

50. Y. Lee, J. Suntivich, K. J. May, E. E. Perry, Y.S. Horn, *Journal of Physical Chemistry Letters*, 2012, 3, 399–404.

51. J. Masud, A. T. Swesi, W. P. R. Liyanage and M. Nath, *ACS Applied Materials & Interfaces*, 2016, 8, 17292.

52. J. Masud, P. Ioannou, N. Levesanos, P. Kyritsis, M. Nath, *Chem.Sus.Chem.*, 2016, 9, 3123.

53. D. Kong, H. Wang, Z. Lu and Y. Cui, *Journal of the American Chemical Society*, 2014, 136, 4897.

54. X. Xu, P. Du, Z. Chen and M. Huang, *Journal of Materials Chemistry A*, 2016, 4, 10933.

55. Z. Wang, J. Li, X. Tian, X. Wang, Y. Yu, K. A. Owusu, L. He and L. Mai, *ACS Applied Materials & Interfaces*, 2016, 8, 19386.

56. M. Hamdani, R. Singh and P. Chartier, *International Journal of Electrochemical Science*, 2010, 5, 556.

57. F. Basharat, U. A. Rana, M. Shahida and M. Serwara, *RSC Advances*, 2015, 5, 86713.

58. Q. Dong, C. Sun, Z. Dai, X. Zang and X. Dong, *Chem.Cat.Chem.*, 2016, 8, 3484.

59. Z. Zhang, S. Liu, F. Xiao and S. Wang, *ACS Sustainable Chemistry & Engineering*, 2017, 5, 529.

60. J. Liang, Y.Z. Wang, C.C. Wang, S.Y. Lu, *Journal of Materials Chemistry A*, 2016, 4, 9797-9806.

61. X. Chen, D. Chen, X. Guo, R. Wang, H. Zhang, *ACS Applied Materials & Interfaces*, 2017, 9, 18774−18781.

62. L. Ma, Y. Hu, R. Chen, G. Zhu, T. Chen, H. Lv, Y. Wang, J. Liang, H. Liu, C. Yan, H. Zhu, Z. Tie, Z. Jin, J. Liu, *Nano Energy*, 2016, 24, 139-147.

63. S. Y. Tee, C. P. Teng, E. Ye, *Materials Science and Engineering C*, 2017, 70, 1018–1030.

64. S. Coster, M.C. Gulliford, P.T. Seed, J.K. Powrie, R. Swaminathan, *Health Technology Assessment*, 2000, 4, 1–93.

65. J. Wang, D.F. Thomas, A. Chen, *Analytical Chemistry*, 2008, 80, 997–1004.

66. H. King, R.E. Aubert, W.H. Herman, *Diabetes Care*, 1998, 21, 1414–1431.

67. S.H. Wild, G. Roglic, A. Green, R. Sicree, H. King, *Diabetes Care*, 2004, 27, 1047–1053.

68. J. Wang, *Chemical Reviews*, 2008, 108, 814–825.

69. K. M. Shaw, M. H. Cummings, Diabetes: Chronic Complications, John Wiley & Sons, 2005.

70. Q. Qian, Q. Hu, L. Li, P. Shi, J. Zhou, J. Kong, X. Zhang, G. Sun, W. Huang, *Sensors and Actuators B*, 2018, 257, 23–28.

71. Kim, S.; Lee, S.H.; Cho, M.; Lee, Y., *Biosensors and Bioelectronics*, 2016, 85, 587–595.

72. S.P. Nichols, A. Koh, W.L. Storm, J.H. Shin, M.H. Schoenfisch, *Chemical Reviews*, 2013, 113, 2528.

73. A.P.F. Turner, *Chemical Society Reviews*,2013, 42, 3184–3196.

74. K. Tian, M. Prestgard, A. Tiwari, *Materials Science and Engineering C*, 2014, 41, 100–118.

75. A. J. Bandodkar, J. Wang, *Trends in Biotechnology*, 2014, 32, 7.

76. K.L. Wu, Y.M. Cai, B.B. Jiang, W.C. Cheong, X.W. Wei, W. Wang, and N. Yu, *RSC Advances*, 2017, 7, 21128-21135.

77. N. Hui, J. Wang, *Journal of Electroanalytical Chemistry*, 2017, 798, 9–16.

78. L. C. Clark, C. Lyons, Ann. N. Y. Proceedings of the National Academy of Sciences, 1962, 102, 29– 45.

79. J. Wang, F. Lu, *Journal of the American Chemical Society*, 1998, 120, 1048.

80. J. Wang, J.W. Mo, S. Li, J. Porter, *Analytica Chimica Acta*, 2001, 441, 183.

81. D. A. Gough, J. Y. Lucisano, P. H. S. Tse, *Analytical Chemistry*, 1985, 57, 2351.

82. J. C. Armour, J. Y. Lucisano, B. D. McKean, D. A. Gough, *Diabetes*, 1990, 39, 1519.

83. A. E. G. Cass, G. Davis, G. D. Francis, H. A. O. Hill, W. J. Aston, I. J. Higgins, E. V. Plotkin, L. D. L. Scott, A. P. F. Turner, *Analytical Chemistry*, 1984, 56, 667.

84. A. Mulchandani, S. Pan, *Analytical Biochemistry*, 1999, 267, 141.

85. S. Tsujimura, S. Kojima, K. Kano, T. Ikeda, M. Sato, H. Sanada, H. Omura, *Bioscience, Biotechnology, and Biochemistry*, 2006, 70, 654.

86. M. G. Loughran, J. M. Hall, and A. P. F. Turner, *Electroanalysis*, 1996, 8, 870.

87. K. Lau, S. A. L. de Fortescu, L. J. Murphy, J. M. Slater, *Electroanalysis*, 2003, 15, 975.

88. C. Taylor, G. Kenausis, I. Katakis, A. Heller, *Journal of Electroanalytical Chemistry*, 1995, 396, 511.

89. A. Heller, B. Feldman, *Accounts of Chemical Research*, 2010.

90. Y. Wang, F. Caruso, *ChemComm*, 2004, 1528-1529.

91. S. Wu, H. Ju, Y. Liu, *Advanced Functional Materials*, 2007, 17, 585.

92. S. Bao, C. M. Li, J. Zang, X. Cui, Y. Qiao, J. Guo, *Advanced Functional Materials*, 2008, 18, 591.

93. J. Wu and Y. Qu, *Analytical and Bioanalytical Chemistry*, 385, 2006, 1330.

94. F. Palmisano, P. G. Zambonin, D. Centonze, and M. Quinto, *Analytical Chemistry*, 74, 2002, 5913.

95. G. J. Koopal, A. A. C. M. Bos, and R. J. M. Nolte, *Sensors and Actuators B*, 18, 1994, 166.

96. S. Park, H. Boo, T.D. Chung, *Analytica Chimica Acta*, 556, 2006, 46.

97. M.M. Rahman, A.J.S. Ahammad, J.H. Jin, S.J. Ahn, J.J. Lee, *Sensors*, 10, 2010, 4855.

98. P. Si, Y. Huang, T. Wang, J. Ma, *RSC Advances*, 2013, 3, 3487.

99. W. Loeb, *Biochemische Zeitschrift*, 17, 1909, 132-144.

100. H. Wroblowa, B. J. Piersma, and J. O. Bockris, *Journal of Electroanalytical Chemistry*, 1963, 6, 1959-1966, 401.

101. J. O. Bockris, B. J. Piersma, and E. Gileadi, *Electrochimica Acta*, 1964, 9, 1329.

102. X. Bo, J. C. Ndamanisha, J. Bai, L. Guo, *Talanta*, 2010, 82, 85-91.

103. G. Chang, H. Shu, Q. Huang, M. Oyama, K. Ji, X. Liu, Y. He, *Electrochimica Acta*, 2015, 157, 149–157.

104. Y. Li, X. Niu, J. Tang, M. Lan, H. Zhao, *Electrochimica Acta*, 2014, 130, 1–8.

105. C. Li, H. Wang, Y. Yamauchi, *ChemPubSoc Europe*, 2013, 19, 2242–2246.

106. S. Park, H. Boo, T. D. Chung, *Analytica Chimica Acta*, 2006, 556, 46–57.

107. J. P. Wang, D. F. Thomas and A. C. Chen, *Analytical Chemistry*, 2008, 80, 997–1004.

108. A. Soni, S. K. Jha, *Biosensors and Bioelectronics.*, 2015, 67, 763–768.

109. M. X. Chu, K. Miyajima, D. Takahashi, T. Arakawa, K. Sano, S. Sawada, H. Kudo, Y. Iwasaki, K. Akiyoshi, M. Mochizukiand K. Mitsubayashi, *Talanta*, 2011, 83, 960–965.

110. O. Olarte, J. Chilo, J. Pelegri-Sebastia, K. Barbe, W. V. Moer, *IEEE Engineering in Medicine and Biology Society*, 2012, 1462–1465.

111. X. Niu, X. Li, J. Pan, Y. He, F. Qiu, Y. Yan, *RSC Advances*, 2016, 6, 84893.

112. M. L. Hammock, A. Chortos, B. C.-K. Tee, J. B.-H. Tok, Z. Bao, *Advanced Materials*, 2013, 25, 5997–6038.

113. J. R. Windmiller, J. Wang, *Electroanalysis*, 2013, 25, 29–46.

114. J. Lankelma, Z. Nie, E. Carrilho, G. M. Whitesides, *Analytical Chemistry*, 2012, 84 (9), 4147−4152.

115. D. Ye, G. Liang, H. Li, J. Luo, S. Zhang, H. Chen, J. Kong, *Talanta*, 2013, 116, 223−230.

116. J. Moyer, D. Wilson, I. Finkelshtein, B. Wong, R. Potts, *Diabetes Technology and Therapeutics*, 2012, 14, (5) 398−402.

117. Guilin Li, Huanhuan Huo and Cailing Xu, *Journal of Materials Chemistry A*, 2015, 3, 4922–4930.

118. B. G. Amin, J. Masud, M. Nath, *Journal of Materials Chemistry B*, 2019,7, 2338-2348.

119. K. E. Toghill and R. G. Compton, *International Journal of Electrochemical Science*, 2010, 5, 1246–1301.

120. S. L. Brooks, R. E. Ashby, A. P. F. Turner, M. R. Calder, D. J. Clarke, *Biosensors*, 1987, 3, 45.

121. S. F. White, I. E. Tothill, J. D. Newman, A. P. F. Turner, *Analytica Chimica Acta*, 1996, 321, 165.

122. P. Favier, D. Bicanic, P. Helander, M. van Iersel, *Journal of Biochemical and Biophysical Methods*, 1997, 34, 205.

123. P. Nandakumar, A. Sapre, A. Lali, B. Mattiasson, *Applied Microbiology and Biotechnology*, 1999, 52, 502.

124. Vidotti, C. D. Cerri, R. F. Carvalhal, J. C. Dias, R. K. Mendes, S. I. Cordoba de Torresi, L.T. Kubota, *Journal of Electroanalytical Chemistry*, 2009, 636, 18.

125. T. You, O. Niwa, Z. Chen, K. Hayashi, M. Tomita, S. Hirono, *Analytical Chemistry*, 2003, 75, 5191.

126. S. Dong, S. Zhang, X. Cheng, P. He, Q. Wang, Y. Fang, *Journal of Chromatography A*, 2007, 1161, 327.

127. S. B. Aoun, G. S. Bang, T. Koga, Y. Nonaka, T. Sotomura, I. Taniguchi, *Electrochemistry Communications*, 2003, 5, 317.

128. M. L. B. Rao, R. F. Drake, *Electrochemistry Communications*, 1969, 116, 334.

129. J Giner, G. Holleck, *University of Washington Press, Seattle*, 1972, 283.

130. R. Rao, G. J. Richter, F. Von Sturm, E. Weidlich, *Bioelectrochemistry and Bioenergetics*, 1976, 3, 139.

131. S. Kerzenmacher, J. Ducree, R. Zengerle, F. von Stetten, *Journal of Power Sources*, 2008, 182, 1.

132. H. Chen, S. Chen, M. Fan, C. Li, D. Chen, G. Tian, and K. Shu, *Journal of Materials Chemistry A*, 2015, 3, 23653–23659.

133. S. Srinivasa Rao, I. K. Durga, N. Kundakarla, D. Punnoose, C. V. V. M. Gopi, A. E. Reddy, M. Jagadeesh, H.-J. Kim, *New Journal of Chemistry*, 2017, 41, 10037—10047.

134. C. Largeot, C. Portet, J. Chmiola, P. Taberna, Y. Gogotsi, P. Simon, *Journal of the American Chemical Society*, 2008, 130, 2730.

135. S. Kandalkar, D. Dhawale, C. Kim, C. Lokhande, *Synthetic Metals*, 2010, 160, 1299.

136. R. Kötz, M. Carlen, *Electrochimica Acta*, 2000, 45, 2483.

137. R. Kotz, S. Muller, M. Bartschi, B. Schnyder, P. Dietrich, F. N. Buchi, A. Tsukada, G. G. Scherer, P. Rodatz, O. Garcia, P. Barrade, V. Hermann and R. Gallay, *Electrochemical Society Proceedings*, 2001, 21, 564.

138. M. Jayalakshmi, K. Balasubramanian, *International Journal of Electrochemical Science*, 2008, 3, 1196 – 1217.

139. P. Simon, Y. Gogotsi, *Nature Materials*, 2008, 7, 845.

140. G. Wang, L. Zhang, J. Zhang, *Chemical Society Reviews*, 2012, 41, 797–828.

141. J. P. Zheng, J. Huang, T. R. Jow, *Journal of the Electrochemical Society*, 1997, 144, 2026.

142. Y. M. Volfkovich, T. M. Serdyuk, *Russ. Journal of the Electrochemical Society*, 2002, 38, 935.

143. Y. Zhang, H. Feng, X. Wu, L. Wang, A. Zhang, T. Xia, H. Dong, X. Li, L. Zhang, *International Journal of Hydrogen Energy*, 2009, 34, 4889.

144. C. Ming Chuang, C. W. Huang, H. Teng, J. M. Ting, *Energy and Fuels*, 2010, 24, 6476.

145. B. E. Conway, V. Birss, J. Wojtowicz, *Journal of Power Sources*, 1997, 66, 1.

146. A. Burke, *Journal of Power Sources*, 2000, 91, 37.

147. S. Ma, K. Nam, W. Yoon, X. Yang, K. Ahn, K. Oh, K. Kim, *Electrochemistry Communications*, 2007, 9, 2807.

148. M. Kisacikoglu, M. Uzunoglu, M. Alam, *International Journal of Hydrogen Energy*, 2009, 34, 1497.

149. M. C. Kisacikoglu, M. Uzunoglu, M. S. Alam, *International Journal of Hydrogen Energy*, 2009, 34, 1497–507.

150. T. Aida, K. Yamada, M. Morita, *Electrochemical and Solid State Letters*, 2006, 9, A534–6.

151. E. Frackowiak, *Physical Chemistry Chemical Physics*, 2007, 9, 1774.

152. A. S. Arico, P. Bruce, B. Scrosati, J. Tarascon, W. V. Chalkwijk, *Nature Materials*, 2005, 4, 366.

153. V. Ruiz, C. Blanco, E. R. Pinero, V. Khomenko, F. Beguin, R. Santamaria, *Physical Chemistry Chemical Physics*, 2007, 52, 4969.

154. J. C. Meyer, A. K. Geim, M. I. Katsnelson, K. S. Novoselov, T. J. Booth, S. Roth, *Nature*, 2007, 446, 60.

155. M. J. Allen, V. C. Tung, R. B. Kaner, *Chemical Reviews*, 2010, 110, 132.

156. C. Gomez-Navarro, R. T. Weitz, A. M. Bittner, M. Scolari, A. Mews, M. Burghard, K. Kern, *Nano Letters*, 2007, 7, 3499.

157. Y. Zhu, S. Murali, W. Cai, X. Li, J.W. Suk, J.R. Potts, R.S. Ruoff, *Advanced Materials*, 2010, 22, 3906-3924.

158. Y. Zhang, H. Feng, X. Wu, L. Wang, A. Zhang, T. Xia, H. Dong, X. Li, L. Zhang, *International Journal of Hydrogen Energy*, 2009, 34, 4889.

159. D. Qu, *Journal of Power Sources*, 2002, 109, 403.

160. D. D. Zhao, S. J. Bao, W. J. Zhou, H. L. Li, *Electrochemistry Communications*, 2007, 9, 869.

161. H. Xia, Y. S. Meng, G. Yuana, C. Cuia, L. Lu, *Electrochemical and Solid State Letters*, 2012, 15, 4, 60-63.

162. V. Subramanian, S. C. Hall, P. H. Smith, B. Rambabu, *Solid State Ionics*, 2004, 175, 30, 511-515.

163. P. Zhao, M. Yao, H. Ren, N. Wang, S. Komarneni, *Applied Surface Science*, 2019, 463, 931-938.

164. Y. Xie, C. Yang, P. Chen, D. Yuan, K. Guo, *Journal of Power Sources*, 2019, 425, 1-9.

165. H. Liu, W. Zhu, D. Long, J. Zhu, G. Pezzotti, *Applied Surface Science*, 2019, 478, 383-392.

166. D. Majumdar, M. Mandal, S. K. Bhattacharya, *Chem. Electro. Chem.*, 2019, 6, 1623-1648.

167. S. Trasatti, G. Buzzanca, *Journal of Electroanalytical Chemistry and Interfacial Electrochemistry*, 1971, 29, 1-5.

168. P. Wu, S. Cheng, M. Yao, L. Yang, Y. Zhu, P. Liu, O. Xing, J. Zhou, M. Wang, H. Luo, M. Liu, *Advanced Functional Materials*, 2017, 27, 1702160.

169. M. Xiang, H. Wu, H. Liu, J. Huang, Y. Zheng, L. Yang, P. Jing, Y. Zhang, S. Dou, H. Liu, *Advanced Functional Materials*, 2017, 27, 1702573.

170. H. Ma, D. Kong, Y. Xu, X. Xie, Y. Tao, Z. Xiao, W. Lv, H. D. Jang, J. Huang, Q. H. Yang, *Small*, 2017, 13.

171. C. Xia, Q. Jiang, C. Zhao, P. M. Beaujuge, H. N. Alshareef, *Nano Energy*, 2016, 24, 78-86.

172. H. Yuan, L. Kong, T. Li, Q. Zhang, *Chinese Chemical Letters*, 2017, 28, 2180-2194.

173. Z. Li, Z. Xu, H. Wang, J. Ding, B. Zahiri, C. M. B. Holt, X. Tan, D. Mitlin, *Energy and Environmental Science*, 2014, 7, 1708.

174. Y. Li, L. Xu, M. Jia, L. L. Cui, J. Gao, X.-J. Jin, *Journal of the Electrochemical Society*, 2018, 165, 9, E303-E310.

175. L. Shen, L. Yu, H.B. Wu, X.Y. Yu, X. Zhang, X.W.D. Lou, *Nature Communications*, 2015, 6, 6694.

176. B. You, Y.J. Sun, *Advanced Energy Materials*, 2016, 6, 1502333–1502341.

177. X. Zheng, H. Wang, C. Wang, Z. Deng, L. Chen, Y. Li, T. Hasan, B.L. Su, *Nano Energy*, 2016, 22, 269–277.

178. W. Zeng, G. Zhang, X. Wu, K. Zhang, H. Zhang, S. Hou, C. Li, T. Wang, H. Duan, *Journal of Materials Chemistry A*, 2015, 3, 24033–24040.

179. H. Chen, S. Chen, M. Fan, C. Li, D. Chen, G. Tian, K. Shu, *Journal of Materials Chemistry A*, 2015, 3, 23653.

180. J. Huang, P. Xu, D. Cao, X. Zhou, S. Yang, Y. Li, G. Wang, *Journal of Power Sources*, 2014, 246, 371–376.

181. T. H. Chen, Z. L. Liu, Z. S. Liu, X. Y. Tao, H. L. Fan, L. T. Guo, *Materials Letters*, 2019, 248, 1-4.

182. J. Goua, S. Xie, Z. Yang, Y. Liu, Y. Chen, Y. Liu, C. Liu, *Electrochimica Acta*, 2017, 229, 299-305.

183. H. Wang, M. Liang, D. Duan, W. Shi, Y. Song, Z. Sun, *Chemical Engineering Journal*, 2018, 350, 523-533.

184. Z. Gao, C. Chen, J. Chang, L. Chen, P. Wang, D. Wu, F. Xu, K. Jiang, *Chemical Engineering Journal*, 2018, 343, 572-582.

185. D. Ghosh, C. K. Das, *ACS Applied Materials & Interfaces*, 2015, 7, 2, 1122-1131.

186. Q. Zhang, C, Xu, B. Lu, *Electrochimica Acta*, 2014,132, 180-185.

187. L. Meng, Y. Wu, T. Zhang, H. Tang, Y. Tian, Y. Yuan, Q. Zhang, Y. Zeng, J. Lu, *Journal of Materials Science*, 2019, 54, 571–581.

188. A. Chang, C. Zhang, Y. Yu, Y. Yu, B. Zhang, *ACS Applied Materials & Interfaces*, 2018, 10, 49, 41861-41865.

189. N. S. Arul, J. I. Han, *Materials Letters*, 2019, 234, 87-91.

190. H. Chen, M. Fan, C. Li, G. Tian, C. Lv, D. Chen, K. Shu, J. Jiang, *Journal of Power Sources*, 2016, 329, 314-322.

191. B. Kirubasankar, V. Murugadoss, S. Angaiah, *RSC Advances*, 2017, 7, 5853-5862.

192. J. Lin, H. Wang, Y. Yan, X. Zheng, H. Jia, J. Qi, J. Cao, J. Tu, W. Fei, J. Feng, *Journal of Materials Chemistry A*, 2018, 6, 19151-19158.

193. Y. Zhang, A. Pan, L. Ding, Z. Zhou, Y. Wang, S. Niu, S. Liang, G. Cao, *ACS Applied Materials & Interfaces*, 2017, 9, 4, 3624-3633.

194. S. Wang, W. Li, L. Xin, M. Wu, Y. Long, H. Huang, X. Lou, *Chemical Engineering Journal*, 2017, 330, 1334-1341.

195. G. A. Snook, P. Kao, A. S. Best, *Journal of Power Sources*, 2011, 196, 1.

VITA

Bahareh Golrokh Amin was born in Tehran, Iran. She received her B.Sc. in Chemistry and Information Technology from the Shahid Beheshti University in June 2015. She continued her studies in Chemistry at the Missouri University of Science and Technology in August 2015. During her Ph.D. studies, Bahareh served as instructor for several Chemistry courses and performed research on new materials for energy storage and biosensing. In July 2019, she received her Ph.D. degree in Chemistry from Missouri University of Science and Technology.